Structural and dynamic insights into oxazolidinone binding, selectivity and resistance to the large ribosomal subunit

Inaugural-Dissertation

for the attainment of the title of doctor
in the Faculty of Mathematics and Natural Sciences
at the Heinrich Heine University Düsseldorf

Presented by

Jagmohan S. Saini
from Punjab, India

Düsseldorf, March 2018

from the Institute for Pharmaceutical and Medicinal Chemistry
at the Heinrich Heine University Düsseldorf

Published by permission of the
Faculty of Mathematics and Natural Sciences at
Heinrich Heine University Düsseldorf

Supervisor: Prof. Dr. Holger Gohlke
Co-supervisor: Prof. Dr. Gerhard Steger

Declaration

I declare under oath that I have compiled my dissertation independently and without any undue assistance by third parties under consideration of the 'Principles for the Safeguarding of Good Scientific Practice at Heinrich Heine University Düsseldorf'.

This dissertation has not been submitted in its present or a similar form in any other institution. I have not made any successful or unsuccessful attempt to obtain a doctorate before.

Düsseldorf, March 2018
Jagmohan S. Saini

To my beloved family

Acknowledgements

This work would have not been possible without the financial support from the International NRW Research School BioStruct, granted by the Ministry of Innovation, Science and Research of the State North Rhine-Westphalia, the Heinrich Heine University of Dusseldorf, and the Entrepreneur Foundation at the Heinrich Heine University of Dusseldorf. We are grateful to the Julich Supercomputing Center (NIC project 5921) and to the 'Zentrum fur Informations-und Medientechnologie' (ZIM) at the HHU for providing computational support.

I thank Prof. Dr. Holger Gohlke for his guidance and support throughout this study, all his advice, discussions and suggestions and especially for his confidence in me. In addition, I thank the whole working group for the friendly and inspiring working atmosphere. Especially, I thank Simone Fulle, Nadine Homeyer, Christian Hanke, and Alexander Metz for their support. Many thanks to Prakash Chandra Rathi, Christopher Pfleger, Doris Klein, Dennis Krüger, Daniela Grimme, Emanuele Ciglia, and Ido Ben-Shalom for their valuable suggestions and friendship. Special thanks to Christian and Prakash for carefully proof reading parts of the thesis.

I am very grateful to Prof. Dr. Gerhard Steger for providing valuable inputs.

Finally, I would like to thank my family, especially my wife Palak and son Jashan, for their endless support, care and for being with me in every situation.

Table of contents

List of publications

This thesis is based on the following manuscripts:

1: Jagmohan S. Saini (80%), Nadine Homeyer, Simone Fulle, Holger Gohlke, Determinants of the species-selectivity of oxazolidinone antibiotics targeting the large ribosomal subunit. **Biol. Chem.,** 2013, 1529-41.

Impact factor reported for 2016: **4.573.**

2: Simone Fulle (40%), Jagmohan S. Saini (40%), Nadine Homeyer, Holger Gohlke, *Complex long distance effects of mutations that confer linezolid resistance in the large ribosomal subunit.* **Nucleic Acids Res.,** 2015, 7731–7743.

Impact factor reported for 2016: **10.162**.

Conference contributions and oral presentations arising from this work

- Oral presentation titled "*Molecular insights into binding and selectivity of oxazolidinone antibiotics targeting the large ribosomal subunit*" at the BioStruct Symposium 2013, Düsseldorf, Germany, November 4-6, 2013.
- Oral presentation titled "*What determines oxazolidinone binding to the large ribosomal subunit*" at the 27th Molecular Modeling Workshop 2013, Erlangen, Germany, Feb. 25-27, 2013.
- Presented poster titled "*Structural and energetic determinants of oxazolidinone binding to the large ribosomal subunit*" at the Workshop on Computer Simulation and Theory of Macromolecules, Hünfeld, Germany, April 20-21, 2012.
- Presented poster titled *"Structural insights into the binding and resistance development of oxazolidinone antibiotics"* at the NIC symposium 2012, Jülich, Germany, February 7-8, 2012.
- Presented poster titled "*Molecular recognition of RNA structures: challenges for modeling macromolecular flexibility and plasticity"* at 7th German Conference on Cheminformatics, Goslar, Germany, November 6-8, 2011.
- Presented poster titled "*Molecular dynamics simulations of ribosome-oxazolidinone complexes reveal structural aspects for antibiotic design"*at BioStruct MasterClass 2011, Heinrich Heine University, Düsseldorf, Germany, September 12-15, 2011. [Awarded with 2nd "best poster award"]
- Presented poster titled "*Structural and energetic aspects of oxazolidinone antibiotics binding to the ribosomal structure"* at 'From Computational Biophysics to Systems Biology' 2011, Jülich, Germany, July 20-22, 2011.
- Presented poster titled "*Structural and energetic aspects of oxazolidinone antibiotics binding to the ribosomal structure" at* 9th International Conference on Chemical Structures, Noordwijkerhout, The Netherlands, June 5-9, 2011.
- Presented poster titled "*Structural and energetic aspects of oxazolidinone antibiotics binding to the ribosomal structure" at* 6th Polish - German Symposium on Pharmaceutical Sciences, Düsseldorf, Germany, May 20-21, 2011
- Presented poster titled "*Structural and energetic aspects of oxazolidinones binding to the ribosome and factor Xa" at* BioStruct MasterClass 2010, Heinrich Heine University, Düsseldorf, Germany, September 6-9, 2010.

Abbreviations

DNA	deoxyribonucleic acids
RNA	ribonucleic acid
S	Svedberg unit
mRNA	messengerRNA
rRNA	ribosomal RNA
tRNA	transfer RNA
MDa	Megadaltons
A site	aminoacyl site
P site	peptidyl site
E site	exit site
PTC	peptidyl transferase center
MRSA	*methicillin-resistant Staphylococcus aureus*
VREF	*vancomycin-resistant Enterococci faecium*
PDB	protein data bank
SBDD	structure-based drug design
MD	molecular dynamics
MM-PBSA	molecular mechanic Poisson Boltzmann surface area
RESP	restrained electrostatic potential method
PME	particle mesh Ewald
QHA	quasi harmonic analysis
RMSD	root mean square deviation
RMSF	root mean square fluctuations
IC_{50}	translational inhibitory activity

List of abbreviations of ribosomal structures

D. radiodurans	*Deinococcus radiodurans*
H. marismortui	*Haloarcula marismortui*
D50S	50S subunit from *D. radiodurans*
E50S*	50S subunit extracted from 70S structure from *E. coli*
H50S	50S subunit from *H. marismortui*
T50S*	50S subunit extracted from 70S structure from *T. thermophilus*
T.thermophiles	*Thermus thermophilus*
M. smegmatis	*Mycobacterium smegmatis*
E. coli	*Escherichia coli*

Abstract

The ribosome is a ribozyme that catalysis the mRNA-directed protein synthesis. Prokaryotic ribosomes are composed of two unequal subunits (30S and 50S). These subunits contain several important functional sites that act as potential antibiotic targets. One of them is the peptidyl transferase center (PTC) located in the 50S large ribosomal subunit. The PTC is a target for various antibiotics used in the clinics such as erythromycin, clindamycin, and chloramphenicol. The ever increasing emergence of multi-drug-resistant bacteria warrants the need to continuously identify new antibiotics.

Oxazolidinones represent one of the few new chemical classes of antibiotics that have been introduced in the clinics over the past 40 years. Linezolid, the only member of this class approved by the FDA, shows excellent activity against major Gram-positive bacteria. The available co-crystal structures of linezolid with the large ribosomal subunit of *Deinococcus radiodurans* (D50S) and *Haloarcula marismortui* (H50S) provide static views of the binding processes but do not reveal the dynamics and energetics involved with antibiotics binding [24, 25].

In order to understand determinants of binding and factors that give rise to selectivity and the resistance development due to mutations for the first time, computational expensive molecular dynamics (MD) simulations in combination with MM-PBSA free energy calculations of oxazolidinones; (linezolid, radezolid and the structurally related drug rivaroxaban) bound to D50S and H50S were performed.

Our results provide a remarkably good agreement of the computed relative binding free energy with selectivity data available from experiment for linezolid. Moreover, structural data as well as energetic analysis shows that binding of radezolid to H50S is more favorable over D50S. Furthermore, the structurally related rivaroxaban does not bind to the ribosome reflected in its displacement from initial binding position as well as considerable positive $\Delta G_{effective}$. In line with literature reports, the structural decomposition identifies nucleotides 2055 and 2572 to be most important for antibiotic selectivity. With respect to the development of linezolid resistance, the analysis shows an unstable binding mode of linezolid in $H50S_{mut}$ over stable binding modes in $H50S_{wt}$ and D50S.The structural and energetic analysis identify U2504 and C2452 as spearheads that exert the most immediate effect on linezolid binding due to the remote double mutation. The results presented here are in-line with modifications of antibiotics belonging to the oxazolidinone class in clinical trials and FDA approved antibiotics binding to the ribosomal subunit.

1. Introduction

1.1 The antibacterial challenge: Discovery and resistance

The beginning of the twentieth century saw infectious diseases as the leading cause of death worldwide [1]. The discovery of antibiotics to combat infections led to a dramatic change not only to the treatment but to the fate of mankind [2]. Antibiotics are defined as chemical compounds that inhibit or kill microbes by interfering with the bacterial structure or function while exhibiting no effect on the eukaryotic host carrying the infectious agents [3]. The foundation of the antibiotic era was laid down by Paul Ehrlich and Alexander Fleming in the early 1900s and 1930s, respectively [4]. Ehrlich's idea of a "magic bullet" that selectively targets only disease-causing microbes and not the host led him to begin a screening program in 1904 to find a drug against syphilis [4]. In 1909, after screening many chemicals, compound numbered 606 was found to cure syphilis-infected rabbits. The drug was marketed under the name Salvarsan and was the most frequently prescribed, until it was replaced by penicillin [5]. However, sulfonamide drugs were the first antibiotics to be used systemically, and paved the way for the antibiotic revolution in medicine. The first sulfonamide, trade-named Prontosil, was a prodrug whose experiments began in 1932 in the laboratories of Bayer AG (Figure 1). Serendipitous discovery of penicillin in the year 1942 marked the beginning of the golden age of antibiotic discovery [6]. This era saw the discovery of new classes of antimicrobial agents being developed one after the other; chloramphenicol and tetracycline in 1949, aminoglycosides in 1950, glycopeptides in 1958, and quinolones in 1962. Years between 1962 and 2000 saw an innovation gap, post which started the "beginning of med-chem" era that led to the discovery of oxazolidinones in 2000 [5], followed by lipopeptides in 2003, mutilins in 2007, fidaxomicin in 2011 and diarylquinolones in 2014 (Figure 1) [7].

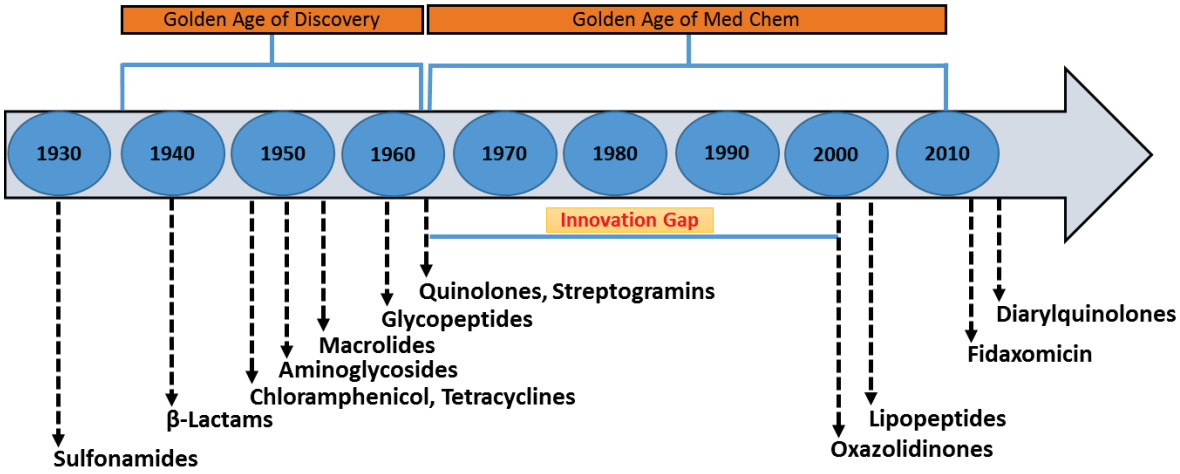

Figure 1: Discovery and development of antibiotics with time.

The origin of antibiotics can be natural as well as by chemical synthesis. Antibiotics can be classified based on the bacterial spectrum they are effective against broad (antibiotics acting against a wide range of disease causing pathogens) *versus* narrow (antibiotics which are effective against a specific family of pathogen), or the route of administration (injectable *versus* oral *versus* topical), or the type of activity (bactericidal *versus* bacteriostatic) they possess. A bacteriostatic antibiotic prevents the growth of bacteria, while a bactericidal antibiotic kills the bacteria [5, 8]. However, the most useful classification from a drug discovery scientist's point of view is based on the chemical structure and the mode of action. Antibiotics within a structural class generally show similar patterns of effectiveness.

Although there are almost 200 conserved essential proteins in bacteria, the number of exploited targets is still very small. Most antibiotics agents used for the treatment of bacterial infections act according to their principal mode of actions. I) inhibition of cell wall biosynthesis, e.g., as β-lactams (penicillinase); II) inhibition of protein synthesis, e.g., aminoglycosides (streptomycin), chloramphenicols, macrolides (erythromycin), tetracyclines and oxazolidinones (linezolid); III) interference with nucleic acid synthesis, e.g., fluoroquinolones, rifampin and fidaxomicin; IV) inhibition of metabolic pathway, e.g., sulphonamides and folic acid analogues; V) disruption of bacterial membrane structure, e.g., lipopeptides (deptomycine); and VI) inhibition of F_1F_o-ATPase, e.g., Diarylquinolines (bedaquiline). Figure 2 depicts various antibiotics and their targets [5, 8].

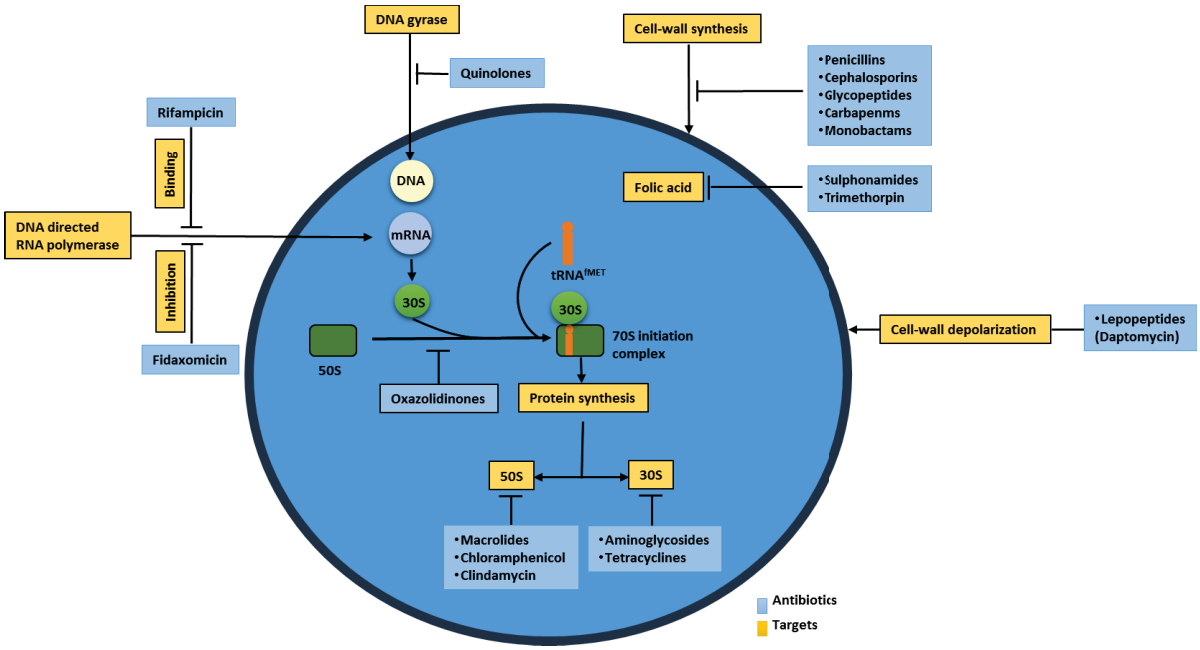

Figure 2: Antibiotics acting at different targets.

Bacterial pathogens have risen beyond human imagination and have utilized their genetic capacities to incapacitate antibiotics targeted against them. Clinically significant resistance can develop after months to years post the introduction of an antibiotic. Microbial pathogens can acquire resistance via following main mechanisms: I) the organism may acquire genes encoding enzymes, such as β-lactamases, that destroy the antibacterial agent before it can have an effect. II) bacteria may acquire efflux pumps that extrude the antibacterial agent from the cell before it can reach its target site and exert its effect. III) bacteria may acquire several genes for a metabolic pathway which ultimately produces altered bacterial cell walls that no longer contain the binding site of the antimicrobial agent [9]. The introduction of new antibiotics has not kept pace with the increasing rate of resistance, leaving clinicians with fewer treatment options. This problem reiterates the continuous and urgent need to develop newer, selective and effective antibiotics [10].

Developing newer antibiotics that act by distinct mechanisms of action have a greater potential in combating multi-drug-resistances, wherein several species of microbes become resistant to multiple antibiotics. This is one of the major global challenges of modern antibiotic drug discovery to understand the reasons of resistance development and to develop selective antibiotics that act at a particular site of action [11].

There has been a decrease in the field of antibiotics in the past few years. The decreasing interest in antibiotics in the pharmaceutical sector is one aspect that is responsible for the rise

in difficulty to treat bacterial infections. For instance, in 2004, merely 1.6% of the drugs in clinical development across the globe's 15 biggest drug firms were antibiotics. This resulting decrease in output of antibiotics can be accorded due to many reasons. Firstly, the norms pertaining to antibiotics are for limited time frames which make production of antibiotics less profitable compared to production of other drugs that are produced to treat other recurring sicknesses. Additionally, the new drugs are prescribed in combination with existing antibiotics in order to treat bacterial infections. This policy assists delay in antibiotics discovery and development. Furthermore, the profit is also limited due to too many generic rivals and the unavoidable development of bacterial resistance. Also, the impediments in form of rules have limited the interest of major pharmaceutical firms. The tolerance of negative side effects has off late been reduced for several drug groups which also include antibiotics. The approval needs during the clinical trials have risen in many instances from exhibition of non-inferiority to superiority and many a times the absence of proper trial directives for antibiotics, especially are a cause for limited growth of the sector. The pharmaceutical industries have to deal with several paradoxes wherein, while the federal agencies demand antibiotic development, several other federal agencies introduce policies that restrict the development that is needed in the first place. The above aspects have resulted in investment in the antibiotic sector being too dangerous. In fact an approximate investment of around $1.7 billion per drug, with limited revenues in return has made this an unprofitable venture for many antibiotic firms [148].

1.2 The bacterial ribosome as a major target for antibiotics

Many clinically useful antibiotics exert their antimicrobial effects by blocking protein synthesis on the bacterial ribosome, and hence it is not surprising that ribosome presents one of the major targets for antibiotic's action. The ribosome is a "ribozyme" that synthesizes proteins in all kingdoms of life by translating genetic information encoded in the messengerRNA (mRNA) [12]. Bacteria have comparatively smaller ribosomes with the sedimentation coefficient of 70S (where S stands for Svedberg units), and a molecular weight of $2.7x10^6$ Daltons. Each of the 70S ribosomes comprises a small (30S) and a large (50S) subunit (Svedberg measures are not additive because the sedimentation rate depends on both mass and surface area). The 70S ribosomes contain proportionally more RNA than protein [13, 14].

The two un-equal subunits (50S and 30S) associate during the initiation phase of translation. The 30S subunit contains the messenger decoding site where the interaction between codons of the ribosomalRNA (rRNA) and the anticodon of mRNA determines the amino acids assembly resulting in a specific protein sequence. It is composed of 16S rRNA and 21 protein chains. On the other hand, the 50S subunit, which is composed of 5S and 23S rRNAs and 34 protein chains, has three distinct binding sites for transfer RNA (tRNA), which is a small RNA chain (73-93 nucleotides) that transfers a specific amino acid to a growing polypeptide chain: the A site that accepts the incoming aminoacylated tRNA; the P site that holds the tRNA with the emerging poly-peptide chain; and the E site that carries the deacylated tRNA, which later leaves the ribosome. The peptide bond formation occurs at the peptidyl transferase center (PTC) [15]. The ribosomal PTC is the catalytic heart of the ribosome, which plays a fundamental role in the protein synthesis and is a part of the large ribosomal subunit 50S. Its primary function is to covalently link amino acids into polypeptides via peptide bond formation [16]. Besides the above components, two protein factors play important roles in the translation: I) protein elongation factor Tu (EF-Tu), which delivers the aminoacylated-tRNAs to the ribosome and II) protein elongation factor G (EF-G), which moves the assembly line device along its mRNA subsequent to the peptide-bond formation. EF-Tu delivers aminoacyl-tRNA molecules to the ribosome and leaves upon hydrolysis of guanosine-5'-triphosphate (GTP) only when the correct cognate tRNA has been delivered. EF-G, which is also GTP-driven, facilitates the translocation of tRNA and mRNA after peptide-bond synthesis [15, 17-19]. A number of antibiotics inhibit growth of microorganisms by binding to the PTC, the decoding site and the protein exit tunnel. For example oxazolidinones (such as linezolid and radezolid) bind to the A-site of the 50S subunit thereby preventing the binding of aminoacyl tRNA [6, 20, 21]. Antibiotics like aminoglycosides (e.g., paromoycin, streptomycin, and tobramycin) bind at the decoding site of the 30S subunit and inhibit protein synthesis. Macrolides (e.g. azithromycin, erythromycin, and roxithromycin) that prevent the elongation of nascent polypeptide chain (Figure 3) [15].

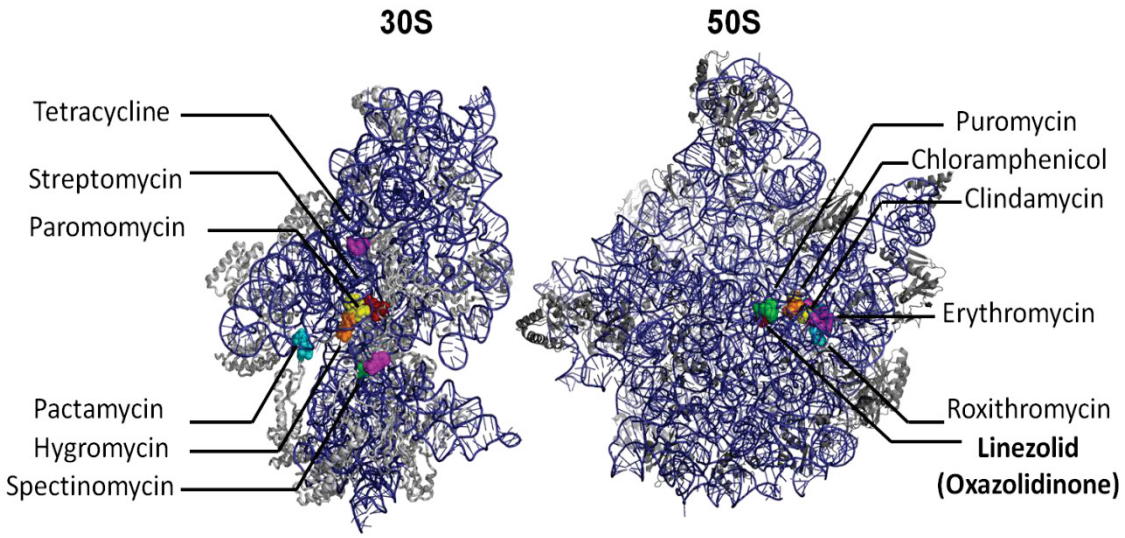

Figure 3: Site of action of various antibiotics at the small (30S) and large (50S) ribosomal subunit.

1.3 Oxazolidinone antibiotics

Even after several decades of research and huge investments, very few classes of antibiotics have been approved by the Food and Drug Administration (FDA) in the past 30 years. The last set of synthetic antibiotics that entered the market was in the year 2000 and belonged to the oxazolidinone class (Figure 1) [22].

The oxazolidinones indicate a new group of antimicrobial agents that have a distinct chemical framework, a five-membered heterocyclic ring forming the core, and are effective against gram-positive pathogenic bacteria. Oxazolidinone antibiotics bind and/or inhibit both archaeal and bacterial ribosomes but do not interact with human cytoplasmic ribosomes [22]. They exhibit a mechanism of inhibiting protein synthesis by preventing the binding of aminoacyl tRNA at the A-site (Figure 4A). They display bacteriostatic activity against many important pathogens, including methicillin-resistant *Staphylococcus aureus* (MRSA), vancomycin-resistant *Enterococci faecium* (VREF), and penicillin- and cephalosporin-resistant *Streptococcus pneumoniae* and are used to treat skin, soft tissue and respiratory tract infections [23].

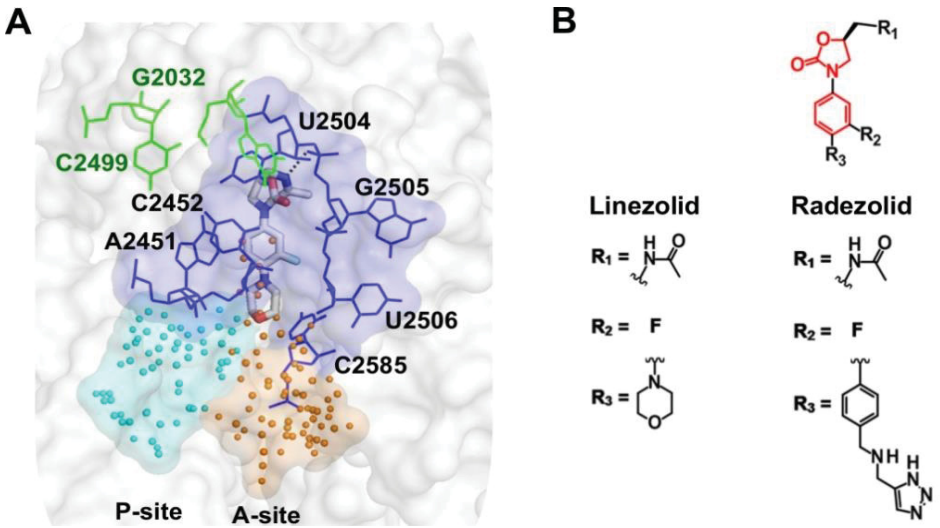

Figure 4: **Binding site of oxazolidinone antibiotics in the 50S ribosomal subunit and investigated oxazolidinone derivatives.** (A): Close-up view of binding site of linezolid within the 23S RNA; nucleotides that form the first shell residues around the antibiotic are depicted in blue colour; nucleotides that upon mutation result in antibiotic resistance are shown in green colour; A-site as well as P-site are shown in surface dot view; a hydrogen bond is shown as dotted line between the phosphate group of G2505 and the acetamide NH group of linezolid (B): Chemical structures of investigated oxazolidinones: linezolid, radezolid.

In the present times, many common gram-positive pathogens (for instance *Staphylococcus aureus*, *Streptococcus pneumonia,* and *Enterococcus*) are becoming more and more resistant to antimicrobial agents. Linezolid (Figure 4B) was the first oxazolidinone that was approved for clinical use. Linezolid exhibits *in vitro* activity (usually bacteriostatic) against several crucial resistant pathogens. The clinical trials have validated the action of linezolid in the setting of pneumonia, skin, and soft-tissue infections, and infections that take place due to vancomycin resistant enterococci. Linezolid is also a great alternative to glycopeptides and streptogramins. It can be effectively used to treat serious infections that occur on account of resistance to gram-positive organisms [24, 25].

The crystal structures of linezolid bound to 50S subunits both from an Archaeon *Haloarcula marismortui* (H50S) (Figure 4A) and bacterium *Deinococcus radiodurans* (D50S) were solved in 2008 [24, 25]. Archaeal ribosomes are considered more "eukaryotic-like" with respect to their antibiotics specificity, i.e., they possess typical eukaryotic elements at the principal antibiotic target sites and require much higher than clinically relevant antibiotic concentrations for binding. This holds true also for the oxazolidinone class of antibiotics: for co-crystallizing linezolid with the eubacterial D50S, a concentration of 5 μM

was required, while a 1,000-fold higher concentration was required for co-crystallization with the archaeal H50S. Furthermore, in a functional assay using ribosomes isolated from *S. aureus*, a eubacterium, a translation-inhibitory activity of IC_{50} of 0.9 μM was measured for linezolid, whereas in the case of H50S, an IC_{50} of 4.96 μM was found (E. M. Duffy, personal communication) [119].

Species-selectivity is the key to the antibiotics effective therapeutic use. In the case of development of new ribosomal antibiotics, the issue of selectivity (pathogens *versus* humans) is of particular importance because of almost universally conserved RNA and protein sequences and an almost identical function of the ribosomes of different species [27]. Still, by exploiting subtle structural changes within the antibiotic binding sites of prokaryotic and eukaryotic ribosomes, high levels of selectivity can be achieved [28]. As one of the most subtle changes, the exchange of adenine and guanine can dictate the preference of antibiotic binding: interactions between paromomycin, an aminoglycoside antibiotic, and the bases A1408 and G1491 in the A-site of bacterial ribosomes cannot be formed in human ribosomes because the bases are reversed to G and A [29]. Even though the nucleotides that form the linezolid binding site are universally conserved among ribosomes, there exists structural and dynamical differences in the critical residues that govern the species-specific selectivity [21].

Not long after the commercial release of linezolid, oxazolidinone-resistant strains of MRSA and VREF began to appear in the clinic [23, 29]. Most of these mutations cluster around the highly conserved nucleotides that form the PTC [25, 29]. These mutations are located in the second or even third shell, far away from the ligand binding site (~10 – 15 Å) and, thus, do not directly interact with the drug. Interestingly, out of 10 mutations known to give rise to linezolid resistance in bacteria and archaea, the nucleotides corresponding to two of these mutations, G2032C and C2499U (*Escherichia coli* numbering used throughout the thesis) are already present in the human 28S rRNA (Figure 4A) [23]. Recently, it has been reported that these single mutations, i.e., G2032C or C2499U, do not lead to a significant reduction in linezolid susceptibility [25].

The co-crystal structures of linezolid with D50S [24] and H50S [25] provided first insights into the structural basis of oxazolidinone activity. These complexes provide crucial insights into the binding sites, binding modes, and mechanism of action of these antibiotics (Figure 4A and 5). This creates possibilities for utilizing rational structure-based drug design (SBDD) techniques not only for improving existing antibiotics by chemical modifications in

order to achieve higher binding affinity and selectivity but also for discovering new classes of anti-bacterial drugs. However, structure determination by X-ray crystallography only provides *static* views of the binding processes but does not reveal (changes in) the *dynamics* associated with antibiotics binding or the *structural and energetic determinants* of binding. Theoretical and computational approaches such as molecular dynamics (MD) simulations in combination with free energy calculations are suitable to fill this gap. The aim of this thesis is to investigate the determinants of binding, resistance development, and selectivity of antibiotics belonging to the oxazolidinone class, in particular linezolid, its derivative radezolid, and the structurally related oral anticoagulant drug rivaroxaban in complex with H50S and D50S by means of MD simulations together with binding free energy calculations (Figure 5).

2. Current computational state-of-the-art techniques used for antibiotic design

The present status of antibiotic development needs major reforms due to ever increasing resistance development. There is an urgent need to design and develop newer selective antibiotics that are effective against a particular pathogen. A continuous increase of computational power, efficient treatment of long-range electrostatic interactions [31], and significant improvement in parallelization [32] have made all-atom MD simulations of large biomolecules like the ribosomal complex with 2.64×10^6 atoms possible. Using targeted MD simulations, the conformational change of the ribosome for accommodating tRNA during decoding has been simulated [32]. In another impressive study, the thermodynamics of the ribosomal decoding site and its interaction with the antibiotic gentamicin has been simulated in explicit solvent [33]. In this study, the simulations have been performed at the Advanced Simulation and Computing Q machine at Los Alamos National Laboratory using 1024 and 480 processors, respectively. The study reveals that the decoding bases flip on a timescale faster than that of gentamicin binding, supporting a stochastic gating mechanism for antibiotic binding, rather than an induced-fit model where the bases only flip in the presence of a ligand. The study also explored the nonspecific binding landscape near the binding site and reveals that, rather than a two-state bound/unbound scenario, drug dissociation entails shuttling between many metastable local minima on the free-energy landscape.

In another study, due to the large size of the ribosomal complex, a multiscale approach wherein MD simulations of ≈80,000 atoms cropped out from the *H. marismortui* large subunit was implemented to study the interactions between components of the ribosome tunnel and different amino acid side chains and ions [34]. Furthermore, an all-atom MD simulation on 128 CPUs was carried out on a 70S ribosome with and without the nascent polypeptide chain inside the ribosomal exit tunnel [35]. Modeling of the nascent chain in the tunnel shows that the extended loops of L4 and L22 partially hinder the passage of the polypeptide. Given that the analyzed trajectory has only a length of 2 ns, it remains unclear whether the proposed gating mechanism is biased by the starting configuration.

Regarding antibiotics binding to the ribosome, MD simulations were performed for a set of aminoglycosides bound to the RNA in the A-site. Binding free energy, essential dynamics, and hydration analyses have been conducted to characterize the energetics and dynamics of the binding for each of the antibiotic in the set [36]. In this study, several dynamic models were built with reasonable binding free energies showing good correlation

with the experimental data. Moreover, hydration analysis detected some long residence water molecules W8 and W49 sites around the U1406.U1495 pair, which are found to be important in molecular recognition. In addition, hydration sites with long residence times were identified between the ring III of two 4,6-linked antibiotics (tobramycin and kanamycin) and phosphate oxygen atoms of G1405/U1406. These findings could further be explored for rational drug design.

Most recently, interactions between the 50S subunit of a bacterial ribosome and the antibiotic sparsomycin and five analogs were investigated by calculating absolute binding free energies and characterizing conformational dynamics. The standard binding free energies of the complexes were computed using free energy perturbation molecular dynamics (FEP/MD) simulations with explicit solvent. The correlation coefficient between calculated and measured binding free energies was 0.96, and the experimentally observed ranking order for the binding affinities of the six ligands is reproduced. However, while the calculated affinities of the strong binders agree well with the experimental values, those for the weak binders are underestimated [37].

In one publication, the impact of ribosomal modifications on the binding of the ketolide antibiotic telithromycin was investigated using a combined grand-canonical Monte Carlo/MD simulation approach [38]. In this study, the impact of macrolide resistance development due to mutation of A2058 to G or methylation by Erm methyltransferase of the exocyclic N6 of A2058 has been investigated. Due to computational expediency, the ribosomal system was truncated to a 40 Å radius spherical system centered on the antibiotic, and150 ns of MD simulations have been carried out for both the wild type as well as the mutant *E.coli* 50S ribosomal subunit. The results of the study emphasize on 1: Increasing the hydrogen bonding interactions with adjacent nucleotides in the binding site, leading to the enthalpic gain, and 2: Increasing the flexibility of the heterocyclic ARM of telithromycin for entropy gain.

In another study, the role of the cofactor for triggering translational arrest for the controlling expression of important genes including macrolide antibiotic resistance genes has been investigated [39]. MD simulations were carried out to understand the drug-dependent structural link between the nascent peptide exit tunnel (NPET) and the PTC of the drug-free and erythromycin-bound *E.coli* ribosome, with the simulation run ranging from 70 to 273 ns. The results of the study showed that the antibiotic induces stalling in the NPET even without

significant contacts with the peptide, by allosterically altering the peptidyl transferase center. The study provided evidence of an allosteric link between the NPET and PTC showing how binding of an antibiotic in the NPET predisposes the ribosome for the stalling when translating specific amino acid sequences.

In an another interesting study, effective *in-silico* predictions for new oxazolidinone antibiotics using force field simulations of antibiotic-ribosomal complexes supervised by experiment and electronic structure methods has been investigated [40]. MD simulations were carried out on the truncated ribosomal linezolid complex. $\Delta\Delta E_b$ value which denoted a more favorable interaction of linezolid with the ribosome was computed. It represents the binding enthalpy relative to linezolid considered as the zero point. AMBER and OPLA-AA force-fields were evaluated by running extensive Monte Carlo (MC) conformational scans for isolated linezolid in order to find out if the particular potential function is able to reproduce 1) the unbound and 2) the bioactive linezolid conformation. The AMBER force field emerged as better in comparison to the OPLS-AA in calculating the global minimum of linezolid bioactive conformation. Moreover, the AMBER force field produces a homogeneous distribution of the low energy conformation, whereas the OPLS-AA low-RMSD conformations are clustered in a confined area. Furthermore, the stereoselectivity of (*R*)-linezolid has been rationalized on an atomic level of resolution using computational methods by monitoring carefully the critical hydrogen bonds within the binding region. $\Delta\Delta E_b$ values were used to rank order the experimental compounds; and it correlated well with the MIC values. Finally, new linezolid derivatives have been designed based on the model and are currently being synthesized and will be tested for biological activities in the future. None of the above studies however, investigated the determinants of binding, specificity and the long-range influence of mutation and hence resistance development for antibiotics binding to the large ribosomal subunit.

3. Molecular dynamics simulations: Background and theory

Molecular dynamics (MD) simulations at the classical mechanical level are at present the most appropriate way to explore the dynamics and energetics of complex biological molecules. In MD simulations, Newton's equations of motion are solved by numerical integration [41]. The simulations provide a dynamic picture starting from a static input structure of a molecule and, therefore, yield deepened insights into the relationship between molecular structure, dynamics, and function. MD simulations result in a trajectory which

specify the position and velocity of the particles in a biomolecule and how they change with time. Like every method MD simulations also have its own advantages and disadvantages. As such, it provides an in-depth view of the intermolecular interactions at an atomic level but suffers from two main limitations, i.e., the insufficient sampling and force field inaccuracies [42, 43, 44]. Several recent reviews describe the emergence of new sampling methods along with latest improvements in force field [45]. In the following section, methodological developments for MD simulations related to force fields and sampling issues are summarized.

3.1 Force fields

The potential energy of the system is described by the following equation, which contains the functions that preserve the essential nature of molecules in condensed phase (eq. 1).

$$E_{pot} = \sum_{bond} K_r (r - r_{eq})^2 + \sum_{angle} K_\theta (\theta - \theta_{eq})^2 + \sum_{dihedrals} \frac{Vn}{2}(1 + \cos[n\phi - \gamma]) + \sum_{i<j}^{atoms} \frac{A_{ij}}{R_{ij}^{12}} - \frac{B_{ij}}{R_{ij}^{6}} + \sum_{i<j}^{atoms} \frac{q_i q_j}{\varepsilon R_{ij}} \quad (1)$$

The first three terms are intra-molecular or bonded terms and describe the bond, angle and dihedral energy for the atoms in the same molecules. The last two terms describe the intermolecular or non-bonded terms which are calculated between all pairs of atoms residing in different molecules or atoms within the same molecule but separated by at least three bonds. The van der Waals interactions are modeled by a 6-12 Lennard-Jones potential, and the electrostatic potentials are calculated using Coulomb's equation [41-49]. The functional form, the parameters k_r, k_θ, Vn, A_{ij}, B_{ij} and the partial atomic charges (q) make up a force field [50].

CHARMM and AMBER force fields are the most prominent and popular ones for nucleic acid simulations. Both force fields share a similar functional form but differ in parameterization [51, 52]. It must be noted that parameterization of nucleic acid force fields is probably more challenging than parameterization of protein force fields due to a more complex balance of forces in nucleic acids. By the first half of the 1980s, enough experience had accumulated with earlier parameterizations for several groups to begin fairly systematic projects to develop a new generation of force fields. The earliest of these efforts were still done at a time when the limited power of computers made it attractive to not include all hydrogen atoms as explicit force centers. The importance of hydrogen bonding, however, led many investigators to adopt a compromise whereby polar hydrogens were explicitly represented but hydrogens bonded to carbon were combined into united atoms. A widely used

force field at this level was developed in 1984 in the Kollman group and was incorporated into the Amber molecular mechanics package [51].

In the context of force fields for RNA MD simulations, the ff99 force field64, [92] was the force field of choice for several years in the Amber program package [77]. The ff99 force field64, [92], as well as other current nucleic acid force fields, performs well in describing canonical DNA and RNA helices, while they might show different success for more complex RNA molecules. The most recent force field developed by the Orozco group named as the Barcelona Supercomputing Center (BSC), the bsc0 modifications, published in 2007 is a further improvement over parm99 by updating the α and γ dihedrals. This corrected α overpopulated in gauche+ conformations and γ overpopulated in trans conformations. Furthermore, bsc1 was released in 2015 and includes the bsc0 modifications and additional modifications to the sugar pucker, the χ glycosidic torsion, and the ε and ζ dihedrals [52, 53]. With the increase in computational power, and consequently extending simulation times, a sudden irreversible transition of RNA helices to ladder like structures was observed in some simulations [140]. In order to avoid the formation of such non-physiological structures, a reparameterization of the χ-dihedral was developed and was published as parmχOL3 [141]. The currently recommended combination is to use the ff99 force field together with the bsc0 and the as parmχOL3 refinements [77]. In the context of RNA simulations in Amber, this combination is also referred to as ff10, ff12 (in Amber12), and ff14 (in Amber14) [77].

As with Amber, the CHARMM program (Chemistry at HARvard using Molecular Mechanics) [54] was originally developed in the early 1980s and initially used an extended atom force field with no explicit hydrogens. By 1985, this had been replaced by the CHARMM19 parameters, in which hydrogen atoms bonded to nitrogen and oxygen are explicitly represented, while hydrogens bonded to carbon or sulfur are treated as part of extended atoms [54]. As with the contemporaneous Amber 1984 united-atom parameterization, the CHARMM19 values were developed and tested primarily on gas phase simulations. However, the CHARMM19 potential seems to do well in solvated simulations and continued to be used for peptide and protein simulations only; this is in contrast to the Amber force field, which is now being widely used for transmembrane proteins with membrane models. In addition, the CHARMM19 values have often been used in conjunction with a distance-dependent dielectric constant as a rough continuum solvation model. Currently, the all-atom model in CHARMM27 is used for nucleic acid simulations [55, 56].

3.2 Free energy calculation methods

3.2.1 MM-PBSA (Molecular Mechanic Poisson-Boltzmann Surface Area)

Free energy calculations have increasingly become part of the standard methods for prediction of binding affinities of small drug molecules, evaluation of relative stabilities of large biomolecular structures, and intricate biomolecular procedures such as protein folding. The calculations can be performed by computationally expensive free energy perturbation (FEP) and thermodynamic integration (TI). Both the techniques need high computational cost to explicitly treat solvent and to determine the differences in free energies of the two states based on simulations that are carried out at intermediate points along a transition path from one state to another [57-60, 78]. The computational cost can be reduced by considering only the end-point states in the free energy calculations. One of the most preferred solvent prototypes relies on the Poisson-Boltzmann (PB) equation, at least as far as electrostatic impacts are concerned, and on the description of a surface tension energy relative to the solvent accessible (SA) surface area considering the inclination of nonpolar parts of a molecule [61-65]. The approach has been used on more than hundred studies to determine the free energies of molecular systems w.r.t. evaluating docking poses, determining structural stability, predicting binding affinities and hot-spots [66-73]. There are many benefits of executing molecular dynamics (MD) simulations by employing implicit in contrast to obvious solvent prototypes; these include quicker equilibration times, and less time for calculations. It is thus needed to investigate implicit solvent MD simulations and especially the MM/PSBA methodology [37, 77, 78, and 119].

In one of the studies the authors presented the results to interpret thermodynamics profiles from ITC in terms of individual energy contributions to binding computed by the MM-PBSA approach for amino-adamantine compounds inhibiting the M2 proton channel of influenza A [72]. The authors compare energy contributions that are accessible by both MM-PBSA and ITC. The trend in the effective binding energy computed by the MM-PBSA approach were highly consistent with the binding enthalpy and free energy determined by ITC measurements of >85% of all eight pairs of aminoadamantane compounds considered in the study. Since entropy contributions are more challenging, only 50% of the considered pairs matched the observed ITC measurements with MM-PBSA calculations. Entropy contributions due to the configurational entropy were computed using combined quasiharmonic and normal mode approached respectively [77, 119]. Furthermore, MM-PBSA approach provided information about the determinants of binding (e.g., in terms of

contributions by electrostatic and van der Waals energies or solvation) that were not available from ITC measurements. Such decomposition helps in linking thermodynamic profiles from ITC with structural causes, thus guiding decision making in lead optimization. The authors showed how computationally relatively inexpensive approach can therefore be highly useful for the design of further drug candidate for M2TM [72].

An excellent review by the author has discussed applications of MMPBSA to biomacromolecules [78]. The review discusses MM-PBSA application to study the stability of DNA, RNA and protein conformers in order to identify the native fold among the set of decoy structures or the fold that is most stable in a given environment. Furthermore, MM-PBSA free energy calculations help to identify the correct cysteine pairing in those cases where X-ray crystallography and nuclear magnetic resonance spectroscopy failed.

In another of the study the authors provided structural basis of antibiotic binding site in nisin resistant protein *Streptococcus agalactiae* COH1 (SaNSR) and the mechanism of substrate specificity [79]. Guided with mutagenesis studies together with MD simulations, revealed that SaNSR recognizes the lanthionine ring closest to the C-terminus of nisin and that this ring binds at one end of the catalytic tunnel, thereby determining the substrate specificity and ensuring the exact coordination of the nisin cleavage site at the catalytic site region. Since there is no crystal structure of SaNSR with bound nisin, a model of SaNSR/nisin complex was generated by integrative modelling. The model reveals that SaNSR binding to nisin is dominated by hydrophobic interactions. Within the protease core key residue forming a pocket that harbors both rings D and E were identified. In agreement with this model, mutation of these residues reduces the activity of SaNSR. Furthermore, water-mediated hydrogen bonds between backbone atoms of rings D and E and side chains were identified. Furthermore, per-residue decomposition of effective binding energies computed by the MM-PBSA approach identified Ile30 as key residue for nisin binding to SaNSR [79].

In yet another study, the authors presented the development of a computationally efficient method to approximate $\Delta S_{R/T}$ in terms of the reduction in translational and rotational freedom of the ligand upon protein−ligand binding (termed BEERT) and tested it successfully in binding affinity computations in connection with MM-PBSA effective energies describing changes in gas-phase interactions and solvation free energies [80]. The methodology differs at two major points: First, bound ligand poses are clustered based on

interactions with the protein rather than the structural similarity of the poses; Second, $\Delta S_{R/T}$ across multiple wells of the protein-ligand energy landscape in the bound state was computed as the weighted average of the single entropies associated with an individual well. The new method differs from the previous combinations of MM-PBSA effective energies with respect to approximations of $\Delta S_{config.}$, wherein the former method estimation is done using rigid rotor, harmonic oscillator approximation (RRHO) over flexible molecule (FM) approach used in the new method. Also the authors claim their approach to be highly computationally efficient with computing time of 45-90 s per complex [80].

Computational methods that combine molecular mechanics energy and implicit solvation models, such as Molecular Mechanics Poisson Boltzmann Surface Area (MM-PBSA), have been widely exploited in free energy calculations [81]. Compared with the rigorous methods such as free energy perturbation (FEP) [82] and thermodynamic integration (TI) [83], the MM-PBSA method is more computationally efficient. That is why the MM-PBSA approach was used in the course of this study to investigate the energetic determinants of binding of oxazolidinones to H50S. This method estimates the free energy of a molecule *x* as the sum of its gas phase energy (H^x_{gas}), solvation free energy (G^x_{solv}), and entropy (S^x) (eq. 2).

$$G^x(i) = H^x_{gas}(i) + H^x_{trans/rot} + G^x_{solv}(i) - TS^x(i) \quad (2)$$

H_{gas} and G_{solv} were averaged over snapshots of conformational ensembles [84]. The effective binding energy was computed as the difference of the average effective energies ($<H_{gas}> + <G_{solv}>$) of the complex and the receptor and ligand (eq.3).

$$\Delta G_{total} = < G_{complex}(i) > - < G_{receptor}(i) > - < G_{ligand}(i) > \quad (3)$$

Where $<\cdot>$ denotes an average over snapshots *i* taken from the MD trajectories. In the single-trajectory MM-PBSA approach, the snapshots are extracted from a single simulation of the complex [85]. Gas-phase energies $H^x_{gas}(i)$ are calculated by summing up contributions from internal energies, electrostatic energies, and van der Waals energies using the ff99SB modifications of the Cornell *et al.,*force filed [64, 92] force-field with no cutoff. Solvation free energies $G^x_{solv}(i)$ are computed as the sum of polar and non-polar contributions. The polar contribution was calculated using the Poisson-Boltzmann (PB) model [77]. The non-polar contribution to the solvation free energy due to cavity formation and van der Waals

interactions between the solute and the solvent was estimated by a solvent-accessible surface area (SA)-dependent term [86] (eq. 4):

$$G^{x}_{nonpolar}(i) = nSASA^{x}(i) + b \quad (4)$$

The $SASA^{x}(i)$ was determined with the LCPO method [87] as implemented in AMBER 10 using a surface tension proportionality constant of and γ was set to 0.005 kcal mol^{-1} A^{-2}.

3.2.2 Solvation Free Energy calculation: APBS

The polar contribution to the solvation free energy was determined using the PB approach [144] wherein the electrostatics contribution to solvation was calculated using the adaptive Poisson-Boltzmann Solver (APBS) [87]. It uses the finite difference method for the generation of accurate solutions to the PB equation. The electrostatic calculations were performed by employing an automatically configured sequential focusing multigrid procedure. In this procedure, a less accurate solution on a coarse finite difference mesh covering the entire ribosome is used to define the boundary conditions for more accurate calculations with a finer discretization of the ligand binding site [87]. The electrostatic potential for the ribosomal complex was obtained at a resolution of 0.19 Å [77].

3.2.3 Post-processing of MD trajectories

Once the MD simulations are carried out, the results are obtained in the form of large trajectories. These trajectories contain the basis information (3D coordinates, velocities) for each atom with respect to the simulation time. The very common techniques by which the structural analysis of generated trajectories is done are briefly summarized below.

A. Root-Mean-Square-Deviation (RMSD)

The Root-Mean-Square-Deviation is a standard measure of distance between two coordinate sets. It gives the average distance d between two position vectors a and b of N equivalent atoms separated in 3D space [77] (eq. 5):

$$\boldsymbol{RMSD} = \sqrt{\frac{1}{N}\sum_i d_i^2} = \sqrt{\frac{1}{N} \parallel a_i - b_i \parallel^2} \quad (5)$$

B. Root-Mean-Square-Fluctuation (RMSF)

The Root-Mean-Fluctuation describes the atomic positional fluctuations within a considered time period. It is calculated by averaging over atom (residue) i's deviation to it time averaged position [22, 88] (eq. 6):

$$\boldsymbol{RMSF} = \sqrt{\langle (r_i - \langle r_i \rangle)^2 \rangle} = \sqrt{\langle r_i^2 \rangle - \langle r_i \rangle^2} \quad (6)$$

The angle brackets $<\cdot>$ denotes a time average. The coordinates should be aligned to a common structure previously, to remove system-wide translational and rotational movements.

4. Aims and scope of the thesis

Understanding at the atomistic level the process of binding, selectivity and resistance development of small antibiotics binding to the large ribosomal subunit thereby inhibiting process of translation is very complicated and intriguing. The aim of the thesis is to provide these critical insights by taking oxazolidinone class of antibiotics as an example as these antibiotics bind to the highly conserved peptidyl transferase center in the ribosome. Technically challenging molecular dynamics simulations in combination with molecular mechanics Poisson-Boltzmann surface area (MM-PBSA) free energy calculations is applied on the oxazolidinones linezolid and radezolid bound to the large ribosomal subunits of the eubacterium D50S and the archaeon H50S. As a negative control structurally similar rivaroxaban, an oral anticoagulant drug was also considered in the study (Figure 5).

The first step of this work is to understand the binding and selectivity aspects of oxazolidinones linezolid, radezolid and rivaroxaban bound to the large ribosomal subunits of the eubacterium D50S and the archaeon H50S (Publication 1, Section 5). On the atomistic level, the analyses reveal an intricate interplay of structural, energetic, and dynamic determinants of the species selectivity of oxazolidinone antibiotics: A structural decomposition of free energy components identifies influences that originate from first and second shell nucleotides of the binding sites and lead to (opposing) contributions from interaction energies, solvation, and entropic factors. Furthermore, both the structural as well as energetic analysis proves rivaroxaban as a non-binder to ribosome.

The second part of this research work is focused to understand the development of antibiotics resistance due to mutation at positions 2032 or 2499 at the atomistic level (Publication 2, Section 6). The structural, dynamic, and energetic determinants reveal how remote mutations exert an influence on the susceptibility of a PTC antibiotic. The determinants are consistent in describing effects of a complex but balanced reorganization in the network of inter-nucleotide interactions that percolates from the mutation sites to the PTC. In particular, identifying cross-talk between the two main routes of information transfer, which could explain the experimentally observed synergy of the double mutation, goes beyond current knowledge on the structural basis for (cross-)resistance.

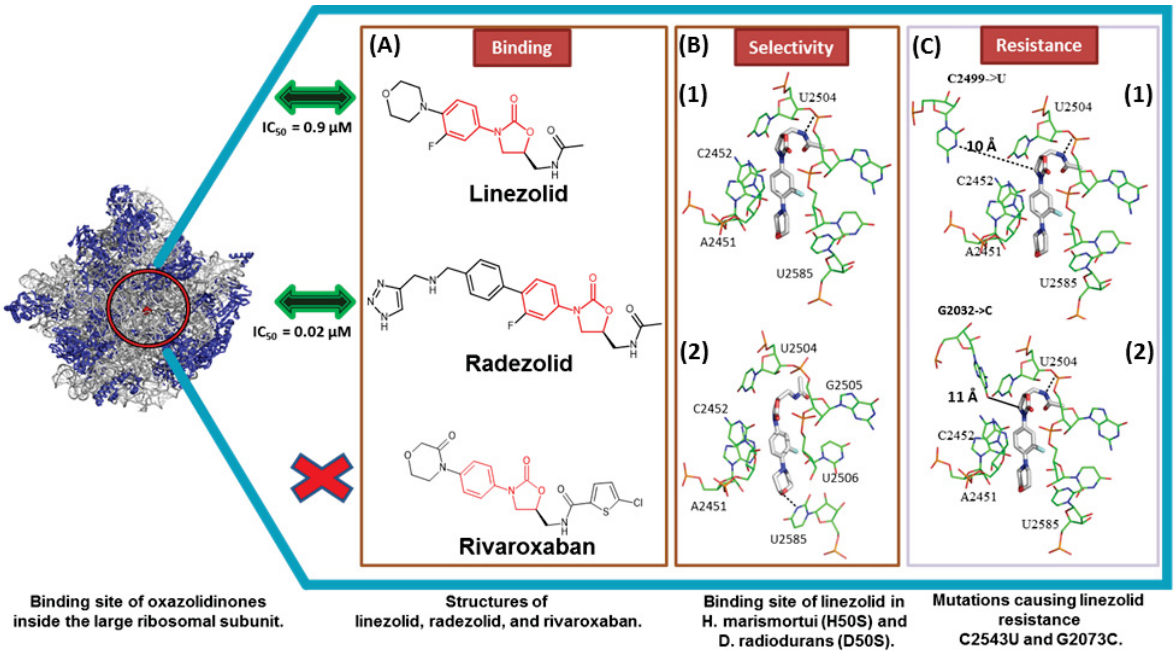

Figure 5: **Overall binding of oxazolidinone antibiotics in the 50S ribosomal subunit.** (A): Chemical structures of investigated oxazolidinones: linezolid, radezolid and rivaroxaban. (B): Close up view of the binding site nucleotides that form the first shell of residues around linezolid in H50S (1) and D50S (2). (C): Mutations of key residues that are located around 10 Å away from the binding site C2534U (1) and G2073C (2) in H50S

For the following Chapter, the text and figures have been taken and modified from the publication:

"**Jagmohan S. Saini,** Nadine Homeyer, Simone Fulle, Holger Gohlke, *Determinants of the species-selectivity of oxazolidinone antibiotics targeting the large ribosomal subunit* **Biol. Chem., 2013**, 1529-41."

5. Structural and energetic determinants of binding and selectivity of oxazolidinones to large ribosomal subunit

5.1 Introduction

Oxazolidinones represent one of two new chemical classes of antibiotics that have been introduced in the clinics over the past 40 years. Linezolid shows excellent activity against major gram-positive bacteria and is very effective in the treatment of infections of the respiratory tract and skin disorders [25]. The co-crystal structures of linezolid with the large ribosomal subunit of D50S, a eubacterium, [24] and H50S, an archaeon, [25] show that the antibiotic exerts its action by binding to the A-site of the peptidyl transferase center (PTC) and, thereby, hinders the proper placement of the incoming aminoacyl-tRNA (Figure 4A and 6B).

The co-crystal structures of linezolid with D50S and H50S provided first insights into the structural basis for the species-selectivity of the oxazolidinone family (Figure 5C) [24, 25]. As such U2585 forms a hydrogen bond with the morpholino ring of linezolid in the D50S but not in the H50S structure [24]. In contrast, the phosphate group of G2505 forms a hydrogen bond with the acetamide NH group of linezolid in the H50S but not in the D50S structure. Otherwise, the overall position of linezolid is similar in both species in terms of ring orientations and interactions (Figure 5C). Obviously, the origin for the large difference in the binding affinity of linezolid towards D50S or H50S cannot be deduced from structural data alone.

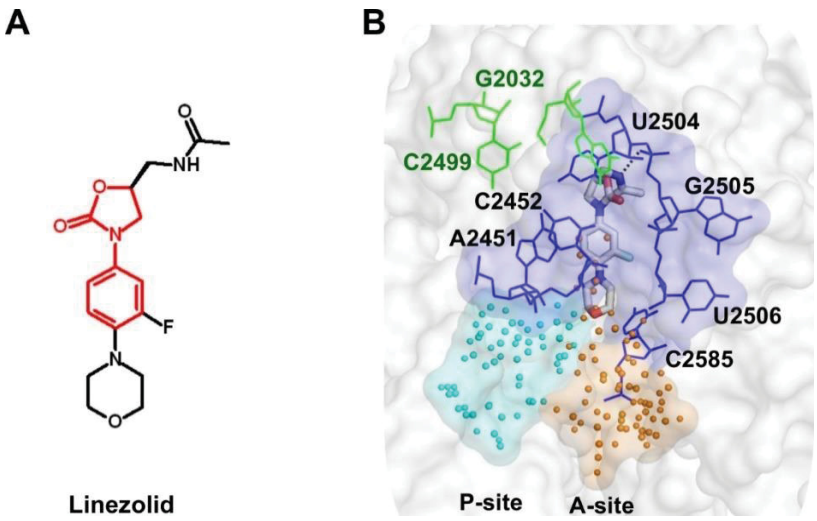

Figure 6: **Binding site representation along with key residues as well as A and P sites.** (A): Chemical structures of linezolid: the core of the molecule is shown in Red. (B): Close-up view of binding site of linezolid within the 23S RNA; nucleotides that form the first shell residues around the antibiotic are depicted in blue colour; nucleotides that upon mutations results in antibiotic resistance are shown in green colour; A-site as well as P-site are shown in surface dot view and finally a hydrogen bond in show as dotted line between the phosphate group of G2505 and the acetamide NH group of linezolid.

In order to provide a better understanding of the selectivity determinants of the oxazolidinone class of antibiotics, we have performed for the first time molecular dynamics (MD) simulations in combination with MM-PBSA free energy calculations of linezolid bound to D50S and H50S. Furthermore, the oxazolidinones radezolid and rivaroxaban were also investigated (Figure 4B).

Radezolid is a promising member of the oxazolidinone class of antibiotics, which has completed clinical trials [90]; http://melinta.com/pipeline/oxazolidinone-and-macrolide-programs/access dated: 13th Jan 2018), requires a 100-times lower concentration than linezolid to inhibit protein synthesis in eubacterial ribosomes [90], and shows an improved pattern of selectivity to bacterial ribosomes [91]. In contrast, rivaroxaban, an oral anticoagulant, does not bind to the ribosome although it is structurally related to linezolid and radezolid (ChEMBL, access date: 13th Jan 2018) [143]. Hence, rivaroxaban was used as a negative control in the course of this study. Overall, our analyses reveal an intricate interplay of structural, energetic, and dynamic determinants of the species-selectivity of oxazolidinone antibiotics.

5.2 Materials & methods

5.2.1 MD simulations of the oxazolidinone-50S systems

The molecular dynamics (MD) simulations were performed with the AMBER 10 suite of programs [77] together with the ff99SB force field [85, 92] for RNAs and proteins, and the general amber force field (GAFF) [93] for the ligands linezolid, radezolid, and rivaroxaban. Bonded parameters of the ligands were obtained using Gaussian 03 [94] and the Antechamber suite [95]. Atomic charges for the ligands were derived by the RESP procedure [96]. All Mg^{2+} (92 in H50S and 35 in D50S) and Zn^{2+} (2 in D50S) ions found in the crystal structures were considered for the MD simulations; non-bonded parameters for Mg^{2+} were taken from Åqvist [97] and for Zn^{2+} from Hoops *et al.* [98]. The starting conformations of D50S and H50S in complex with linezolid were obtained from the respective X-ray structures (PDB codes: 3DLL and 3CPW) [24, 25]. The crystal structure of H50S contains CCA-N-acetylphenylalanine (CCA-Phe), an analogue present at the P-site, that is absent in the D50S structure [24, 25]. Since it is established that the binding conformation of linezolid in the presence and absence of CCA-Phe does not differ significantly from the conformation in the structure of linezolid alone [24, 119], CCA-Phe was removed from the crystal structure before the system setup. Co-crystal structures of radezolid and rivaroxaban are unavailable; hence, they were obtained by modifying the linezolid complex structures. Protein chains 1, 2, and 3 containing C-alpha atoms only in the crystal structure of D50S were completed with the help of the Modeller software package [99] and the MacroModel module [100] of the Schrödinger software. Each complex was neutralized by adding Na^+ and Cl^- counter ions, and the systems were then solvated in a truncated octahedral periodic box of TIP3P water [101] with a distance between the edges of the box and the closest solute atom of at least 10 Å. This resulted in system size of ~8.5×10^5 atoms.

The particle mesh Ewald (PME) method was used to treat long-range electrostatic interactions [102], and a direct-space non-bonded cutoff of 9 Å was applied. The systems were initially minimized by 500 steps. Harmonic restraints with force constants of 5 kcal mol^{-1} $Å^{-2}$ were applied to all RNA, protein, and ligand atoms in all minimizations and the initial equilibration runs. After minimization the systems were heated from 100 K to 300 K using canonical ensemble (NVT) MD. The solvent density was then adjusted using isothermal-isobaric ensemble (NPT) MD. During equilibration it proved necessary to re-solvate the tunnel region of the large ribosomal subunit multiple times, as water molecules continued to fill voids initially present in the ribosomal structure. The force constants of the

harmonic restraints on the RNA, protein, and ligand atoms were then gradually reduced to zero over 300 ps of MD simulation in the NVT ensemble. In all MD simulations, a time step of 2 fs was used, and the lengths of bonds involving hydrogen atoms were constrained by the SHAKE algorithm [103]. Production simulations were performed employing a time constant of 2.0 ps for heat bath coupling. The production runs achieved lengths of 50 ns of which snapshots saved at 20 ps intervals during the last 20 ns (10 ns) were used for structural analysis (the calculation of effective binding energies and entropy contributions). The MD simulations were performed on the supercomputer JUROPA at the Jülich Supercomputing Center (JSC). All figures and images were generated by gnuplot [104] and pymol [105].

5.2.2 Structural analysis of MD trajectories

The 'ptraj' module of Amber 10 [77] was used for analyzing the root-mean square deviation (RMSD) between structure pairs, the root-mean square fluctuations (RMSF) about the mean position of atoms, and the formation of hydrogen bonds. For investigating structural deviations along the trajectories, RMSD of all residues of the oxazolidinone-50S complexes as well as RMSD of the "core" residues were computed with respect to the starting structures of the production run; for both RMSD calculations only the corresponding C-alpha (Cα) and phosphate atoms of the 50S structure were considered. The "core residues" were defined to be those residues with 90% lowest RMSF of all Cα and phosphate atoms. A visual inspection revealed that the excluded residues mainly belong to the stalk regions and not to the investigated binding site. RMSF values were calculated for the ligands after root mean-square fitting of the ligand atoms. For the calculation of the occupancy of hydrogen bonds, hydrogen bonds were defined by a distance cutoff of 3.2 Å and an angle cutoff of 120°.

5.2.3 Calculation of effective binding energies

In the single-trajectory MM-PBSA approach employed here, the snapshots were extracted from the trajectory of the complex simulation [75, 76, 78, 83, 84]. All water molecules were deleted as were all counter ions except Mg^{2+} and Zn^{2+} ions. Gas-phase energies (MM) $H^{x}_{gas}(i)$ were calculated by summing up contributions from internal energies, electrostatic energies, and van der Waals energies using the ff99SB [85, 92] force-field with no cutoff. Solvation free energies $G^{x}_{solv}(i)$ were computed as the sum of polar and non-polar contributions. The polar contribution was calculated using the Poisson-Boltzmann (PB) model as implemented in the Adaptive Poisson-Boltzmann Solver (APBS) [87]. A sequential-focusing multigrid procedure was applied where the 50S ribosomal complexes were initially encapsulated in a

coarser cubic grid with dimensions of 292 × 347 × 412 $Å^3$; then, a finer, cubic grid with dimensions of 25 × 25 × 25 $Å^3$ focused on the ligand region was applied. The electrostatic potential was obtained at a resolution of 0.19 Å. The continuum solvent dielectric constant was set to 80, and the solute dielectric constant was set to 11. The value of 11 for the solute dielectric constant has been found to be optimal in preliminary tests on oxazolidinone-H50S complexes. The dielectric boundary was defined by a probe sphere with a radius of 1.4 Å. For all PB calculations, the PARSE parameter set was applied, with a value of 2.0 Å [106] for phosphorus. A dielectric radius of 1.50 Å was assigned to both Zn^{2+} and Mg^{2+} ions [107]. The calculations were performed at 150 mM ionic strength with an ion exclusion radius of 2 Å [107].

The non-polar contribution to the solvation free energy was estimated by a solvent-accessible surface area (SASA)-dependent term (eq. 4). The SASAx(i) was determined with the LCPO method [108] as implemented in AMBER 10 [77], and γ was set to 0.005 kcal mol^{-1} A^{-2}.

5.2.4 Calculation of individual entropy contributions

Individual entropic contributions were calculated by quasiharmonic analysis [37, 77]. The convergence of the vibrational entropy estimates were checked by computing entropies based on snapshots from increasing segments of the last 10 ns of the MD simulations. While converged estimates were obtained for the ligand (drift: 0.05 kcal mol^{-1} for the last 1 ns Figure 7), estimates for the receptor did not converge anymore when residues of the second shell of the ligand binding site were considered (drift: 24.28 kcal mol^{-1} for the last 1 ns Figure 7). Thus, we computed vibrational entropy estimates for the receptor considering only first shell residues of the ligand binding site (drift: 5.52 kcal mol^{-1} for the last 1 ns; Figure 7). As a downside, vibrational entropy contributions from residues further away were neglected.

The difference in the change of the configurational entropy due to ligand binding to D50S *versus* H50S $T\Delta\Delta S_{D50S-H50S}$ was calculated according to (eq. 7)

$$T\Delta\Delta S_{D50S-H50S} = T\Delta S_{D50S} - T\Delta S_{H50S} \quad (7)$$

using T = 300 K. Considering that the change of the configurational entropy due to ligand binding to the ribosomal species *i* (with *i* = {D50S, H50S}) is (eq. 8)

$$T\Delta S_{,i} = TS_{i,complex} - TS_{i,receptor} - TS_{ligand} \quad (8)$$

the contribution of the unbound ligand TS_{ligand} cancels in (eq. 8). Furthermore, we assumed that the contributions of the unbound receptors $TS_{i,receptor}$ will be very similar given that the first shell residues are identical between both species. Hence, $TS_{i,receptor}$ was neglected when computing (eq. 8).The complex entropy $TS_{i,complex}$ was finally determined by (eqs. 9-10)

$$TS_{i,complex} = TS_{i,R,T,complex} + TS_{i,V,complex} \quad (9)$$

$$\approx TS_{i,R,T,V,ligand\ in\ complex} + TS_{i,V,receptor\ in\ complex} \quad (10)$$

with $TS_{i,R,T,complex}$ and $TS_{i,V,complex}$ being the rotational/translational and vibrational contributions, respectively. This sum was approximated by the sum of the total entropy of the bound ligand ($TS_{i,R,T,V,ligand\ in\ complex}$), computed by quasiharmonic analysis (QHA) after root mean-square (RMS) fitting of the first shell residues, and the vibrational entropy of the receptor in the bound state ($TS_{i,V,receptor\ in\ complex}$), determined by QHA for the residues in the first shell of the ligand binding site after RMS fitting of the residues in the second shell (eq. 10).

5.3 Results and Discussion

5.3.1 Overall stability of the oxazolidinone-50S complexes

We studied differences in oxazolidinone binding to D50S and H50S by all-atom explicit solvent MD simulations of the respective complexes of 50 ns length each. This leads to in total 300 ns of simulation time for systems of the size of ~8.5×10^5 atoms. For investigating structural deviations along the trajectories, the overall root mean-square deviation (eq. 5) as well as the RMSD of the "core" residues were computed with respect to the starting structures. (The term "residue" is used here for both amino acids and nucleotides.) The "core" residues were selected by regarding only those residues with the 90% lowest root mean-square fluctuations (RMSF) (eq. 6) of $C\alpha$ and phosphate atoms. Overall the RMSD of the "core" (Figure 7A) stabilized over the initial 30 ns of simulation time: The RMSD values of the "core" residues reach a plateau of 2-3 Å (4-5 Å) for the linezolid/radezolid-H50S (D50S) complexes (Figure 7A). These deviations are comparable to those found in related simulations [36, 37, 69] and suggest that for the "core" of the ribosome stable trajectories can be obtained already after a few tens of ns. The results of the RMSD analyses also point out that the nucleotides surrounding the binding site in the oxazolidinone-50S complexes do not undergo major structural rearrangements.

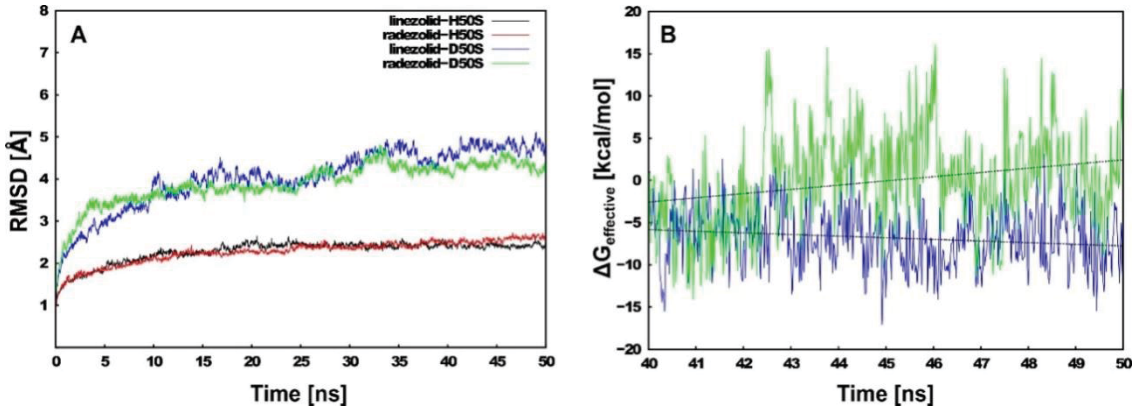

Figure 7: **Root mean square deviations and effective binding energies of oxazolidinone-50S complex over the entire simulation period of 50 ns.** (A): Root mean square deviation of C_α and phosphate atoms of the 'core-residues' along the MD trajectory of oxazolidinone-50S complex structures. RMSD is calculated with respect to the starting frame of the production run. The 'core-residues' are defined as the residues which show 90% lowest RMSF of the C_α and phosphate atoms. RMSD values for linezolid and radezolid in H50S are shown in black and red, and for linezolid and radezolid in D50S the RMSD values are depicted in blue and green, respectively. (B): Time series of effective binding energies calculated for 500 snapshots extracted in 20-ps intervals from the last 10 ns of MD simulations of linezolid-D50S (blue) and radezolid-D50S complexes (green). The drifts in the effective binding energies, determined from the slopes of the linear regression lines, are -0.19 kcal/(mol*ns) and 0.50 kcal/(mol*ns), respectively.

Consequently, the last 20 ns of MD trajectories were used for all subsequent structural analyses. However, in the energetic analysis, the effective binding energies showed significantly higher fluctuations in the 30- to 40-ns range than in the 40- to 50-ns range (Figure 8). Hence, for the energetic analyses only the last 10 ns were used. This ensured rather stable effective binding energies computed by the MM-PBSA approach as revealed from the time-series of these values (Figure 7B).The average drifts in the effective binding energies, as determined by the slopes of the linear regression lines, are -0.19 kcal mol^{-1} ns^{-1} (0.50 kcal mol^{-1} ns^{-1}) for linezolid (radezolid) in D50S. The magnitude of these drifts is comparable to those found for ligands binding to proteins [69].

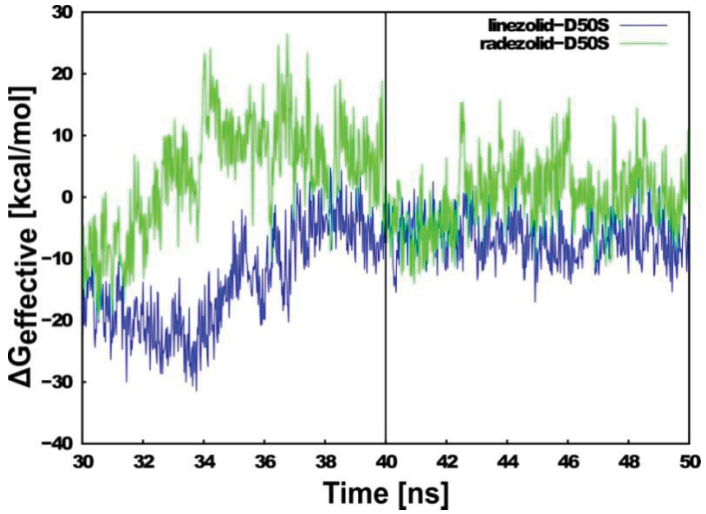

Figure 8: Time-series of effective binding energies. Effective binding energies calculated for 1000 snapshots extracted in 20 ps intervals from the last 20 ns of MD simulations of linezolid-D50S (blue) and radezolid-D50S complexes (green).

5.3.2 Structural analysis of the oxazolidinone-50S complexes

The crystal structures of linezolid-D50S and linezolid-H50S complexes both show that linezolid binds to the PTC with the acetamide end being located near the mouth of the ribosomal exit tunnel, the oxazolidinone ring making stacking interactions with U2504, and the morpholino ring approaching U2585 (Figure 4A, 5B&C and 6B) [24, 25]. Despite the similar overall binding modes, the crystal structures also reveal differences (Figure 5C) [24]. These include a rotation around the fluorophenyl ring relative to the oxazolidinone ring and different conformations of U2506 and U2585.

In order to detect whether such differences in the binding modes also lead to differences in specific interactions, we analyzed the network of hydrogen bonds of the antibiotics inside the binding pockets along the MD trajectories. In the linezolid-H50S crystal structure, the acetamide NH of linezolid forms a hydrogen bond with the phosphate group of G2505 [25] (Figure 5B). In contrast, the crystal structure of linezolid bound to D50S shows the involvement of the oxygen atom of the morpholino ring in a hydrogen bond interaction with N3 of U2585 [84] (Figure 5B). Figure 9 depicts the distances between these respective atoms (and those of the triazolyl-methylamino moiety in the case of radezolid) along the MD simulations of the H50S and D50S complexes with linezolid and radezolid, respectively. A distance < 3.2 Å between the acceptor and donor atoms is used as a criterion for the existence of a hydrogen bond [24, 150]. In the case of linezolid-H50S, the hydrogen bond between the acetamide NH of the ligand and the phosphate group of G2505 is disrupted throughout the

whole MD simulation (Figure 9A), whereas for radezolid-H50S the respective hydrogen bond is present ~90% of the time (Figure 9C). No hydrogen bond formation is observed for the morpholino and triazolyl-methylamino moieties, however, in both H50S simulations. In the case of D50S, no hydrogen bond is found involving the acetamide NH of linezolid or radezolid (Figure 9B, D), as is no hydrogen bond involving the morpholino moiety of linezolid. However, in the case of radezolid-D50S, hydrogen bond interactions of the triazolyl-methylamino moiety occur at ~34 ns and around 37 ns.

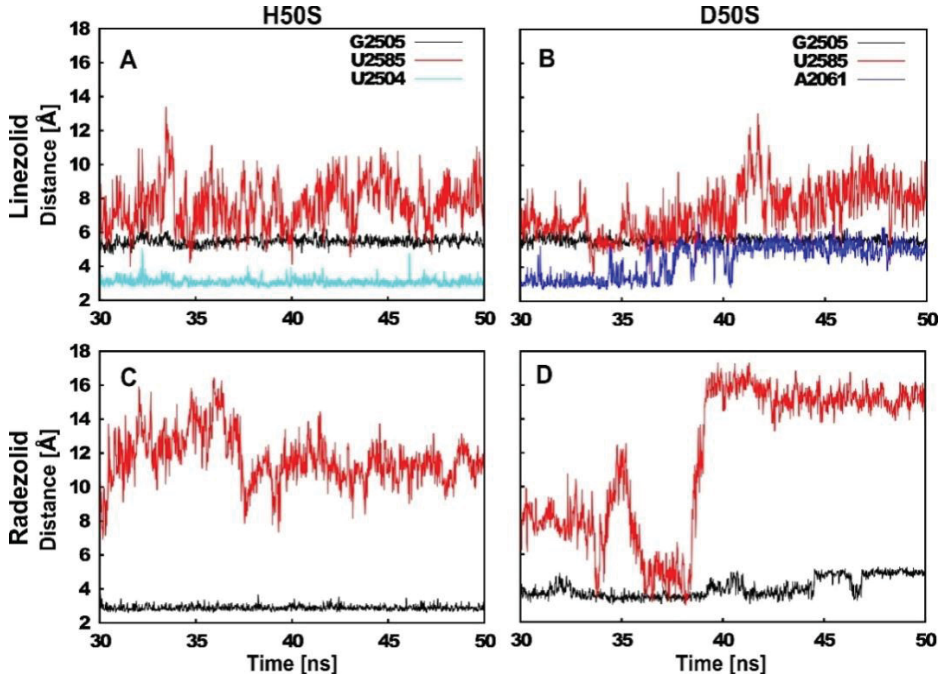

Figure 9: **Distances monitoring hydrogen bond**. Hydrogen bond formation for (A): linezolid-H50S, (B): linezolid-D50S, (C): radezolid-H50S, and (D): radezolid-D50S complex simulations. Hydrogen bonds were defined by acceptor donor atom distances of < 3.2 Å and acceptor H-donor angles of >120°. The distance between the ligands' acetamide NH group and the oxygens' of the phosphate group of G2505 is shown in black; the distance between the oxygen of the morpholino ring of linezolid and N3 of U2585 or any donor group of the triazolyl-methylamino moiety of radezolid and the carbonyl oxygens' of U2585 are shown in red. Only the smallest distance found is plotted in all cases. In addition, the distance between linezolid's acetamide NH group and O2' of U2504 is shown for H50S (A, cyan) as is the distance between linezolid's acetamide NH group and O6 of A2061 for D50S (B, blue).

Next, we analyzed interactions between the oxazolidinone ring and the nucleobase of U2504 as well as between the fluoro-phenyl ring and the nucleobases of A2451 and C2452, which form the so-called A-site cleft, by measuring the distances between the centers of the

respective rings (Figure 10). These ring/nucleobase pairs have been identified in the crystal structures of linezolid-D50S and linezolid-H50S as making important contacts [24, 25]. We used a ring center-to-ring center distance < 5.0 Å as a criterion to identify such contacts, which allows identifying T-shaped or parallel displaced ring configurations in addition to perfectly stacked ones [111]. The results show that linezolid engages in all such ring/nucleobase contacts (Figure 10A, B, D, E, F) except with A2451 when bound to H50S (Figure 9C). Radezolid forms all contacts (Figure 10A, B, C, D, E, and F). It is obvious, however, that – when established – contacts between the fluoro-phenyl ring and nucleobases of A2451 or C2452 of linezolid and radezolid have a longer distance in the D50S case (Figure 10D, F) than in the H50S case (Figure 10C, E). This suggests that weaker ring/nucleobase interactions are formed in the former case.

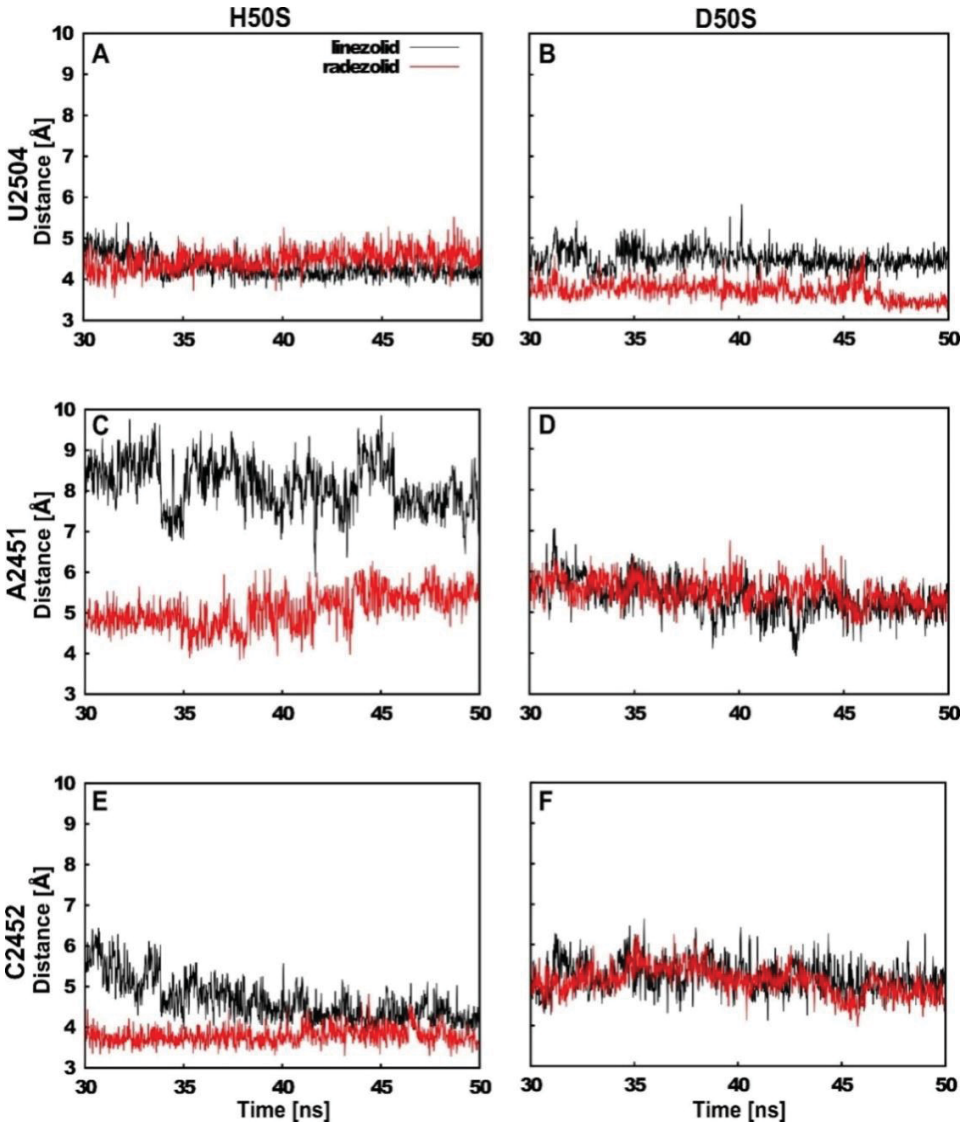

Figure 10: Distance plots representing aromatic stacking interactions: Distances between the centers of mass of the oxazolidinone ring and the nucleobase of U2504 (A, B) as well as between the centers of mass of the fluoro-phenyl ring and the nucleobases of A2451 (C, D) and C2452 (E, F), respectively. (A), (C), (E) Distances for oxazolidinone-H50S complex simulations. (B), (D), (F) Distances for oxazolidinone-D50S complex simulations. Black curves are for linezolid, red curves are for radezolid.

As the A-site cleft is wider [113] and more rigid [114] in *apo* D50S than in *apo* H50S, the dynamic behavior of the oxazolidinones inside the binding site could also differ between these eubacterial and archaeal ribosomes. We thus analyzed the RMSF (eq. 6) of the bound oxazolidinones (Figure 11).

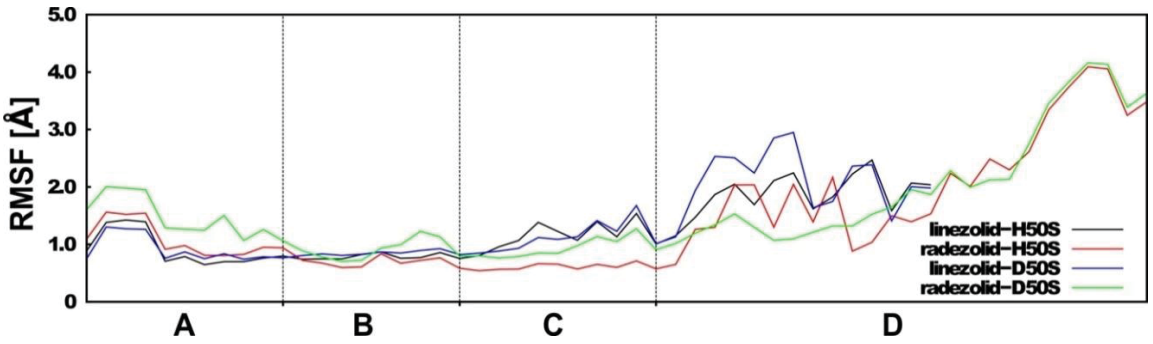

Figure 11: Root mean-square fluctuations of ligand atoms. RMSF of ligand atoms inside the binding site of the linezolid-H50S (black), radezolid-H50S (red), linezolid-D50S (blue), and radezolid-D50S (green) complexes for the last 20 ns of the MD simulations after root mean square fitting with respect to the phosphorous and C_α atoms of the first and second shell residues of the ligand binding sites. A, B, C, and D represent the acetamide, oxazolidinone, fluoro-phenyl, and morpholino moieties, respectively.

The RMSF values demonstrate that radezolid shows a higher mobility in the acetamide region than linezolid (in D50S and H50S), and that radezolid's mobility itself is higher when bound to D50S than when bound to H50S. The latter is also confirmed when analyzing structural variations of radezolid over the course of the MD trajectories (Figure 12). The difference of RMSF values in the case of linezolid is less pronounced in the acetamide region. In the region of the oxazolidinone core and the fluoro-phenyl ring, the mobility is generally low. In contrast, in the region of the morpholino and triazolyl-methylamino moieties, a generally high mobility is observed.

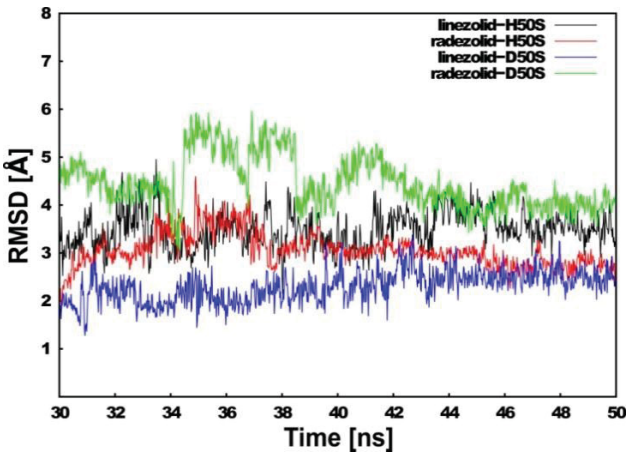

Figure 12: Root mean-square deviations of all atoms of the oxazolidinones along the MD trajectories. RMSD computed relative to the starting structure after root mean square fitting with respect to the phosphorous and C_α atoms of the first and second shell residues of the ligand binding sites. RMSD values for linezolid and radezolid in H50S are depicted in black and red, and for linezolid and radezolid in D50S in blue and green, respectively.

Finally, as the negatively charged ribonucleic acids need Mg^{2+} ions to maintain their structural stability [114], a correct description of the properties and behavior of the Mg^{2+} ions in the simulations is essential. The RMSF of the Mg^{2+} ions over the course of the MD simulations reveals that all Mg^{2+} ions remained fixed to their starting positions (data not shown). Thus, it seemed reasonable to consider these ions as part of the receptor in the subsequent effective binding energy calculations. For the D50S complexes the simulations also showed that one of the Mg^{2+} ions remains in close proximity to the bound oxazolidinones (Figure 13), as also observed in the crystal structure [24].

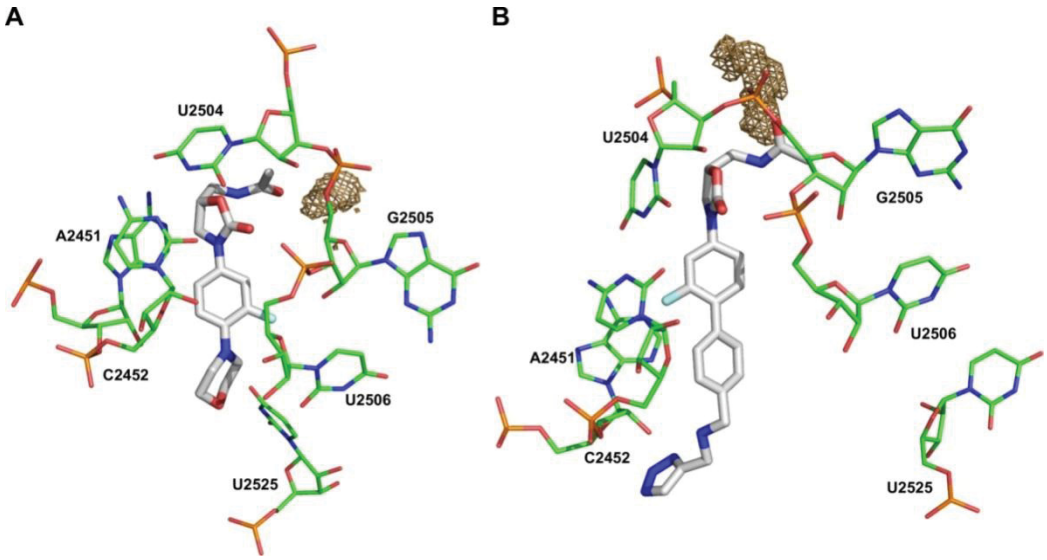

Figure 13: Isocontour meshes of the density of magnesium ions. Isocontours calculated in the vicinity of oxazolidinones as obtained from MD simulations of the (A): linezolid-D50S and (B): radezolid-D50S complex structures. A contouring level of 1 σ was used.

5.3.3 Energetic analysis of the oxazolidinone-50S complexes

In order to obtain insights into the energetic determinants of the selectivity of linezolid and radezolid with respect to D50S and H50S, effective binding energies ($\Delta G_{\text{effective}}$), i.e., the sum of gas-phase energies and solvation free energies, were computed by the MM-PBSA method using the single-trajectory approach (Table 1; eqs. 2, 3).

Table 1. Differences in the energy and entropy components for Linezolid and Radezolid bonding to H50S and D50S.[a]

Contribution[b]	Linezolid (D50S – H50S)		Radezolid (D50S – H50S)	
	Mean[c]	σ[d]	Mean[c]	σ[d]
$\Delta\Delta H_{elec}$	-4.52	0.04	-8.61	0.10
$\Delta\Delta H_{vdW}$	1.12	0.19	7.05	0.26
$\Delta\Delta H_{gas}$	-3.39	0.21	-1.56	0.30
$\Delta\Delta G_{PB}$	-3.64	0.20	21.82	0.25
$\Delta\Delta G_{nonpolar}$	0.07	0.09	0.48	0.09
ΔG_{eff}	-6.93	0.26	20.73	0.31
$TS_{R,\ T,\ V,\ ligand\ in\ complex}$	3.66	-[e]	3.15	-[e]
$TS_{V,\ receptor\ in\ complex}$	-4.46	-[e]	7.29	-[e]
$T\Delta\Delta S_{tot}$	-0.80	-[e]	10.44	-[e]
$\Delta\Delta G$	-6.16	-[e]	10.29	-[e]

[a] Gas phase and solvation free energy contributions were determined by the MM-PBSA approach, and entropy contributions were calculated by quasiharmonic analysis considering 500 snapshots from the last 10 ns of MD simulations of oxazolidinone-50S complexes; T = 300 K.
[b] H_{elec} : electrostatic energy; H_{vdW} : van der Waals energy; H_{gas} : gas-phase energy; G_{PB} : polar contribution to the solvation free energy; $G_{nonpolar}$: non-polar contribution to the solvation free energy; G_{eff} : effective energy; $S_{R,\ T,\ V,\ ligand\ in\ complex}$: translational, rotational, and vibrational entropy of the ligand in the complex, $S_{V,\ receptor\ in\ complex}$: vibrational entropy of the receptor in the complex.
[c] Average contributions in kcal mol^{-1}.
[d] Standard error of the mean in kcal mol^{-1}.
[e] No values available.

Although the alternative 3-trajectory MM-PBSA approach [75, 76, 78, 83, 84] has the advantage that changes in the receptor and ligand conformation upon complex formation are taken into account, the computationally less demanding single-trajectory approach has proven to be a good approximation in several ligand binding energy studies [84]. Here, $\Delta G_{effective}$ was computed by averaging over 500 snapshots extracted at 20 ps intervals from the last 10 ns of the MD simulations. The associated standard error in the mean determined according to ref. [84] is ~0.25 kcal mol^{-1} (Table 1). The computed $\Delta G_{effective}$ of linezolid (-6.73 kcal mol^{-1}; Table 2) and radezolid (-0.05 kcal mol^{-1}; Table 2) bound to D50S are (weakly) negative,

indicating that the sum of gas-phase and solvation free energies favor binding of these antibiotics. In contrast, for rivaroxaban, a considerably positive $\Delta G_{effective}$ was obtained (6.96 kcal mol^{-1}; Table 2), which is in line with experimental findings that rivaroxaban does not bind to the ribosome [119]. The analysis of the MD simulation of the rivaroxaban-D50S complex revealed that due to a displacement from its initial position rivaroxaban loses important interactions inside the binding site that are present in the linezolid-D50S complex crystal structure [24, 119].

Table 2. Energy and entropy contributions to ligand binding in D50S.[a]

Contribution[b]	Linezolid		Radezolid		Rivaroxaban	
	Mean[c]	σ[d]	Mean[c]	σ[d]	Mean[c]	σ[d]
ΔH_{elec}	-7.48	0.03	-12.54	0.08	-0.88	0.04
ΔH_{vdW}	- 39.43	0.14	-50.48	0.20	-41.94	0.20
ΔH_{gas}	-46.91	0.15	-63.03	0.23	-42.83	0.20
ΔG_{PB}	43.68	0.12	66.97	0.21	53.52	0.35
$\Delta G_{nonpolar}$	-3.53	0.01	-3.99	0.01	-3.74	0.01
ΔG_{eff}	-6.73	0.16	-0.05	0.25	6.96	0.49
$TS_{R, T, V, ligand\ in\ complex}$	73.89	-[e]	84.24	-[e]	-[e]	-[e]
$TS_{V, receptor\ in\ complex}$	253.06	-[e]	247.30	-[e]	-[e]	-[e]
$T\Delta S_{tot}$	326.95	-[e]	331.54	-[e]	-[e]	-[e]
ΔG	-333.71	-[e]	-331.59	-[e]	-[e]	-[e]

[a] Gas phase and solvation free energy contributions were determined by the MM-PBSA approach, and entropy contributions were calculated by quasiharmonic analysis considering 500 snapshots from the last 10 ns of MD simulations of oxazolidinone-50S complexes; T = 300 K.
[b] H_{elec} : electrostatic energy; H_{vdW} : van der Waals energy; H_{gas} : gas-phase energy; G_{PB} : polar contribution to the solvation free energy; $G_{nonpolar}$: non-polar contribution to the solvation free energy; G_{eff} : effective energy; $S_{R, T, V, ligand\ in\ complex}$: translational, rotational, and vibrational entropy of the ligand in the complex, $S_{V, receptor\ in\ complex}$: vibrational entropy of the receptor in the complex.
[c] Average contributions in kcal mol^{-1}.
[d] Standard error of the mean in kcal mol^{-1}.
[e] No values available.

The difference in the effective binding energy ($\Delta\Delta G_{effective}$) for linezolid bound to D50S *versus* H50S is -6.93 ± 0.26 kcal mol^{-1} (Table 1), thus demonstrating that binding of the antibiotic to D50S is favored. At T = 300 K, this difference is equivalent to a 10^5-fold larger association constant for linezolid-D50S than for linezolid-H50S. This result agrees well with experiment according to which a 10^3-fold higher concentration of the antibiotic is required for a successful co-crystallization in H50S compared to D50S [118]. The decomposition of $\Delta\Delta G_{effective}$ with respect to the energy terms contributing to it reveals that the electrostatic ($\Delta\Delta H_{elec}$ = -4.52 kcal mol^{-1}) and polar solvation free energy ($\Delta\Delta G_{PB}$ = -3.64 kcal mol^{-1}) contributions favor binding to D50S over H50S, whereas van der Waals interactions ($\Delta\Delta H_{vdW}$ = 1.12 kcal mol^{-1}) disfavor it. In contrast, for radezolid, $\Delta\Delta G_{effective}$ = 20.73

kcal mol^{-1} was computed (Table 1), which would suggest that, based only on the sum of gas-phase and solvation free energies, binding to H50S is favored over D50S. This result is at variance with experiment: While to the best of our knowledge no specific experimental data of radezolid binding to D50S or H50S has been reported, it has been stated that radezolid is > 100-fold selective for bacterial ribosomes over those of rabbit reticulocyte [132]. Regarding the decomposition of $\Delta\Delta G_{effective}$ with respect to the energy terms contributing to it, we find that the polar solvation free energy ($\Delta\Delta G_{PB}$ = 21.82 kcal mol^{-1}) highly favors binding to H50S compared to D50S. The van der Waals interactions also considerably contribute to the more favorable effective binding energy found for H50S ($\Delta\Delta H_{vdW}$ = 7.05 kcal mol^{-1}), whereas the electrostatic energy ($\Delta\Delta H_{elec}$ = -8.61 kcal mol^{-1}), as in the case of linezolid, shows the opposite trend, i.e., is more favorable in the D50S case.

While the continuum solvation model provides estimates of the free energy of solvation and includes entropic contributions of the solvent, changes in the entropy of the solute molecules upon binding have been neglected so far. However, such changes can significantly influence the binding affinity [120, 121]. Hence, we estimated differences in the changes in the configurational entropy ($T\Delta\Delta S$ at T = 300 K) upon binding of linezolid (or radezolid) to D50S and H50S based on motions of the ligands and the nucleotides forming the first shell of the binding site by quasiharmonic analysis (QHA) (Table 1; Tables 2 and 3; eqs. 7-10; Figure 14). The librational/vibrational entropy of the ligand inside the binding site ($TS_{R,T,V,\ ligand\ in\ complex}$) was found to be higher in the D50S complex than in the H50S complex by 3-4 kcal mol^{-1} for both ligands (Table 1). In contrast, ligand binding has converse effects on the vibrational entropy of the first shell nucleotides ($TS_{V,\ receptor\ in\ complex}$): linezolid (radezolid) binding leads to ~4 kcal mol^{-1} lower (~7 kcal mol^{-1} higher) values in the case of D50S than H50S. Taken together, the difference in the changes in the configurational entropy is close to zero for linezolid binding to D50S *versus* H50S; in contrast, the changes in the configurational entropy favor radezolid binding to D50S over H50S by ~10 kcal mol^{-1} (Table 1).

Table 3. Entropy contributions to ligand binding in D50S and H50S.[a]

Contribution[b]	Linezolid		Radezolid	
	D50S[c]	H50S[c]	D50S[c]	H50S[c]
$TS_{R,\ T,\ V,\ \text{ligand in complex}}$	73.90 (74.65)	70.23 (74.70)	84.25 (91.61)	81.09 (90.07)
$TS_{V,\ \text{receptor in complex}}$	253.06 (274.04)	257.52 (276.68)	247.30 (275.66)	240.01 (260.48)
$T\Delta S_{tot}$	326.96 (348.69)	327.75 (351.38)	331.55 (367.27)	321.10(350.55)
$T\Delta\Delta S_{tot}$[d]	-0.80 (-2.69)		10.44 (46.17)	

[a] Entropy contributions were calculated by quasiharmonic analysis considering 500 (1000) snapshots from the last 10 (20) ns of MD simulations of oxazolidinone-50S complexes; $T = 300$ K.
[b] $S_{R,\ T,\ V,\ \text{ligand in complex}}$: translational, rotational, and vibrational entropy of the ligand in the complex, $S_{V,\ \text{receptor in complex}}$: vibrational entropy of the receptor in the complex.
[c] Average contributions in kcal mol^{-1}.
[d] Difference in the $T\Delta S_{tot}$ contributions between D50S and H50S in kcal mol^{-1}.

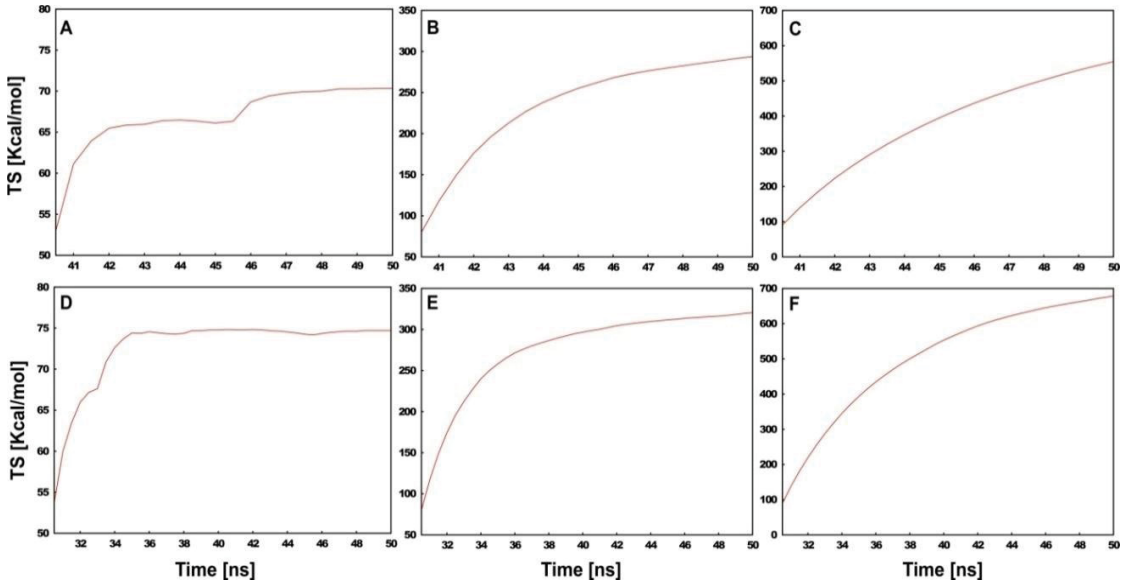

Figure 14: Convergence of the absolute entropy. Entropy, i.e., *TS* at $T = 300$ K of the linezolid-H50S complex computed by quasiharmonic analysis for the last 10 ns (A, B, and C) and 20 ns (D, E, and F). (A and D): Only the ligand was considered for the entropy calculations after root mean-square (RMS) fitting with respect to the first shell of residues of the ligand binding site; (B and E): the ligand plus the first shell of residues were considered after RMS fitting with respect to the second shell of residues of the ligand binding site; (C and F): the ligand plus the first two shells of residues were considered after RMS fitting with respect to the third shell of residues of the ligand binding site. The drifts for the last 1 ns of the interval 40 - 50 ns are 0.05 kcal mol^{-1} (A), 5.52 kcal mol^{-1} (B), and 24.28 kcal mol^{-1} (C) whereas the drifts for the last 1 ns of the interval 30 - 50 ns are 0.003 kcal mol^{-1} (D), 2.26 kcal mol^{-1} (E), and 7.51 kcal mol^{-1} (F), respectively.

To gain insights into the origin of the selectivity of oxazolidinone binding on an atomic level, we decomposed the effective binding energy in terms of contributions from structural subunits of D50S and H50S. Such structural decompositions have been successfully applied before in the context of protein-protein interactions [69, 122] and protein-peptide interactions [150] by us. The standard error in the mean $\Delta G_{effective}$ value for one residue is assumed to be of the same order of magnitude than the one for the overall effective binding energy (~0.25 kcal mol^{-1}). Note that the mean $\Delta G_{effective}$ values do not include contributions due to changes in the configurational entropy of the receptor residues upon ligand binding. Such contributions could be of significant influence, however, according to the $TS_{V,\text{ receptor in complex}}$ computations above. As expected, the structural decomposition reveals that first shell nucleotides contribute most to the effective binding energy (between -10.03 and -13.06 kcal mol^{-1}) (Figure 15; Tables 4, 5). Still, second shell nucleotides show contributions of up to 1.76 kcal mol^{-1}, i.e., 15%. As a single-trajectory alternative is used for the computations of effective binding energies, long-range electrostatic influences are most likely responsible for the contribution by the second shell nucleotides [124-131].

Table 4. Residue-wise effective binding energy contributions for D50S and H50S.[a]

	D50S		H50S	
Residue no.[b]	**Linezolid**	**Radezolid**	**Linezolid**	**Radezolid**
A2451[c]	-3.61	-4.16	-0.12	-3.21
C2452[c]	-4.43	-2.21	-5.54	-3.44
U2504[c]	-2.52	-3.54	-2.41	-2.22
G2505[c]	-0.57	-0.38	-0.19	-1.57
U2506[c]	-1.60	-0.18	-1.79	-2.09
U2585[c]	-0.33	-0.24	0.02	0.15
$\Sigma_{\text{first shell}}$	**-13.06**	**-10.71**	**-10.03**	**-12.38**
C(A)2055[d,e]	-0.40	-0.16	0.29	0.40
G2447[d]	0.26	0.21	0.17	0.23
A2453[d]	-0.18	-0.03	0.23	0.09
U2500[d]	-0.05	-0.06	0.11	0.26
A(U)2572[d,e]	0.15	0.06	0.80	0.78
$\Sigma_{\text{second shell}}$	**-0.22**	**0.02**	**1.60**	**1.76**

[a] Mean effective binding energies for first and second shell residues of the ligand binding site were determined by the MM-PBSA approach considering 500 snapshots from the last 10 ns of MD simulations of oxazolidinone-50S complexes. In kcal mol^{-1}.
[b] Residue number according to *E. coli* numbering.
[c] Residues of the first shell of the ligand binding site.
[d] Residues of the second shell of the ligand binding site.
[e] Nucleotide outside the brackets: D50S; nucleotide inside the brackets: H50S.

Table 5. Difference in effective binding energy contributions between D50S and H50S on a per-residue level.[a]

Residue no.[b]	Linezolid (D50S – H50S)	Radezolid (D50S – H50S)
A2451[c]	-3.49	-0.95
C2452[c]	1.11	1.23
U2504[c]	-0.11	-1.32
G2505[c]	-0.38	1.19
U2506[c]	0.19	1.91
U2585[c]	-0.35	-0.39
$\Sigma_{\text{first shell}}$	**-3.03**	**1.67**
C(A)2055[d,e]	-0.69	-0.56
G2447[d]	0.09	-0.02
A2453[d]	-0.41	-0.12
U2500[d]	-0.16	-0.32
A(U)2572[d,e]	-0.65	-0.72
$\Sigma_{\text{second shell}}$	**-1.82**	**-1.74**

[a] Difference between mean effective binding energies for D50S and H50S. Effective binding energies for first and second shell residues of the ligand binding site were computed by the MM-PBSA approach considering 500 snapshots from the last 10 ns of MD simulations of oxazolidinone-50S complexes. In kcal mol^{-1}.
[b] Residue number according to *E. coli* numbering.
[c] Residues of the first shell of the ligand binding site.
[d] Residues of the second shell of the ligand binding site.
[e] Nucleotide outside the brackets: D50S; nucleotide inside the brackets: H50S

Regarding linezolid, the most pronounced difference is observed for A2451 in the first shell (Table 5): this nucleotide contributes strongly (-3.61 kcal mol^{-1}) to the binding of the antibiotic in D50S, but shows an almost neutral influence (-0.12 kcal mol^{-1}) in the case of H50S (Table 4). The difference in the contribution of the highly favorable C2452 – ligand interaction is not as pronounced (-4.43 kcal mol^{-1} in D50S *versus* -5.54 kcal mol^{-1} in H50S), but amounts up to ~1 kcal mol^{-1} in favor of H50S. Notably, also small differences in the effective binding energies of second shell nucleotides are observed: nucleotides 2055 (2572) contribute favorably (neutrally) to binding in the case of D50S (-0.40 kcal mol^{-1} (0.15 kcal mol^{-1})), whereas they disfavor binding to H50S (0.29 kcal mol^{-1} (0.80 kcal mol^{-1})).

As to radezolid, again A2451 and C2452 show significant and opposing differences in their contributions to the effective binding energy (Table 5): Both nucleotides contribute highly favorably to binding in D50S and H50S, but A2451 shows a higher effective binding energy in D50S (-4.16 kcal mol^{-1}) than in H50S (-3.21 kcal mol^{-1}), whereas C2452 exhibits a lower effective binding energy in D50S (-2.21 kcal mol^{-1}) than in H50S (-3.44 kcal mol^{-1}) (Table 4). For U2504, which shows the second largest difference, the same trend as for A2451 is observed: this nucleotide's contribution is more favorable in the D50S case (-3.54 kcal mol^{-1}) than in the H50S case (-2.22 kcal mol^{-1}). Finally, G2505 and U2506 contribute to the effective binding energy by -1.57 and -2.09 kcal mol^{-1} in H50S, whereas their contributions remain almost neutral in the case of D50S. As to the contributions from second shell nucleotides, again differences are found between D50S and H50S: nucleotides 2055 and 2572 both disfavor binding to H50S, whereas their contribution to binding in D50S is neutral (Table 4).

In summary, the energetic analyses of the oxazolidione-50S complexes reveal significant differences in the effective binding energies, also in terms of structural contributions, and configurational entropies with respect to the binding of linezolid or radezolid to D50S and H50S.

5.3.4 Conclusions and implications for drug design

The highly conserved functional sites in the ribosome make the task of developing selective antibiotics challenging. In the present study, we aimed at identifying on an atomic level the determinants of selectivity of linezolid and radezolid, binding to the eubacterial D50S and the archaeal H50S subunits, by means of MD simulations and free energy computations. Although structure-activity relationships of oxazolidinones have been

extensively reported [126-132], none of these studies has considered aspects of structure, energetics, and dynamics to selectivity simultaneously. Preliminary results addressing this question have been reported by Franceschi *et al.* as a conference contribution using MCPRO [133] for a residue-by-residue analysis of interaction energies [134].

From a global point of view, it is remarkable that the MM-PBSA analyses including estimates of changes in the configurational entropy agree well with results from experiment on the selectivity of linezolid. These computations furthermore reveal that linezolid's selectivity towards D50S over H50S is favored by the effective energy whereas there is only a vanishing contribution by the configurational entropy (Table 1). A converse picture emerges for the global selectivity determinants of radezolid: the effective energy strongly favors binding to H50S over D50S now, but differences in the changes of the configurational entropy oppose this effect (Table 1). Although in sum, binding of radezolid to H50S remains favorable, note that the contributions of the configurational entropy only consider effects of the first shell of binding site nucleotides due to the lack of convergence when including second (and, likely, higher) shell nucleotides (see Materials and Methods). If one assumes that the observed trend for the configurational entropy will become even more pronounced once additional nucleotides are included in the estimation, radezolid's binding to D50S will eventually become favorable over binding to H50S, in agreement with experiment.

These observations on the energetics on a global level are consistent with structural and mobility analyses of oxazolidinone-50S complexes from the MD trajectories, and structural analyses of *apo* and *holo* 50S crystal structures. As such, a wider A-site cleft in the case of *apo* D50S compared to *apo* H50S [112] may contribute to the observed higher mobility of radezolid particularly in the acetamide region (Figure 10) and, consequently, to the higher vibrational/librational entropy (Table 1) when bound to D50S compared to H50S. In turn, rigidity analyses on 50S subunits revealed that the glycosidic bond of A2451 is flexible in H50S but rigid in D50S [113]. Accordingly, binding of the antibiotics can rigidify this crevice only in the case of H50S, even more so if strong aromatic interactions are formed between the fluoro-phenyl ring and the cleft's nucleobases. The latter is particularly observed for radezolid binding to H50S (Table 1; Figure 15; Table 4). Thus, it does not come as a surprise that vibrational entropy contributions of first shell nucleotides of the binding sites favor radezolid binding to D50S over H50S (Table 1).

The structural analysis of the MD trajectories reveals that linezolid neither forms strong hydrogen bonds with its acetamide group nor with its morpholino moiety, neither when it is bound to D50S nor to H50S. Regarding the acetamide group, this observation agrees with observations from the linezolid-D50S crystal structure [24] but disagrees with what has been found for the linezolid-H50S structure [25]. In the latter case, a hydrogen bond to the phosphate group of G2505 has been described. Regarding the morpholino moiety, only a relatively weak hydrogen bond has been found in the linezolid-D50S crystal structure [24, 25], which stabilizes an otherwise highly flexible U2585. Thus, the observed breaking of this hydrogen bond during the MD simulations at 300 K is not unexpected. Interactions of linezolid's fluoro-phenyl ring are observed to C2452 in both the D50S and H50S simulations (Figure 10E,F), in agreement with crystal structure analyses [24, 25], with them being tighter in the H50S case. In contrast, A2451 forms additional interactions with the fluoro-phenyl ring only in D50S, which explains to a large extent why the effective binding energy of linezolid is more favorable in the D50S case than in the H50S case (Table 1). Radezolid forms a strong hydrogen bond with its acetamide group to G2505 in H50S only. Furthermore, although it forms tighter interactions with its oxazolidinone ring with U2504 in D50S, it does so too between its fluoro-phenyl ring and A2451 as well as C2452 in H50S. Taken together, these differences in the interactions can explain to a large extent why the effective binding energy of radezolid is computed to be more favorable in the H50S case than in the D50S case (Table 1).

The results from the structural decomposition of the effective binding energies confirm essentially these analyses of the influence of interactions of first shell nucleotides of the binding sites on oxazolidinone selectivity. As an advantage, the structural decomposition provides a spatially resolved picture of the binding energetics (Figure 15), making the identification of selectivity "hot spots" or "cold spots" easier. This is particularly helpful for investigating influences of the second (and higher) shell residues, where often a direct link to interactions with the ligand is not obvious. In the present case, the structural decomposition reveals the most pronounced influence of second shell residues on the selectivity of oxazolidinones for nucleotides 2055 and 2572 (Figure 15; Table 5). This finding is in line with previous reports according to which both nucleotides are involved in differently restraining the conformational space of U2504 in eubacteria *versus* archaea/eucaryotes and, hence, the selectivity of antibiotics binding to the A-site cleft [135, 142]: In general, in eubacteria, U2504 is sterically fostered by C2055 and A2572 to adopt a conformation that

favors interactions with antibiotics; in contrast, in archaea/eucaryotes U2504 adopts a conformation unsuitable for interactions with antibiotics due to A2055 and U2572. Oxazolidinone binding to the A-site cleft is now peculiar in that U2504 *in* H50S adopts a *eubacterial* conformation. As a consequence, the induced fit should incur a cost in free energy. In line with this, the structural decomposition identifies U2504 to disfavor oxazolidinone binding to H50S over D50S. Notably, the conformational strain is also relayed to nucleotides 2055 and 2572 as these disfavor oxazolidinone binding to H50S over D50S, too (Figure 15; Table 5). This finding provides direct evidence for the energetic involvement of second shell residues in oxazolidinone selectivity.

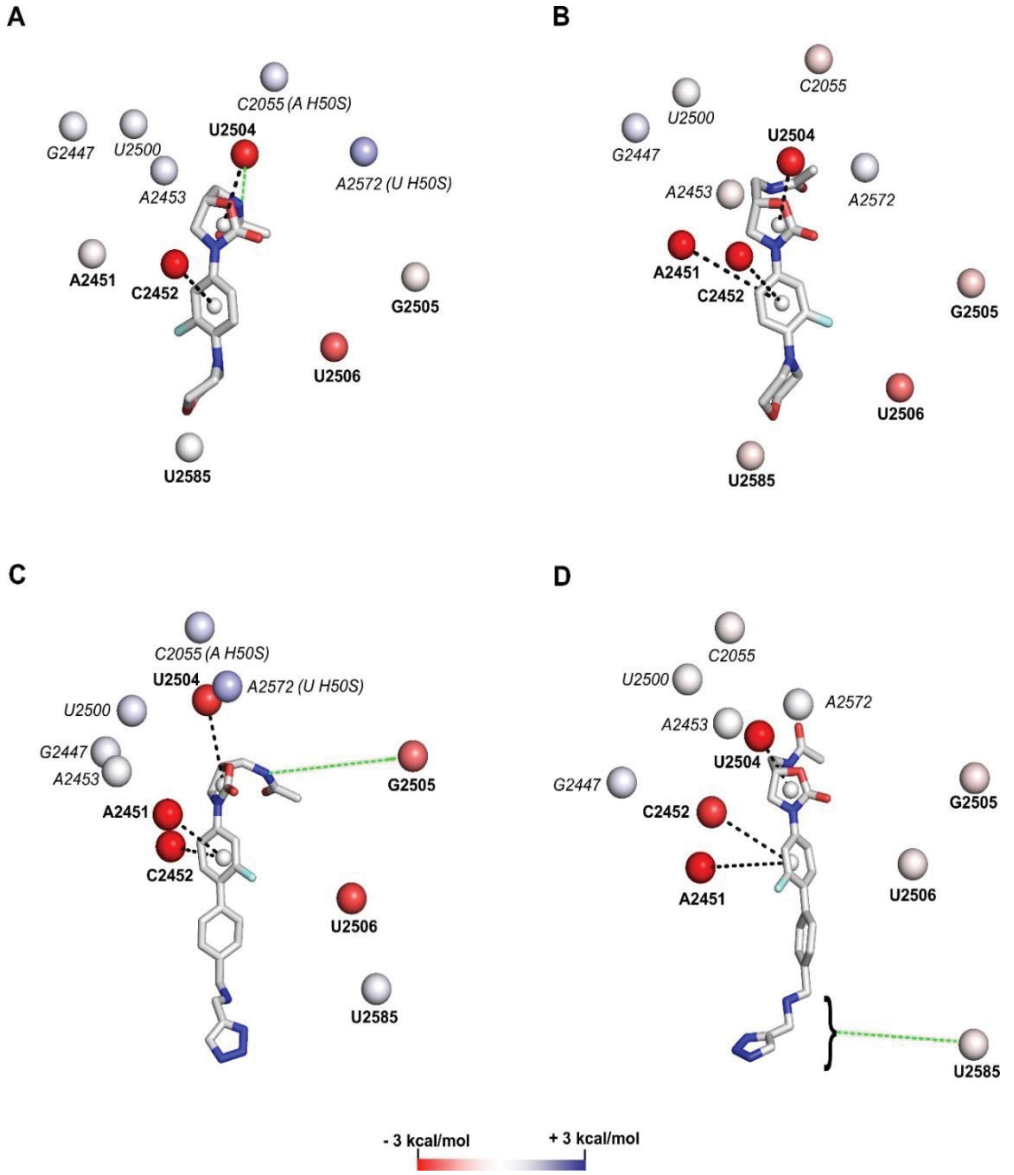

Figure 15: Per-residue contributions to the effective binding energy. Structural decomposition at per-residue level calculated via MM-PBSA using ensembles from MD simulations of (A): linezolid-H50S, (B): linezolid-D50S, (C): radezolid-H50S, and (D): radezolid-D50S complex structures. Each sphere represents the center of mass of the nucleobase of the respective nucleotide; nucleotides of the first shell are labeled with straight letters, those of the second shell in italics. Ligands are shown as sticks. The per-residue contributions are mapped using a color code with a linear scale (red: ≤ -3 kcal/mol; white: 0 kcal/mol; blue: ≥ +3 kcal/mol). Hydrogen bonds observed during the MD simulations between oxazolidinones and nucleotides (Figure 9) are indicated by dotted green lines; ring/nucleobase contacts observed during the MD simulations (Figure 10) are shown as dotted black lines.

For the following Chapter, the text and figures have been taken and modified from the publication:

"Simone Fulle, **Jagmohan S. Saini,** Nadine Homeyer, Holger Gohlke, "Complex long-distance effects of mutations that confer linezolid resistance in the large ribosomal subunit. **Nucleic Acids Res., 2015,** 7731–7743"

6. Complex long-distance effects of mutations that confer linezolid resistance development in the ribosomal subunit

6.1 Introduction

The ever increasing emergence of multidrug-resistant bacteria will make current antibiotics virtually ineffective in the future. This stresses the need to identify novel classes of antibiotics [2, 136]. Yet, only compounds of five new classes of antibiotics have been approved by the FDA in the past 30 years, among them antibiotics of the oxazolidinone class [137]. Oxazolidinone antibiotics display bacteriostatic activity against many important pathogens, including methicillin-resistant *Staphylococcus aureus* (MRSA) and vancomycin-resistant *Enterococcus faecium* (VREF) [138]. So far, linezolid (Figure 4B) has been the first line antibiotic for therapeutic use [22, 137-139] but enhanced oxazolidinones are currently undergoing clinical evaluation [89]. The co-crystal structures of linezolid with the large ribosomal subunits of the eubacterium D50Sand the archaeon (H50S) [24, 25]demonstrate that the antibiotic exerts its action by binding to the A-site of the highly conserved peptidyl transferase center (PTC) [24, 25] (Figure 4A) and preventing the proper placement of the incoming aminoacyl-tRNA. As a consequence, protein synthesis is inhibited.

Not long after the commercial release of linezolid, strains of MRSA and VREF appeared in the clinics that are resistant against linezolid [24, 139]. Also considering nucleotides conferring linezolid resistance in other bacterial strains (Table 6), it was revealed that many of these are clustered in a distinct region of the PTC (called the PTC "rear wall") and are located in a distance of 6-12 Å from the affected antibiotic [23, 29]. An explanation for this observation is that mutations of the highly conserved linezolid binding pocket are likely unfavorable for ribosome function, [29] while nucleotide alterations in more remote regions of lower sequence conservation bear a lower potential to affect ribosome function lethally.

Table 6: Nucleotides mediating linezolid resistance (Table adapted from ref. [29]).

E. coli[a,b]	*D. radiodurans*[c]	*H. marismortui*[c]
2032	2015	2073
2062	2045	2103
2447	2426	2482
2452	2431	2487
2453	2432	2488
2499	2478	2534
2500	2479	2535
2503	2482	2538
2504	2483	2539
2505	2484	2540
2576	2555	2611

[a]*E. coli* numbering
[b] From ref. [119]
[c] Taken from http://www.riboworld.com/nuctrans/

Oxazolidinones bind and inhibit both bacterial and archaeal ribosomes [24, 25] but do not interact with human cytoplasmic ribosomes [24]. Out of 10 mutations known to give rise to linezolid resistance in bacteria and archaea, the nucleotides corresponding to two of these mutations are already present in the 28S rRNA of *Homo sapiens* at positions 2032 and 2499 [24, 142]. Mutations at these positions also mediate resistance against other antibiotics [142-146]. Both mutation sites, which are either highly or absolutely conserved in eubacteria (position G2032: 94%; C2499: 100%), [29] are more than 10 Å away from linezolid bound at the PTC and constitute third shell nucleotides with respect to the linezolid binding pocket. Thus, mutation effects must propagate to nucleotides forming direct interactions with the drug (first shell nucleotides) via second shell nucleotides (Figure 16B, C) [29]. Experimental results indicate that single mutations at that distance are not sufficient to confer resistance [29] and that the development of antibiotics resistance due to remote nucleotides requires the additive or even synergistic effect of several mutations [23, 146]. Accordingly, a double mutation at these sequence positions (G2032A-C2499A) observed in *Mycobacterium smegmatis* showed remarkable synergistic effects on linezolid resistance relative to the effects of the corresponding single mutations [29]. Overall, this makes these sites ideal

prototypes for investigating how mutations can confer long-distance effects on antibiotics binding.

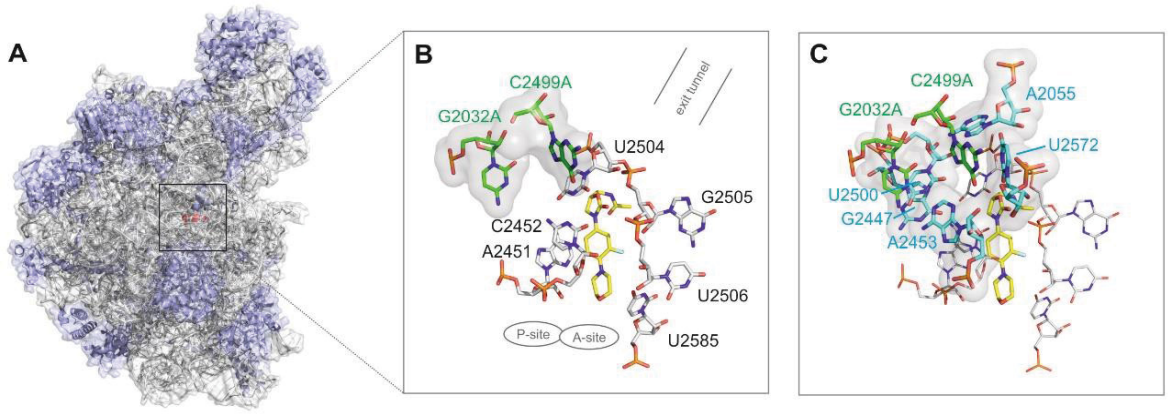

Figure 16: Binding region of linezolid in H50S. (A): Structure of the large ribosomal subunit (PDB code 3CPW [119]). The ribosomal RNA is shown in grey and the protein chains are shown in blue; the binding position of linezolid (red) is depicted by a black square. (B and C): Binding mode of linezolid in the PTC of H50S. Nucleotides forming the 1st (black labels) and 2nd shell (light blue labels) of the binding site are depicted in (B and C), respectively; the two mutation sites (G2032A and C2499A) are highlighted in green. The locations of the A- and P-site and of the exit tunnel are indicated.

To gain insights at an atomistic level into how remote mutations exert long-distance effects that lead to resistance to oxazolidinones, we extended a previous study on the determinants of the species selectivity of oxazolidinone antibiotics, which had considered the wild type structure of H50S (linezolid-H50S$_{wt}$), [119] by performing molecular dynamics (MD) simulations in combination with molecular mechanics Poisson-Boltzmann surface area (MM-PBSA) free energy calculations of linezolid bound to the double mutant G2032A-C2499A of H50S (linezolid-H50S$_{mut}$). Furthermore, MD simulations of novel oxazolidinone antibiotics, radezolid that show activity against linezolid-resistant strains [147] were performed. To the best of our knowledge, this is the first study that investigates resistance to oxazolidinone binding to the 50S ribosomal subunit by simultaneously considering structural, energetic, and dynamic aspects. These determinants are consistent in describing effects of a complex but balanced reorganization in the network of inter-nucleotide interactions that percolates from the mutation sites to the PTC. Cross-talk identified between the two main routes of information transfer can explain the experimentally observed synergy of the double

mutation. These findings go beyond current knowledge on the structural basis for oxazolidinone resistance.

6.2 Material and Methods

6.2.1 MD simulations of the oxazolidinone-50S systems

Please refer to section 5.2.1 for details regarding (A) ligands parameterization, (B) system building, and (C) setting MD simulations.

To investigate the influence of the G2032A-C2499A double mutation on linezolid binding, a model structure (linezolid-H50S$_{mut}$) was generated from the linezolid-H50S crystal [25] complex structure by mutating G2032 and C2499 to adenine, respectively.

Please refer to section 5.2.2 for details regarding structural analysis of MD trajectories.

For the calculation of the occupancy of hydrogen bonds, hydrogen bonds were defined by acceptor…donor atom distances of < 3.2 Å and acceptor…H-donor angles of > 120°. For the analysis of water-mediated hydrogen bonds, the 'cpptraj' module of AmberTools13 was used with the same geometric criteria as in the case of "normal" hydrogen bonds.

6.2.2 Calculation of effective binding energies

Please refer to section 5.2.3 for details regarding calculation of effective binding energies.

A sequential-focusing multigrid procedure was applied where the 50S ribosomal complexes were initially encapsulated in a coarser cubic grid with dimensions of 292 × 347 × 412 Å^3; then, a finer, cubic grid with dimensions of 25 × 25 × 25 Å^3 focused on the ligand region was applied. The electrostatic potential was obtained at a resolution of 0.19 Å. The continuum solvent dielectric constant was set to 80, and the solute dielectric constant was set to 11. The value of 11 for the solute dielectric constant has been found to be optimal in preliminary tests on oxazolidinone-H50S complexes. The dielectric boundary was defined by a probe sphere with a radius of 1.4 Å. For all PB calculations, the PARSE parameter set was applied (radius of H= 1.0 Å, C = 1.7 Å, N= 1.5 Å, O = 1.4 Å, P = 2.0 Å) [142]. A dielectric radius of 1.50 Å was assigned to both Zn^{2+} and Mg^{2+} ions [107]. The calculations were performed at 150 mM ionic strength with an ion exclusion radius of 2 Å [107].

6.3 Results and discussion

6.3.1 Overall structural stability of the linezolid-H50S complexes

All-atom explicit solvent MD simulations of 50 ns length each were performed for linezolid-H50S$_{wt}$ (described in ref. [119]) and linezolid-H50S$_{mut}$, which constitute systems of the size of ~8.5×10^5 atoms. For investigating structural deviations along the trajectories, the root-mean square deviation (RMSD) of all and only 'core' residues were computed with respect to the starting structure for both the complexes (Figure 17A) (eq. 5). Here the term 'residue' is used for both nucleotides and amino acids. Likewise, the RMSD of nucleotides forming the ligand binding site (1st and 2nd shell nucleotides of the PTC) (Figure 17B) and the RMSD of linezolid (Figure 17C) were computed after superpositioning the 'core residues'. Comparing these values with those for linezolid-H50S$_{wt}$ [119] shows that the structures of the large ribosomal subunits remain stable over the course of the trajectories, with RMSD values of the 'core' and binding site residues reaching plateaus of ~2 Å. A major difference between both systems occurs with respect to the stability of the ligand binding mode: while the ligand in linezolid-H50S$_{wt}$ shows RMSD values of ~3 Å after 10 ns of MD simulations, which then remain stable (Figure 17C), the RMSD of the ligand in linezolid-H50S$_{mut}$ jumps to ~6 Å after that time and then increases to values of up to 14 Å (Figure 17C). Visual inspection of the linezolid-H50S$_{mut}$ trajectory reveals that linezolid moves from the starting position (Figure 16B, C) further towards the A- and P-sites in the course of the simulation (Figure 16B).

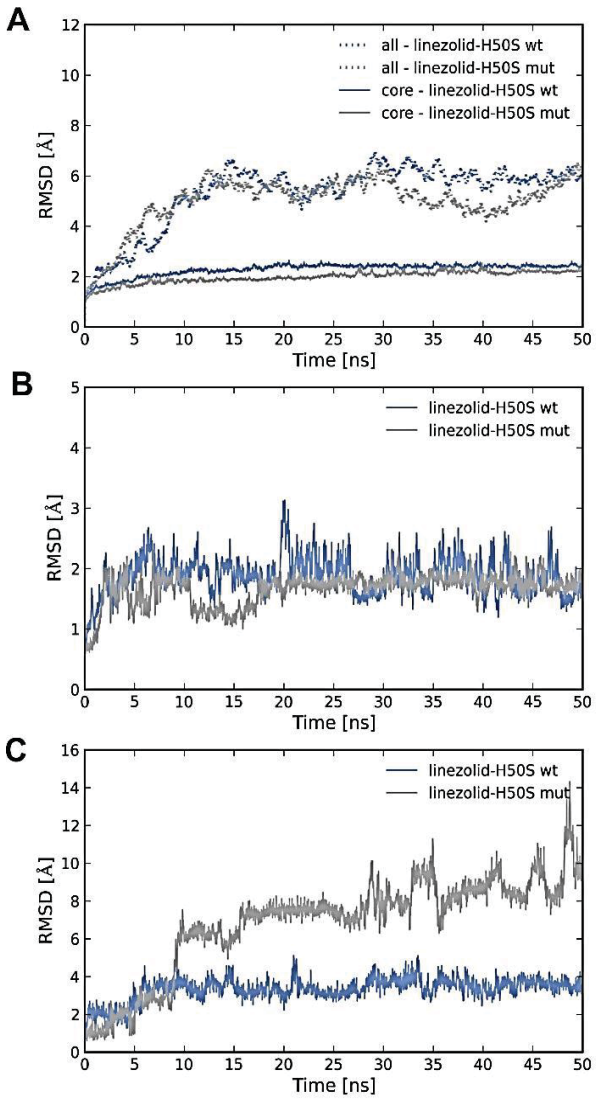

Figure 17: Root mean-square deviations of all-atoms, core-atoms, and the ligand with respect to the starting structure. (A): RMSD of $C_\alpha$and phosphorous atoms of all residues (dashed lines) and the 'core residues' (solid lines) along the MD trajectories of linezolid-H50S$_{wt}$ (blue) and linezolid-H50S$_{mut}$ (grey) complex structures. The 'core residues' were defined as those residues with the 90% lowest RMSF of the C_α and phosphorous atoms. (B): RMSD of nucleotides forming the ligand binding site (1st and 2nd shell) along the MD trajectories of linezolid-H50S$_{wt}$ (blue) and linezolid-H50S$_{mut}$ (grey) complex structures. (C): RMSD of linezolid along the MD trajectories of linezolid-H50S$_{wt}$ (blue) and linezolid-H50S$_{mut}$ (grey) complex structures after fitting to the $C_\alpha$and phosphorous atoms of the 'core residues'.

6.3.2 Effect of G2032A-C2499A mutations on structure and interaction network

The movement of linezolid in the H50S$_{mut}$ structure is accompanied by conformational changes of nucleobases forming the first shell, especially U2504, G2505, U2506, A2451, and C2452 (Figure 18B) in comparison to the starting structure (Figure 16B). Most pronounced, the nucleobase of U2504 in H50S$_{mut}$ moves to where the oxazolidinone core of linezolid was

in the starting structure; likewise, G2505 moves to the starting location of the acetamide moiety. In contrast, only minor structural changes of both the ligand binding mode and the surrounding nucleobases have been observed for linezolid bound to $H50S_{wt}$ (Figure 16B, C and 18A) [119].

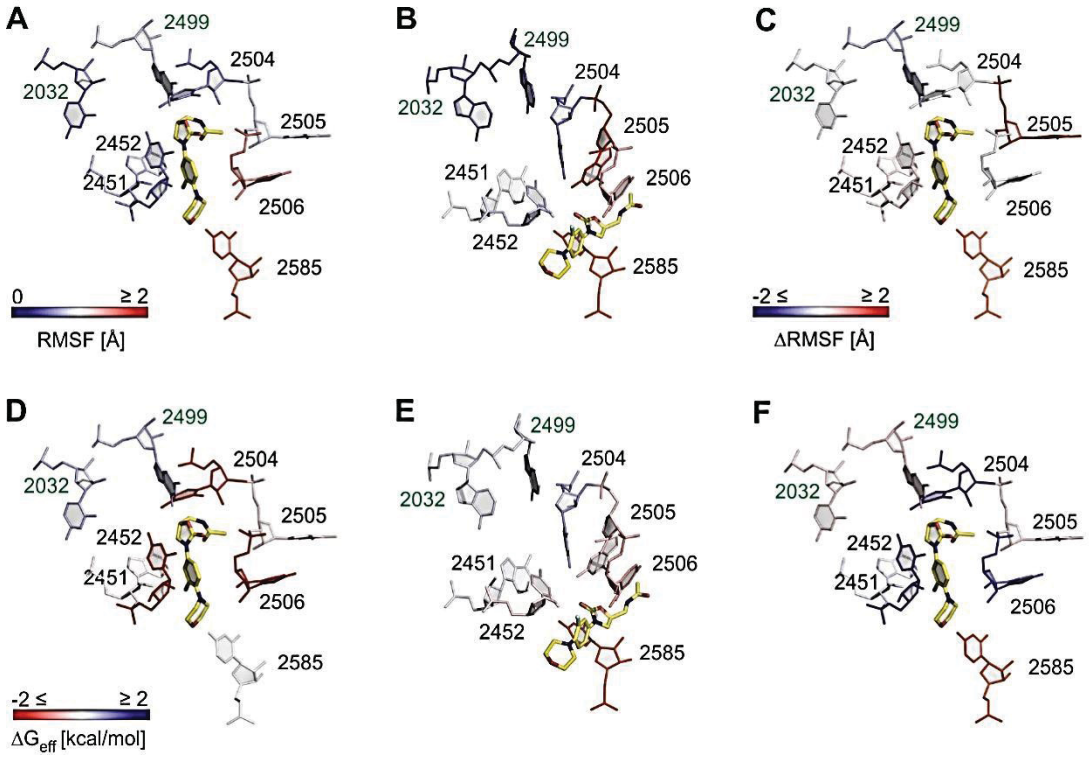

Figure 18: RMSF and per-nucleotide contributions to the effective binding energy. Shown are nucleotides of the 1st shell of the binding site along with the two mutation sites 2032 and 2499 investigated in this study. The structure with the smallest RMSD to the average structure of the last 20 ns of the respective MD trajectory was used for visualization; linezolid is colored in yellow. (A-C): Per-nucleobase RMSF obtained from MD simulations of linezolid-$H50S_{wt}$ (A), linezolid-$H50S_{mut}$ (B) (deep blue: RMSF 0 Å; white: 1 Å; deep red: RMSF ≥ 2 Å) as well as the difference (linezolid-$H50S_{mut}$ – linezolid-$H50S_{wt}$; deep blue: ≤ -2 Å; white: 0 Å; deep red: ≥ 2 Å). (D-F): Per-nucleotide contributions as computed by MM-PBSA for linezolid-$H50S_{wt}$ (D), linezolid-$H50S_{mut}$ (E) as well as the difference (linezolid-$H50S_{mut}$ – linezolid-$H50S_{wt}$) (F) (deep red: ≤ −2 kcal mol^{-1}; white: 0 kcal mol^{-1}; deep blue: ≥ +2 kcal mol^{-1}). Except for the mutated nucleotides, the data for the per-nucleotide decomposition for linezolid-$H50S_{wt}$ has been taken from ref. [119].

Next changes in the network of hydrogen bond and aromatic stacking interactions caused by the G2032A-C2499A double mutation were investigated. In the H50S co-crystal structure, [26] only one hydrogen bond interaction is formed between the acetamide NH group of linezolid and the phosphate group of G2505. This hydrogen bond is missing in the linezolid-D50S crystal structure, [25] indicating its weak nature. In addition, aromatic stacking interactions are formed in the H50S co-crystal structure between the oxazolidinone core and the nucleobase of U2504 as well as between the fluoro-phenyl ring and the nucleobase of C2452 [119]. In the course of the linezolid-H50S$_{wt}$ trajectory, these two aromatic stacking interactions remain stable (Figure 17B, C) whereas the hydrogen bond between linezolid's acetamide NH and G2505 breaks after 4 ns (data not shown) and does not re-form again (Figure 19A) [119]. Instead, the ligand's acetamide NH group forms a strong hydrogen bond with the sugar part of U2504 (occupancy 75%; Figure 19A, grey line) as a result of minor changes of the ligand binding mode. None of these interactions are present in the course of the linezolid-H50S$_{mut}$ trajectory (Figure 19A-C) as expected from the large shift of linezolid described above. Together with C2452, A2451 forms the so-called A-site cleft [119]. Monitoring aromatic stacking interactions between the fluoro-phenyl ring of linezolid and A2451 neither revealed stacking interactions in linezolid-H50S$_{wt}$ nor in linezolid-H50S$_{mut}$, however.

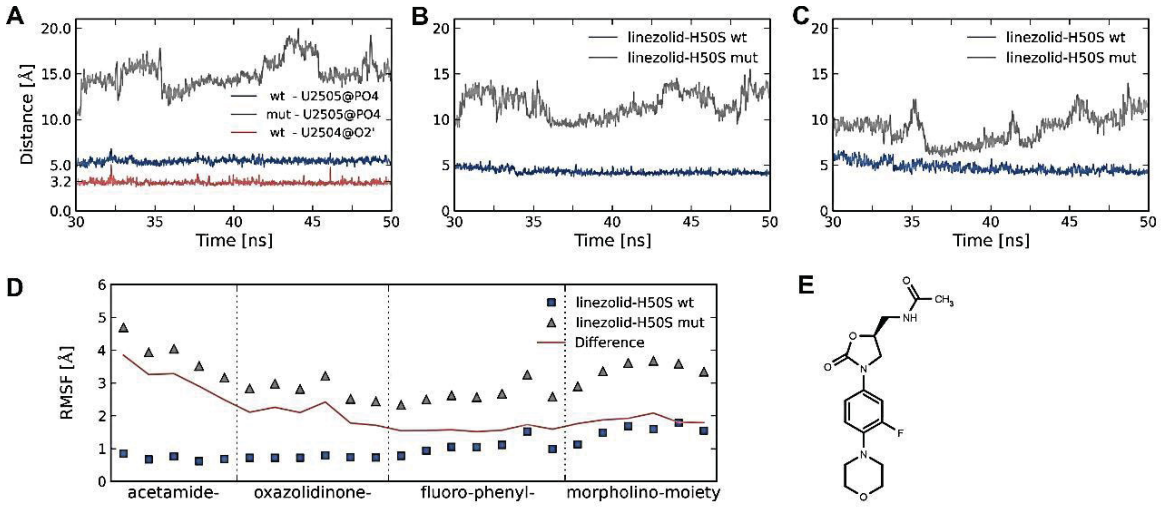

Figure 19: Interactions of linezolid with nucleotides of the 1st shell and RMSF of linezolid. (A): Distances monitoring hydrogen bond formation between linezolid's acetamide NH group and the oxygens of the phosphate group of G2505 (linezolid-H50S$_{wt}$: blue, linezolid-H50S$_{mut}$: grey; only the smallest distance found in each snapshot is plotted) and between linezolid's acetamide NH group and O2' of U2504 (linezolid-H50S$_{wt}$: red). (B and C): Distances monitoring aromatic stacking interactions between the centers of mass of the oxazolidinone core and the nucleobase of U2504 (B), and between the fluoro-phenyl ring and the nucleobase of C2452 (C). Distances for linezolid-H50S$_{wt}$ and linezolid-H50S$_{mut}$ simulations are depicted with blue and grey lines, respectively. (D): RMSF of linezolid atoms during the linezolid-H50S$_{wt}$ (squares) and linezolid-H50S$_{mut}$ (triangles) simulations. The red line represents the difference between the RMSF of linezolid-H50S$_{mut}$ andlinezolid-H50S$_{wt}$ simulations. The data for the linezolid-H50S$_{wt}$ simulation was taken from ref. [119]. (E): Chemical structure of linezolid.

Regarding interactions between nucleotides of the 1st to 3rd shells, strong hydrogen bonds interaction are formed in the linezolid-H50S$_{wt}$ trajectory between nucleotides U2504 and C2452 (occupancy 93%), U2504 and U2500 (occupancy 67%), U2500 and C2452 (occupancy 88%), U2500 and A2055 (occupancy 60%), U2572 and G2032 (occupancies 61% and 66%), as well as between C2499 and A2453 (occupancy 99%) (Figure 20, Table 7). Except for a hydrogen bond between U2504 and U2500 (occupancy 90%), all other hydrogen bonds are absent over the course of the linezolid-H50S$_{mut}$ trajectory (Figure 20). Instead eight new hydrogen bonds are formed in the linezolid-H50S$_{mut}$ trajectory, two between A2451 and G2447 (occupancy 73% and 75%), one between C2452 and A2451 (occupancy 60%), two between U2500 and A2453 (occupancies 82 and 99%), one between U2500 and G2447

(occupancy 73%), one between U2500 and A2032 (occupancy 87%), and one between G2505 and U2504 (occupancy 86%) (Figure 20, Table 7).

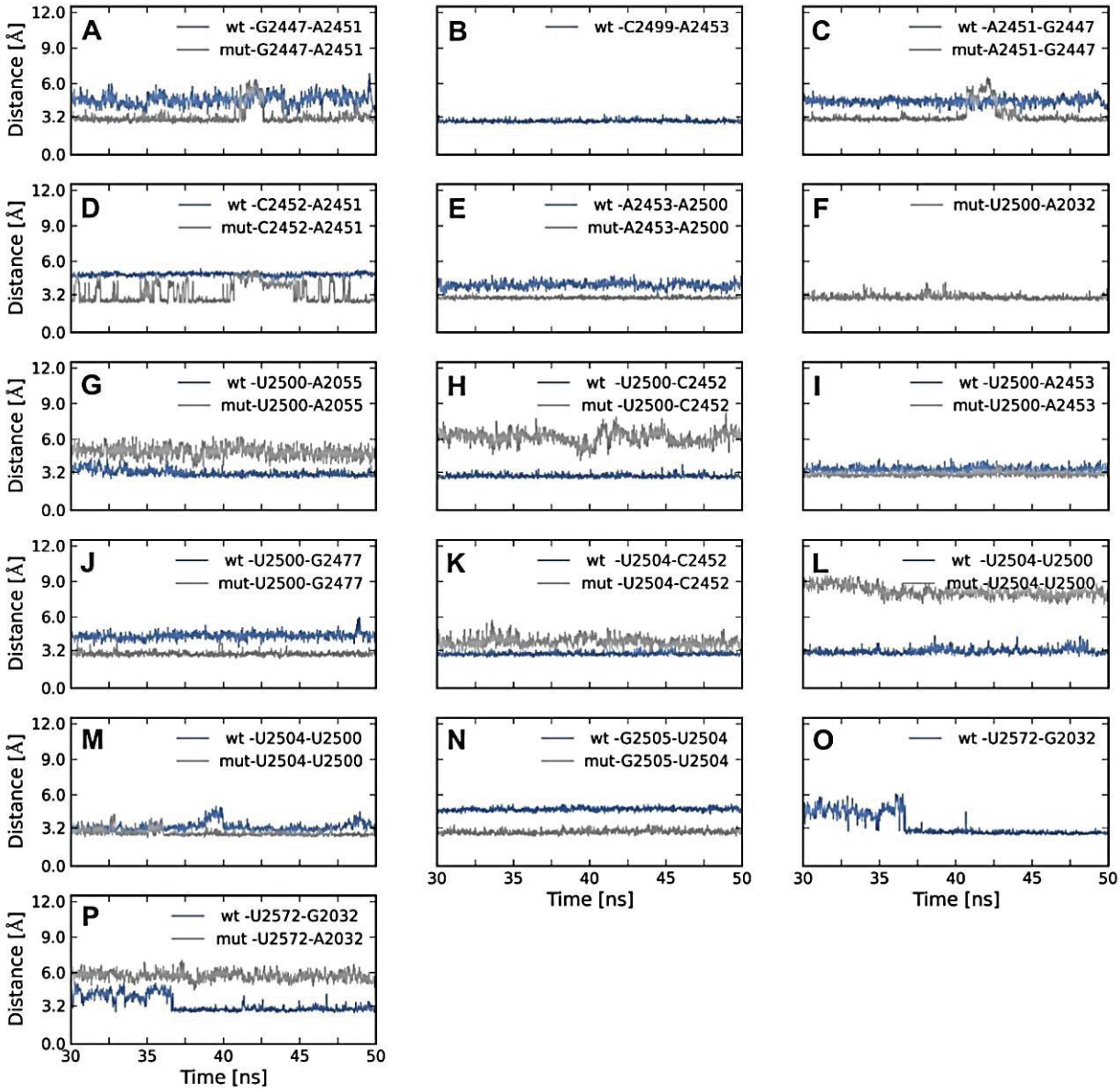

Figure 20: Distances monitoring hydrogen bond formation for linezolid-H50S$_{wt}$ (blue) and linezolid-H50S$_{mut}$ (grey). The monitored distances are ordered according to the number of the acceptor base: i.e., between: (A): G2477@O6 and A2451@N6; (B): C2499@O2 and A2453@N6; (C): A2451@N7 and G2447@N1; (D): C2452@O2P and A2451@O2'; (E): A2453@N1 and U2500@N3; (F): U2500@O2 and A2032@N6; (G): U2500@O2 and A2055@N6; (H): U2500@O4 and C2452@N4; (I): U2500@O4 and A2453@N6; (J): U2500@O5' and G2447@O2'; (K): U2504@O4 and C2452@N4; (L): U2504@O4 and U2500@N3; (M): U2504@O1P and U2500@O2'; (N): G2505@O1P and U2504@O2'; (O): U2572@O2P and G2032@N2;

(P): U2572@O4’ and G/A2032@N1. In the case of the mutated nucleotides C/A2499 and G/A2032 distances are only shown if the respective hydrogen bond is possible.

Table 7. Hydrogen bonds with occupancy values > 60%

Linezolid-H50S$_{wt}$			Linezolid-H50S$_{mut}$		
Acceptor[a]	**Donor[a]**	**% occupied**	**Acceptor[a]**	**Donor[a]**	**% occupied**
-	-	-	G2447@O6	A2451@N6;H62	73
C2499@O2	A2453@N6;H62	99	-	-	-
-	-	-	A2451@N7	G2447@N1;H1	75
-	-	-	C2452@O2P	A2451@O2';HO'	60
-	-	-	A2453@N1	U2500@N3;H3	99
U2500@O2	A2055@N6;H61	60	U2500@O2	A2032@N6;H62	87
U2500@O4	C2452@N4;H42	88	U2500@O4	A2453@N6;H61	82
-	-	-	U2500@O5'	G2447@O2';HO'	73
U2504@O4	C2452@N4;H41	93	-	-	-
U2504@O4	U2500@N3;H3	67	U2504@O1P	U2500@O2';HO'	90
-	-	-	G2505@O1P	U2504@O2';HO'	86
U2572@O2P	G2032@N2;H21	66	-	-	-
U2572@O4'	G2032@N1;H1	61	-	-	-

[a]*E. coli* numbering; the notation after the @ refers to the atom name according to the Amber force field. Nucleotides on white background are in the 1st shell, those on light grey background in the 2nd shell, and those on dark grey background in the 3rd shell. The nucleotides are sorted according to the number of the acceptor base.

Aromatic stacking interactions that occur only in the linezolid-H50S$_{wt}$ trajectory were found between A2055 and U2504; in turn, stacking interactions between A2499 and U2500, A2032 and A2055, A2451 and C2452 as well as G2505 and U2506 occur only in the linezolid-H50S$_{mut}$ trajectory (Figure 21, Table 8).

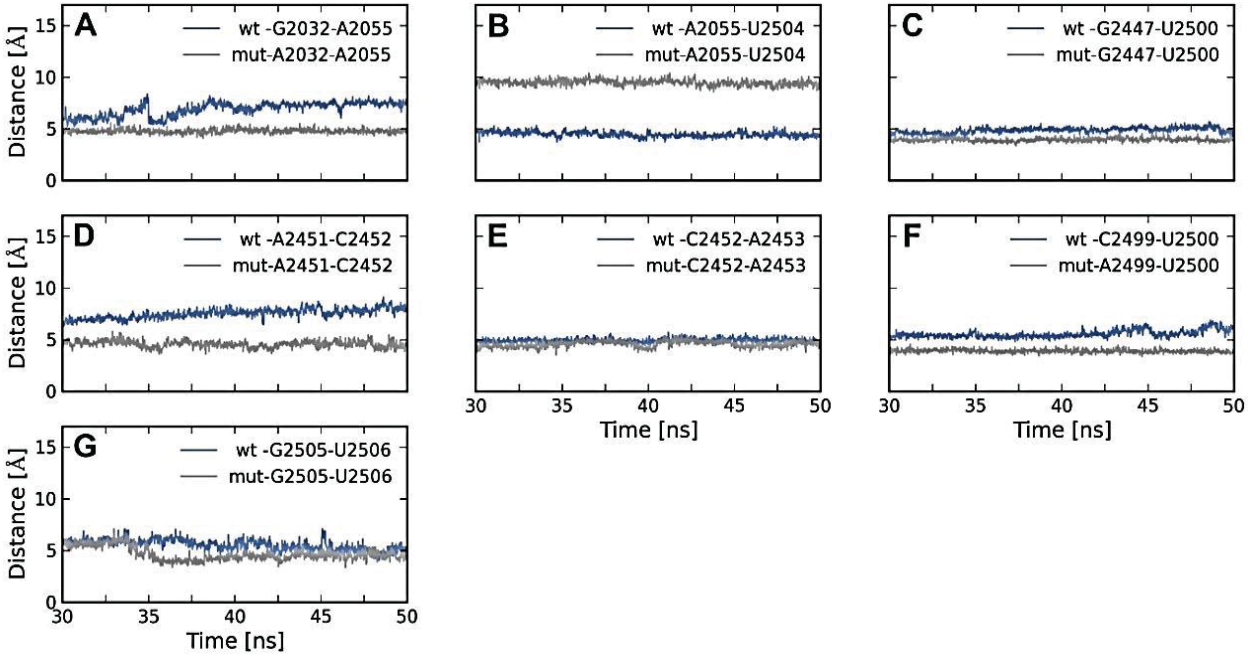

Figure 21: Distances monitoring aromatic stacking interactions for linezolid-H50S$_{wt}$ (blue) and linezolid-H50S$_{mut}$ (grey). The distances were determined between the centers of mass of nucleobases (A): G/A2032 and A2055, (B): A2055 and U2504, (C): G2447 and U2500, (D): A2451 and C2452, (E): C2452 and A2453, (F): C/A2499 and U2500, and (G): G2505 and U2506.

Table 8. Aromatic stacking interactions with occupancy values > 60%.

Linezolid-H50S$_{wt}$			Linezolid-H50S$_{mut}$		
Nucleobase	**Nucleobase**	**% occupied**	**Nucleobase**	**Nucleobase**	**% occupied**
-	-	-	A2032	A2055	84
A2055	U2504	97	-	-	-
G2447	U2500	66	G2447	U2500	100
-	-	-	A2451	C2452	89
C2452	A2453	63	C2452	A2453	92
-	-	-	A2499	U2500	100
-	-	-	G2505	U2506	74

[a]*E. coli* numbering. Nucleotides on white background are in the 1st shell, those on light grey background in the 2nd shell, and those on dark grey background in the 3rd shell. The nucleotides are sorted according to the number of the first base.

In summary, major changes in the interaction network between 1st to 3rd shell nucleotides are observed between linezolid-H50S$_{wt}$ and linezolid-H50S$_{mut}$ despite overall only moderate structural changes (RMSD ~ 2 Å; see above).

6.3.3 Effect of G2032A-C2499A mutations on the dynamics

Higher root-mean square atomic fluctuations (RMSF) (eq. 6) of nucleotides forming the 1st shell of the linezolid binding site (A2451, C2452, G2505, U2506, U2585; (Figure 18A, B)) were found in the linezolid-H50S$_{mut}$ trajectory as compared to the linezolid-H50S$_{wt}$ trajectory, with differences as large as 1.4 Å (U2585; Figure 18C). In contrast, nucleotides U2572 (2nd shell) and G2032 (3rd shell) were slightly more mobile in the linezolid-H50S$_{wt}$ trajectory (differences < 0.4 Å). The higher RMSF of nucleotides A2451 and C2452 in linezolid-H50S$_{mut}$ are surprising at first glance because these nucleotides make hydrogen bonds and stacking interactions with neighboring nucleotides in the linezolid-H50S$_{mut}$ trajectory that do not occur in the linezolid-H50S$_{wt}$ trajectory (see above). However, one needs to consider that linezolid moves away from its starting position in the linezolid-H50S$_{mut}$ trajectory, which removes steric restrictions between the A-site cleft-forming nucleotides A2451 and C2452. In turn, the higher RMSF of G2032 in linezolid-H50S$_{wt}$ can be explained in that G2032 only forms a hydrogen bond to U2572 there but a hydrogen bond to U2500 and stacking interactions to A2055 in linezolid-H50S$_{mut}$ (Table 7 and Table 8).

Regarding the ligand, the highest RMSF over the last 20 ns of the linezolid-H50S$_{wt}$ trajectory are found in the region of the morpholino moiety (average over all atoms: 1.5 Å) whereas the acetamide, oxazolidinone, and fluoro-phenyl moieties are less mobile (0.7, 0.7, and 1.1 Å (Figure 19D,E)) [149]. This is in line with the analysis of stabilizing interactions, which indicated that linezolid's acetamide NH is involved in a hydrogen bond to U2504 (Figure 19A). In contrast, the shifted ligand in the linezolid-H50S$_{mut}$ complex shows RMSF values as high as 4.7 and 3.7 Å at either end of the molecule (Figure 19D), suggesting that linezolid is not tightly bound at its new position.

6.3.4 Effect of G2032A-C2499A mutations on per-nucleotide contributions to the effective binding energy

The above analyses were complemented by a structural decomposition [149] of MM-PBSA effective binding energies in order to investigate differences in the energetic contributions of nucleotides in the first and second shell of the PTC binding site [150]. As in our previous study, [69, 151] we pursued the single-trajectory approach [150-152] as it has proven to be a good and computationally more efficient approximation to the three-trajectory approach in ligand binding studies [78, 119]. The analysis was performed for the last 10 ns of the MD trajectories because the drift in effective binding energies (0.32 kcal mol^{-1} ns^{-1} for linezolid-H50S$_{wt}$ [119]; 3.62 kcal mol^{-1} ns^{-1} for linezolid-H50S$_{mut}$) over time was lowest there for linezolid-H50S$_{wt}$ (Figure 22) [119].

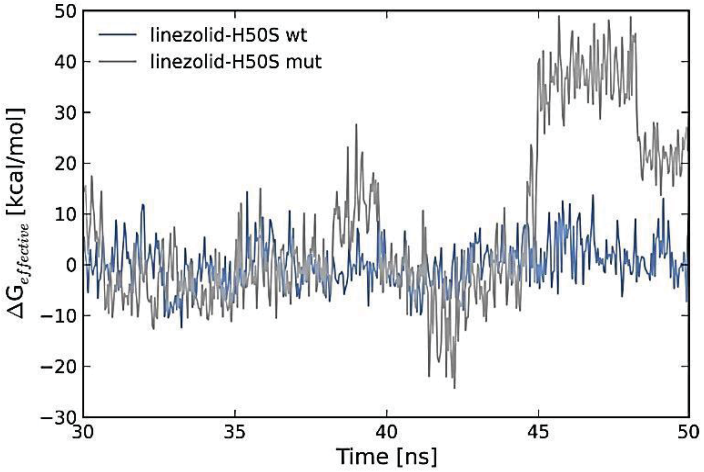

Figure 22: Time series of effective binding energies. Effective binding energies were calculated for 500 snapshots extracted in 20 ps intervals from the last 10 ns of the MD simulations of linezolid-H50S$_{wt}$ (blue) and linezolid-H50S$_{mut}$ (grey). The drifts in the effective binding energies, determined from the slopes of the linear regression lines for linezolid-H50S$_{wt}$ and linezolid-H50S$_{mut}$, are 0.32 kcal mol^{-1} ns^{-1} and 3.62 kcal mol^{-1} ns^{-1}, respectively.

The much larger drift for linezolid-H50S$_{mut}$ can be explained by the displacement of linezolid from its initial binding position further towards the A- and P-sites (Figure 18B). The difference in the total effective binding energy of linezolid in linezolid-H50S$_{mut}$ *versus* linezolid-H50S$_{wt}$ is 7.18 ± 0.77 kcal mol^{-1} (mean ± SEM determined over 500 snapshots extracted in intervals of 20 ps; Table 9). The sign of the difference agrees with experimental

results according to which *M. smegmatis* revealed a minimum inhibitory concentration (MIC) of linezolid of 2 µg ml^{-1} for the wildtype (SZ558 strain) and a MIC of 8 µg ml^{-1} for the G2032A-C2499A mutant [153]. The positive total effective binding energy of 7.38 ± 0.74 kcal mol^{-1} for linezolid binding to $H50S_{mut}$ (Table 9) also reflects that the initial binding mode of linezolid in $H50S_{mut}$ is significantly less stable (Figure 18B).

Table 9. Components of the effective energy for linezolid binding to H50S.[a]

Contribution[b]	Linezolid-H50S$_{wt}$		Linezolid-H50S$_{mut}$		ΔH50S$_{mut}$– H50S$_{wt}$	
	Mean[c]	σ[d]	Mean[c]	σ[d]	Mean[c]	σ[d]
ΔH_{elec}	-2.96	0.03	1.34	0.10	4.30	0.10
ΔH_{vdW}	-40.56	0.14	-32.77	0.21	7.79	0.25
ΔH_{gas}	-43.52	0.14	-31.43	0.17	12.09	0.22
ΔG_{PB}	47.33	0.17	42.36	0.61	-4.97	0.63
$\Delta G_{nonpolar}$	-3.61	0.01	-3.55	0.02	0.06	0.02
$\Delta G_{effective}$	0.20	0.20	7.38	0.74	7.18	0.77

[a] Gas phase and solvation free energy contributions were determined by the MM-PBSA approach, considering 500 snapshots from the last 10 ns of MD simulations of the linezolid-H50S complexes.
[b] H_{elec}: electrostatic energy; H_{vdW} : van der Waals energy; H_{gas} : gas phase energy; G_{PB} : polar part of the solvation free energy; $G_{nonpolar}$: non-polar part of the solvation free energy; $G_{effective}$: effective energy.
[c] Mean contributions in kcal mol^{-1}.
[d] Standard error in the mean values in kcal mol^{-1}.

As to a quantitative comparison, the computed difference in the total effective binding energy seems to exceed the difference in the binding free energy inferred from the MIC (at T = 300 K: ~0.8 kcal mol-1) by ~9-fold. We note, however, that MIC characterizes the lowest concentration of an antibiotic that will inhibit the visible growth of a microorganism after some incubation [153] and as such is generally regarded as the most basic measurement of the activity of an antibiotic against an organism [146]. Several examples for the lack of direct, quantitative correlations between antibiotic binding and the antibiotic sensitivity of the corresponding organism have been noted (e.g., see ref. [155] with respect to penicillin binding). Thus, ideally, our results should be compared to biophysical binding data obtained for H. *marismortui* ribosomes; however, to the best of our knowledge, no such data is available. An inappropriate computational model could be another reason for the variance between the computed difference in the total effective binding energy and the inferred difference in the binding free energy from the MIC. While we cannot exclude this possibility, it appears unlikely to us given that in our recent study on linezolid binding to H50S and D50S, employing the same computational model, the computed ratio of the association constants agreed to within a factor of 100 with the ratio of concentrations required for a successful co-crystallization of linezolid in H50S or D50S [118, 119]. The previous results

reported were also in line with results from functional assays on *Staphylococcus aureus* and *H. marismortui* ribosomes where a selectivity of linezolid towards the eubacterial ribosome was found [139, 119]. Finally, the movement of linezolid from the starting position further towards the A- and P-sites (see above) might result in a linezolid configuration in $H50S_{mut}$ that is still inhibitory and hence explain the small change in the MIC between wildtype and G2032A-C2499A mutant of *M. smegmatis*. In fact, the position occupied by linezolid in $H50S_{mut}$ after the movement overlaps with the binding site of sparsomycin and dalfopristin [136]. However, much longer MD simulations are required to test if the new binding mode of linezolid is stable.

At a per-nucleotide level, C2452 and U2504 show the largest (> 2.9 kcal mol^{-1}) differences in their contributions to the effective binding energy when comparing linezolid-$H50S_{mut}$ *versus* linezolid-$H50S_{wt}$ (Figure 18D-F; Table 4; the SEM in the difference in the effective binding energy due to one nucleotide is assumed to be of a similar magnitude than the one for the overall difference (see above) [119]). Of all 1st shell nucleotides, these nucleotides are closest to the mutation sites in the 3rd shell. U2585 also shows a large difference but of opposite sign (-2.9 kcal mol^{-1}), in line with the fact that this nucleotide interacts favorably with the shifted linezolid in $H50S_{mut}$ (Figure 18E). In all, the nucleotides of the 1st shell contribute almost 90% to the difference in the total effective binding energy (Table 10). In contrast, the 2nd shell contribution is small and even in favor of binding to the mutant (Table 10). These findings are in line with results from our previous study [119] on the proportion of contributions of 1st and 2nd shell nucleotides to the total effective binding energies *per se*. Finally, the contributions of the nucleotides at the mutations sites 2032 and 2499 differ between $H50S_{mut}$ *versus* $H50S_{wt}$ by -0.31 and -0.27 kcal mol^{-1} (Table 10).

Table 10. Effective binding energy contributions between linezolid-H50S$_{mut}$ and linezolid-H50S$_{wt}$ on a per-nucleotide level.[a]

Nucleotide no.[b]	**Linezolid-H50S$_{wt}$[f]**	**Linezolid-H50S$_{mut}$[g]**	**Δ[h]H50S$_{mut}$[g] –H50S$_{wt}$[f]**
A2451[c]	-0.12	0.14	0.26
C2452[c]	-5.54	-0.29	5.25
U2504[c]	-2.41	0.54	2.95
G2505[c]	-0.19	-0.41	-0.22
U2506[c]	-1.79	-0.80	0.99
U2585[c]	0.02	-2.84	-2.86
Σ first shell			6.37
A2055[d]	0.29	0.16	-0.13
G2447[d]	0.17	0.30	0.13
A2453[d]	0.23	0.32	0.09
U2500[d]	0.11	0.20	0.09
U2572[d]	0.80	0.27	-0.53
Σ second shell			-0.35
G/A2032[e]	0.44	0.13	-0.31
C/A2499[e]	0.46	0.19	-0.27
Σ third shell			-0.58

[a] Effective binding energies for first and second shell nucleotides of the ligand binding site were computed by the MM-PBSA approach considering 500 snapshots from the last 10 ns of MD simulations of the linezolid-H50S complexes. In kcal mol^{-1}. The standard error of the mean (SEM) varies between 0.001 and 0.046 kcal mol^{-1}.
[b]Nucleotide number according to *E. coli* numbering.
[c]Nucleotides of the first shell of the ligand binding site.
[d]Nucleotides of the second shell of the ligand binding site.
[e]Nucleotides of the third shell of the ligand binding site.
[f]Wild type H50S in complex with linezolid.
[g]H50S with G2032A-C2499Adouble mutation in complex with linezolid.
[h] Difference between mean effective binding energies for linezolid-H50S$_{mut}$ and linezolid-H50S$_{wt}$.

6.3.5 Conclusions and implications for antibiotics design

This study reveals at an atomistic level how the G2032A-C2499A double mutation in the third shell of the H50S A-site confers linezolid resistance by a complex set of effects that percolate to the antibiotic binding site. From a global point of view, the long-distance effect is markedly manifested by an instable binding mode of linezolid in $H50S_{mut}$ observed already after 10 ns of MD simulations (Figure 22), which is in contrast to stable linezolid binding modes over the last 10 ns of MD simulations observed in $H50S_{wt}$ (Figure 22 and 8) and D50S. The observed linezolid displacement in $H50S_{mut}$ is accompanied by a positive total effective binding energy (Table 9) and high RMSF values of the ligand at the new position (Figure 19D), suggesting that the ligand is not tightly bound at the new position and that a further displacement ought to be expected if the MD simulations were elongated.

At a local level, the effect of the double mutation is summarized in Figure 23. Regarding critical interactions, the binding mode of linezolid in $H50S_{wt}$ is stabilized by a hydrogen bond between the antibiotic's acetamide group and the sugar part of U2504 (Figure 19A) or between the acetamide group and the phosphate group of G2505 (Table 20) as observed in the crystal structure [25, 119]. In addition, stacking interactions between linezolid's fluorophenyl ring and C2452 (Figure 19C), in agreement with the crystal structure [24, 25, 119] and between the oxazolidinone core and U2504 (Figure 19B) occur. Notably, all these interactions are amiss in linezolid-$H50S_{mut}$, most likely as a result of the pronounced conformational changes observed for the respective nucleobases with respect to the starting structure. In agreement, the two nucleotides C2452 and U2504 also show the most disfavorable relative contributions to the effective binding energy at a per-nucleotide level (Figure 18F, Table 9 and 10). In all, our structural and energetic analyses identify U2504 and C2452 as spearheads among the 1st shell nucleotides that exert the most immediate effect on linezolid binding due to the remote double mutation. For U2504, which also has a prominent role in determining the selectivity of antibiotics binding to the A-site [29], a pivotal role in resistance to linezolid via mechanisms by which the nucleotide is perturbed by proximal mutations has been suggested previously based on comparative crystallographic studies [157]. In contrast, aside from a direct mutation [151] C2452 has not yet been linked to linezolid resistance resulting from remote mutations. What leads to C2452 and U2504 being spearheads? The structural decomposition of the difference in effective binding energy (Figure 18F, Table 10, Figure 23A) reveals only minor changes at the per-nucleotide level for nucleotides of the 2nd shell and the mutation sites C/A2499 and G/A2032, which are mostly

slightly in favor of the $H50S_{mut}$ structure. Note that this result must be interpreted with caution because in the single-trajectory MM-PBSA approach pursued here conformational changes of receptor and ligand upon complex formation are ignored [119, 142]. Still, it leads to the interesting suggestions that either the effect of the double mutation does not result in gross structural reorganizations in the 2nd and 3rd shell, and hence no changes in the effective energy are associated with them, or structural reorganizations are associated with mutually compensating changes in the effective energy. The analysis of structural changes and changes in the interaction network indicate that the latter applies (Figure 23A): As to hydrogen bonds 2nd and 3rd shell nucleotides are involved in, five are lost in $H50S_{mut}$ compared to $H50S_{wt}$ (C/A2499···A2453; U2500···A2055; U2500···C2452; U2572···G/A2032 (2x)) and six are formed (G2447···A2451 (2x); U2500···G2447; A2453···U2500 (2x); U2500···A2032); this is accompanied by two stacking interactions involving 2nd and 3rd shell nucleotides formed in $H50S_{mut}$ compared to $H50S_{wt}$ (G/A2032···A2055; C/A2499···U2500) and one lost (A2055···U2504). In line with the balanced numbers of lost and newly formed interactions, the mobility of second and third shell nucleotides only changes marginally between $H50S_{wt}$ and $H50S_{mut}$ (Figure 23A; Table 7).

From this complex reorganization in the network of inter-nucleotide interactions, we can suggest two main routes by which the information of the double mutation is transmitted via 2nd shell nucleotides to U2504 and C2452 (Figure 23B):

I) The G2032A mutation results in the formation of base stacking interactions with A2055, which likely contributes to the loss of stacking interactions of A2055 with U2504, which in turn releases a restraint on the conformation of the U2504 base (Figure 23B; red arrows). Nucleotide 2055 has been described before to have a prominent role in influencing the conformation of the U2504 base in eubacterial *versus* archaeal/eukaryotic ribosomes [29]. Furthermore, the G2032A mutation leads to a loss of a hydrogen bond with U2572 (Figure 23B; red dashed arrow). U2572 in $H50S_{wt}$ has been described to block the U2504 ribose from shifting away from the PTC (Figure 18B; Figure 18A); [29] the lost hydrogen bond may thus release this blocking effect (Figure 23B; grey dashed arrow) although we were unable to observe this on the time scale of our simulations. These findings can explain how the G2032A mutation directly perturbs the conformation of U2504. This result strongly supports the hypothesis that U2504 is important for binding of PTC antibiotics and that its conformation is maintained and restrained, among other second shell nucleotides, by

nucleotides 2055 and 2572, which was previously derived based on the comparative analysis of ribosomal crystal structures [29].

II) In contrast, the C2499A mutation directly perturbs C2452 by way of two subroutes: a) As an immediate effect, the mutation leads to the formation of stacking interactions with U2500, which changes the orientation of the latter base such that a hydrogen bond to C2452 is broken (Figure 23B; blue arrows). b) More indirectly, a hydrogen bond is lost due to the mutation between A2499 and A2453. Because of this and the change in the orientation of U2500 (see a)) hydrogen bonds between A2453 and U2500 as well as U2500 and G2447 are formed. The latter leads to G2447 taking up a new orientation, which allows it to form a hydrogen bond with A2451. Finally, A2451 then forms stacking interactions to C2452 (Figure 23B; blue dashed arrows). Together with a) this leads to a change in the orientation of C2452 such that the stacking interactions with linezolid are lost. To the best of our knowledge, such an indirect perturbation of C2452 by C2499A has not yet been described.

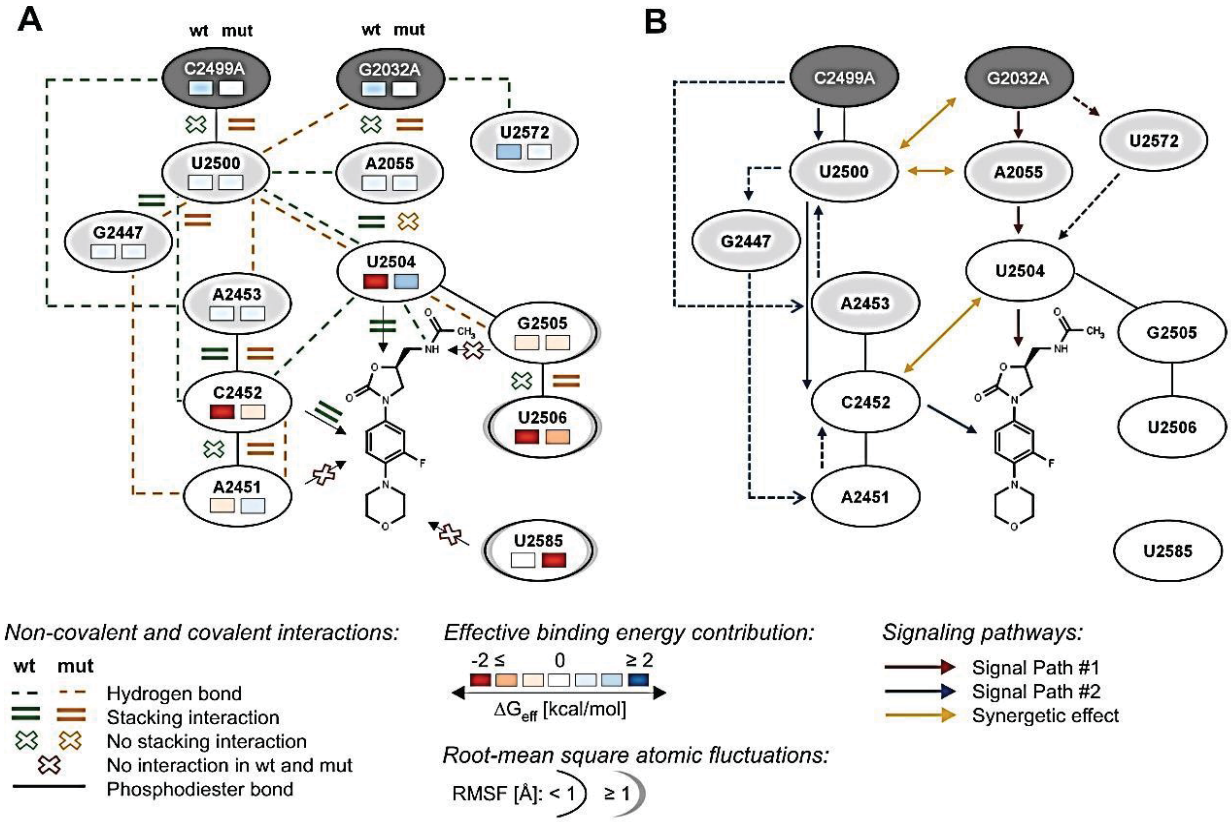

Figure 23: Summary of interactions, contributions to the effective binding energy, and RMSF as well as proposed signaling pathways from the mutation sites to the binding site. (A): Scheme summarizing non-covalent interactions (Table 7, Table 8), contributions to the effective binding energy (Figure 18), and RMSF (Figure 18) of nucleotides forming the 1st (white ellipses) and 2nd (light grey ellipses) shell of the PTC binding site and the two mutation sites (dark grey ellipses). Non-covalent interactions are displayed in green for linezolid-H50S$_{wt}$ and in orange for linezolid-H50S$_{mut}$. Information on contributions to the effective binding energy and RMSF of each nucleotide are depicted on the left side for linezolid-H50S$_{wt}$ and on the right side for linezolid-H50S$_{mut}$, respectively. See the legend for further details. (B**):** Routes by which the information of the double mutation is transmitted via 2nd shell nucleotides to U2504 (red arrows) and C2452 (blue arrows), respectively, as well as synergistic effects between these two routes (yellow arrows). The grey arrow depicts a blocking effect of U2504 by U2572 in H50S$_{wt}$ described in ref. [158] but not observed on the time scale of our simulations.

Although an example for a G2032A (C2499A) mutation without the involvement of 2499 (2032) has been described, leading to linezolid resistance in *E. coli* [157] (*Halobacterium halobium* [159]), usually a G2032A mutation is accompanied by a C2499A mutation [146]. This can be rationalized by the finding of synergistic effects on antibiotic

susceptibilities due to the double mutation, [29] and it has been suggested based on the comparative analysis of ribosomal crystal structures that favorable polar attractions between A2499 and A2032 stabilize the latter nucleotide [160]. However, no hydrogen bond between these two nucleotides in the course of the MD simulation of $H50S_{mut}$ was found. The question arises is what then leads to the observed synergy? The structural analysis suggests that there is cross-talk between the two main routes that transmits information I) from the mutation site G2032A via U2500 to C2452, II) from the C2499A mutation site via U2500 and A2055 to U2504, and III) from U2504 to C2452 and *vice versa* (Figure 23B, yellow arrows): I) the G2032A mutation leads to the formation of a hydrogen bond with U2500; II) the C2499A mutation leads to stacking interactions in $H50S_{mut}$ with U2500 that fosters the fixation of U2500 in a conformation not competent to form a hydrogen bond to A2055; III) the hydrogen bond between C2452 and U2504 is lost in $H50S_{mut}$. These findings suggest that synergistic effects between the two mutations arise from an indirect manner rather than from direct interactions between the mutated nucleotides. However, additional comparisons to MD simulations of linzelid-H50S complex structures with the respective single mutations will be required to provide direct evidence for this.

Table 11. Nucleotide differences in the first and second shell of the linezolid binding site of bacterial, archaeal, and eukaryotic ribosomes.[a]

Nucleotides	Bacteria				Archaea	Eukarya
	E. coli[a]	*D. radiodurans*[b]	*T. thermophilus*[b]	*M. smegmatis*[c]	*H. marismortui*[b]	*S. cerevisiae*[b]
First-shell	A2451	A	A	A	A	A
	C2452	C	C	C	C	C
	U2504	U	U	U	U	U
	G2505	G	G	G	G	G
	U2506	U	U	U	U	U
	U2585	U	U	U	U	U
Second-shell	C2055	**C**	**C**	**C**	**A**	**A**
	G2447	G	G	G	G	G
	A2453	**A**	**A**	**A**	**A**	**U**
	U2500	U	U	U	U	U
	A2572	A	A	A	**U**	A

[a]*E. coli* numbering.
[b]Used PDB codes: *D. radiodurans* (3DLL), *T. thermophilus* (2J01), *H. marismortui* (3CPW), and *S. cerevisiae* (3U5D).
[c] Taken from ref. [119].

To the best of the knowledge, the investigation of resistance to antibiotics binding to the A-site of the 50S ribosomal subunit due to remote mutations by MD simulations and free energy calculations by considering aspects of structure, dynamics, and energetics simultaneously is carried out for the first time. The linezolid-H50S structure [119] was chosen as a model for several reasons: I) This structure has been solved at a resolution of 2.7 Å, [119] which is the highest resolution available for complex structures of linezolid bound to the large ribosomal subunit, and the structure was successfully used in the previous computational study [119, 156]. II) The *archaeal* H50S subunit shows typical *eubacterial* elements at the PTC in that the linezolid-bound conformation of U2504 is nearly identical to

that of the *apo* conformation of the homologous nucleotide in bacterial ribosomes, which can explain why H50S binds oxazolidone antibiotics [15]. III) The H50S subunit possesses *eukaryotic* elements in the second shell PTC nucleotides [15] (Table 5), which can explain why archaeal ribosomes are generally considered more "eukaryotic-like" with respect to their antibiotic specificities [25]. The H50S subunit can thus be regarded as an intermediate, which may be particularly suited for investigating effects of nucleotide exchanges at remote sites on linezolid binding, where low sequence conservations have been observed between eukaryotes and bacteria and which have been associated with species-selectivity of binding and resistance in bacteria.

The analyses of structural, dynamic, and energetic determinants reveal how remote mutations exert an influence on the susceptibility of a PTC antibiotic. The determinants are consistent in describing effects of a complex but balanced reorganization in the network of inter-nucleotide interactions that percolates from the mutation sites to the PTC. In particular, identifying cross-talk between the two main routes of information transfer, which could explain the experimentally observed synergy of the double mutation, goes beyond current knowledge on the structural basis for (cross-)resistance. As demonstrated in this work, it has become possible to explicitly investigate the respective combination of organism/mutation/antibiotic within the time range available by current state-of-the art MD simulations.

7. Conclusion and significance

The current research work is carried out to understand at the atomistic level the binding, selectivity and resistance development of small antibiotics inhibiting process of translation and aims to provide an understanding for designing future antibiotics (Figure 5). Specifically, binding, selectivity and resistance development of oxazolidinone class of antibiotics binding to the 50S subunit of ribsome have been studied in this research work. Oxazolidinone antibiotics bind to the highly conserved peptidyl transferase center in the ribosome. For developing selective antibiotics, a profound understanding of the selectivity determinants is required. Furthermore, since development of resistance to antibiotics is ever increasing, detailed insights into resistance development due to mutation is studided at an atomic level. For the first time technically challenging molecular dynamics simulations in combination with molecular mechanics Poisson-Boltzmann surface area (MM-PBSA) free energy calculations of the oxazolidinones linezolid and radezolid bound to the large ribosomal subunits of the eubacterium *D. radiodurans* and the archaeon *H. marismortui* are performed.

- A remarkably good agreement of the computed relative binding free energies with experimentally available selectivity data available for linezolid is found (Section5).
- Furthermore, binding of radezolid to H50S is more favourable over D50S as shown by stable hydrogen bond, aromatic stacking interactions with residues forming the first shell as well as binding free energy calcualtions. However, structurally related rivaroxaban does not bind to ribosome as shown by displacement from it's initial binding position as well as considerable positive $\Delta G_{effective}$ (Section 5).
- The structural decomposition reveals the most pronounced influence of second shell residues on the selectivity of oxazolidinones for nucleotides 2055 and 2572. This finding is in line with previous reports according to which both nucleotides are involved in restraining the conformational space of U2504 in eubacteria vs. archaea/eucaryotes and, hence, the selectivity of antibiotics binding to the A-site cleft (Section 5).
- Linezolid in $H50S_{mut}$ show unstable binding mode already just after 10 ns of MD simulations, which is in contrast to stable linezolid binding modes over 50 ns of MD simulations observed in $H50S_{wt}$ and D50S. The observed linezolid

displacement in $H50S_{mut}$ is accompanied by high RMSF values of the ligand at the new position and a positive total effective binding energy (Section 6).

- In all, the structural and energetic analyses identify U2504 and C2452 as spearheads among the first shell nucleotides that exert the most immediate effect on linezolid binding due to the remote double mutation. Also, U2504 has a prominent role in determining the selectivity of antibiotics binding to the A-site cleft (Section 6).
- Most importantly, the results presented here are in-line with the recent development in oxazolidinones antibiotics. Potent oxazolidinone derivatives showed activity against linezolid resistant strains already approved by FDA or in advance clinical evaluations, such as radezolid and tedizolid have been modified at the tail end (morpholino) of linezolid and not towards the head part (acetamide). This is explainable by our study where modifications at the tail end are bearable in contrast to the head region as it is least influenced by the here investigated mutations 2499 and 2032 (Section 6).
- Major changes in the interaction network between first to third shell nucleotides are observed between linezolid-$H50S_{wt}$ and linezolid-$H50S_{mut}$ despite overall only moderate structural changes. Our analysis suggest that synergistic effects between the two mutations arise from an indirect manner rather than from direct interactions between the mutated nucleotides (Section 6).

Overall, the analyses reveal an intricate interplay of structural, energetic, and dynamic determinants of the species-selectivity of oxazolidinone antibiotics. Even for the structurally rather similar members; linezolid and radezolid investigated here, significant differences in the (opposing) contributions from interaction energies, solvation, and entropic factors have been identified, as have been influences of first and second shell nucleotides detected. Furthermore, the structural, dynamic, and energetic determinants reveal how remote mutations exert an influence on the susceptibility of the PTC antibiotic. The determinants are consistent in describing effects of a complex but balanced reorganization in the network of inter-nucleotide interactions that percolates from the mutation sites to the PTC**.** In particular, identifying cross-talk between the two main routes of information transfer, which could explain the experimentally observed synergy of the double mutation, goes beyond current knowledge on the structural basis for (cross-)resistance. The possibility to extrapolate our

results to other organisms and/or resistances to other antibiotics is limited due to the complexity of the involved effects. Yet, as demonstrated in this work, it has become possible to explicitly investigate the respective combination of organism/mutation/antibiotic within the time range available by current state-of-the art MD simulations. The study carried by us may help in rational antibiotic discovery and development in the future.

8. Summary and perspective

The current thesis can be understood as a first detailed study into understanding the binding, selectivity and resistance development of oxazolidinone class of antibiotics binding to the large ribosomal subunit. Three different ligands namely linezolid, radezolid (belonging to oxazolidinone class) and rivaroxaban were selected based on their chemical similarity. Since linezolid bound crystal structure was available for both H50S and D50S, these complexes were selected for carrying out the MD simulations. Linezolid was modified inside the binding pocket of both H50S and D50S to yield radezolid and rivaroxaban structures.Furthermore, to understand the role of mutations giving rise to linezolid resistance development, two nucleotides; G2032 and C2499 were selected, as it is known, that out of 10 mutations giving rise to linezolid resistance in bacteria and archaea, the nucleotides corresponding to two of these mutations are already present in the 28S rRNA of *Homo sapiens*. Both these mutation sites are located more than 10 Å away from the linezolid binding site at the PTC and constitute the third shell of nucleotides. Besides, a double mutation at these sequence positions (G2032A-C2499A) observed in *M. smegmatis* showed remarkable synergistic effects on linezolid resistance relative to the effects of the corresponding single mutations. Overall, this makes these sites ideal prototypes for investigating how mutations can confer long distance effects on antibiotics binding (Figure 5). For the first time, MD simulations of time step 50 ns each followed by MM-PBSA was applied to the whole ribosomal complexes, i.e., linezolid-H50S(D50S), radezolid-H50S(D50S), rivaroxaban-H50S(D50S) and linezolid-H50S$_{mut}$.

In summary, the structural and energetic analyses of the oxazolidione-50S complexes reveal significant differences in the effective binding energies and configurational entropies with respect to the binding of linezolid or radezolid to D50S and H50S. Even for the structurally similar ligands: linezolid and radezolid considered in the study, significant differences in the (opposing) contributions from interaction energies, solvation, and entropic factors have been identified. Furthermore, rivaroxaban which shows reasonable structural

similarities with the other two ligands has been shown to be a non-binder to ribosome. As to the selectivity aspect of antibiotics binding to the A-site cleft, the structural decomposition reveals the most pronounced influence of second shell residues on the selectivity of oxazolidinones for nucleotides 2055 and 2572 (Section 5). Finally, as to the development of resistance to linezolid binding, linezolid in $H50S_{mut}$ showed unstable binding mode already just after 10 ns of MD simulations, which is in contrast to stable linezolid binding modes over 50 ns of MD simulations observed in $H50S_{wt}$ and D50S. Overall, the structural and energetic analyses identify U2504 and C2452 as spearheads among the first shell nucleotides that exert the most immediate effect on linezolid binding due to the remote double mutation (Section 6).

As to the implications of the work, oxazolidinones derivatives showing potency against linezolid resistant strains that have undergone advance clinical evaluations or have been approved by FDA, such as radezolid and tedizolid have been modified at the tail end (morpholino) of linezolid and not towards the head part (acetamide). This is proven by our study where modifications at the tail end are bearable in contrast to the head region as it is least influenced by the here investigated mutations 2499 and 2032. It is also important to question the extent to which the results are transferable between species. In our view, one needs to exercise caution in this context given that A2055 in H50S differs from C2055 usually found in bacterial ribosomes and considering the importance of nucleotide 2055 in restraining the conformation of U2504. This view is corroborated by experimental findings according to which the single mutation G2032A confers resistance to linezolid in *E. coli* [158] but neither in *T. thermophiles* [161] nor in *M. smegmatis*, [160] demonstrating organism-dependent effects of the mutation even within a series of bacterial ribosomes. Another question relates to the predictability of cross-resistances from our work. The marked conformational change of U2504 observed in the MD simulations of $H50S_{mut}$ together with this nucleotide's central role in the overlapping binding modes of linezolid, [24] chloramphenicol, [162] and valnemulin (inferred from the binding mode of the related pleuromutilin tiamulin [163]) may rationalize why the G2032A-C2499A double mutation in *M. smegmatis* results in reduced antibiotics susceptibilities in all three cases [160]. However, our findings do not allow to explain why the susceptibility to clindamycin, the binding mode of which overlaps with the ones of the other three antibiotics, [162] is uninfluenced by the double mutation in *M. smegmatis* [160]. Apparently, there is no simple relationship between overlapping binding modes and cross-resistance. Additional (and possibly synergistic) effects

must be considered, such as found in terms of the influence of C2452 on linezolid binding in our case. In our view, this makes the prediction of cross-resistance without explicitly considering the respective mutation and the potentially influenced antibiotic difficult.

The ribosome is a complex, dynamic machine that directs the multi-stage process of translation. Hence, running MD simulations on the full ribosomal complexes to gain insights into antibiotic binding are computationally demanding and resource intensive. It may thus be worth to invest in the development of small RNA model systems of antibiotic binding sites, especially that have been useful to study the A-site of bacterial 16S rRNA in the 30S subunit [164]. However, one must have to take extra care in building up the system and most importantly in interpretation of the results thus obtained. Such model systems normally lack critical information about electrostatic contributions coming from residues that are located far away from the binding pocket. Moreover, such binding site models could not be capable of explaining the long-range mutation effects that are responsible for developing multi-drug resistance in microbes.

Also, determining free energies in a complex system such as ribosome is quite challenging and difficult. In order to obtain estimates of the changes in solvation it would be necessary to perform the free energy calculations in the absence of antibiotic in the ribosomal complex. This is a very challenging calculation which would be further complicated by the likely presence of various ions in the absence of antibiotic under investigation which would in turn impact the solvation energy. Understanding the binding, selectivity and resistance development of antibiotics to the large ribosomal subunit using computational methods like MD simulations and free energy calculations is still in its infancy. Nevertheless, it is anticipated that more advances, increased automation and streamline use of these techniques will successfully help in rational antibiotic discovery and development in future.

References

1. Donadio, S., et al., *Antibiotic discovery in the twenty-first century: current trends and future perspectives.* J Antibiot, 2010. **63**: p. 423-430.
2. Davies, J. and D. Davies, *Origins and Evolution of Antibiotic Resistance.* Microbiol Mol Biol Rev, 2010. **74**(3): p. 417-433.
3. Demain, A.L. and S. Sanchez, *Microbial drug discovery: 80 years of progress.* J Antibiot, 2009. **62**: p. 5-16.
4. Strebhardt, K. and A. Ullrich, *Paul Ehrlich's magic bullet concept: 100 years of progress.* Nat Rev Cancer, 2008. **8**: p. 473-480.
5. Walsh, C.T. and T.A. Wencewicz, *Prospects for new antibiotics: a molecule-centered perspective.* J Antibiot, 2014. **67**(7): p. 7-22.
6. Wilson, D.N. and K.H. Nierhaus, *The Oxazolidinone Class of Drugs Find Their Orientation on the Ribosome.* Mol Cell, 2007. **26**(4): p. 260-262.
7. Wright, G.D., *The antibiotic resistome: the nexus of chemical and genetic diversity.* Nat Rev Microbiol, 2007. **5**(3): p. 175-186.
8. Lewis, K., *Platforms for antibiotic discovery.* Nat Rev Drug Discov, 2013. **12**(5): p. 371-87.
9. Tenover, F.C., *Mechanisms of antimicrobial resistance in bacteria.* Am J Med, 2006. **119**(6 Suppl 1): p. S3-10; discussion S62-70.
10. Woodford, N. and D.M. Livermore, *Infections caused by Gram-positive bacteria: a review of the global challenge.* J Infect, 2009. **59**(S1): p. S4 S16.
11. Blaha, G.M., Y.S. Polikanov, and T.A. Steitz, *Elements of ribosomal drug resistance and specificity.* Curr Opin Struct Biol, 2012. **22**(6): p. 750-758.
12. Steitz, T.A. and P.B. Moore, *RNA, the first macromolecular catalyst: the ribosome is a ribozyme.* Trends Biochem Sci, 2003. **28**(8): p. 411-418.
13. David-Eden, H., A.S. Mankin, and Y. Mandel-Gutfreund, *Structural signatures of antibiotic binding sites on the ribosome.* Nucleic Acids Res, 2010. **38**(18): p. 5982-94.
14. Rodnina, M.V., *The ribosome as a versatile catalyst: reactions at the peptidyl transferase center.* Curr Opin Struct Biol, 2013. **23**(4): p. 595-602.
15. Yonath, A., *Antibiotics targeting ribosomes: resistance, selectivity, synergism and cellular regulation.* Annu Rev Biochem, 2005. **74**: p. 649-679.
16. Spirin, A.S., *Ribosome as a molecular machine.* FEBS Lett, 2002. **514**: p. 2-10.
17. Wilson, D.N., *The A-Z of bacterial translation inhibitors.* Crit Rev Biochem Mol Biol, 2009. **44**(6): p. 393-433.
18. Bulkley, D., et al., *Revisiting the structures of several antibiotics bound to the bacterial ribosome.* Proc Natl Acad Sci USA, 2010. **107**(27): p. 17158-17163.
19. Schlunzen, F., et al., *Structural basis for the interaction of antibiotics with the peptidyl transferase centre in eubacteria.* Nature, 2001. **413**(6858): p. 814-821.
20. Matassova, N.B., et al., *Ribosomal RNA is the target for oxazolidinones, a novel class of translational inhibitors.* RNA, 1999. **5**(7): p. 939-46.
21. Stefani, S., et al., *Linezolid Resistance in Staphylococci.* Pharmaceuticals, 2010. **3**: p. 1988-2006.
22. Leach, K.L., et al., *Linezolid, the first oxazolidinone antibacterial agent.* Ann N Y Acad Sci, 2011. **1222**: p. 49-54.
23. Long, K.S., et al., *Mutations in 23S rRNA at the peptidyl transferase center and their relationship to linezolid binding and cross-resistance.* Antimicrob Agents Chemother, 2010. **54**(11): p. 4705-4713.

24. Ippolito, J.A., et al., *Crystal structure of the oxazolidinone antibiotic linezolid bound to the 50S ribosomal subunit.* J Med Chem, 2008. **51**(12): p. 3353-3356.
25. Wilson, D.N., et al., *The oxazolidinone antibiotics perturb the ribosomal peptidyl-transferase center and effect tRNA positioning.* Proc Natl Acad Sci USA, 2008. **105**(36): p. 13339-13344.
26. Bottger, E.C., et al., *Structural basis for selectivity and toxicity of ribosomal antibiotics.* EMBO Rep, 2001. **2**(4): p. 318-323.
27. Wilson, D.N., et al., *Species-specific antibiotic-ribosome interactions: implications for drug development.* Biol Chem, 2005. **386**(12): p. 1239-52.
28. Romanowska, J., J.A. McCammon, and J. Trylska, *Understanding the origins of bacterial resistance to aminoglycosides through molecular dynamics mutational study of the ribosomal A-site.* PLoS Comput Biol, 2011. **7**(7): p. 1-6.
29. Davidovich, C., A. Bashan, and A. Yonath, *Structural basis for cross-resistance to ribosomal PTC antibiotics.* Proc Natl Acad Sci USA, 2008. **105**(52): p. 20665-20670.
30. Darden, T., D. York, and L. Pedersen, *Particle mesh Ewald: An N log (N) method for Ewald sums in large systems.* J Chem Phys, 1993. **98**: p. 10089.
31. Sanbonmatsu, K.Y. and C.S. Tung, *High performance computing in biology: multimillion atom simulations of nanoscale systems.* J Struct Biol, 2007. **157**: p. 470-480.
32. Sanbonmatsu, K.Y., S. Joseph, and C.-S. Tung, *Simulating movement of tRNA into the ribosome during decoding.* Proc Natl Acad Sci USA, 2005. **102**: p. 15854-15859.
33. Vaiana, A.C. and K.Y. Sanbonmatsu, *Stochastic gating and drug-ribosome interactions.* J Mol Biol, 2009. **386**: p. 648-661.
34. Petrone, P.M., et al., *Side-chain recognition and gating in the ribosome exit tunnel.* Proc Natl Acad Sci USA, 2008. **105**: p. 16549-16554.
35. Ishida, H. and S. Hayward, *Path of nascent polypeptide in exit tunnel revealed by molecular dynamics simulation of ribosome.* Biophys J, 2008. **95**: p. 5962-5973.
36. Chen, S.Y. and T.H. Lin, *A molecular dynamics study on binding recognition between several 4,5 and 4,6-linked aminoglycosides with A-site RNA.* J Mol Recognit, 2010. **23**(5): p. 423-434.
37. Ge, X. and B. Roux, *Absolute binding free energy calculations of sparsomycin analogs to the bacterial ribosome.* J Phys Chem B, 2010. **114**(29): p. 9525-9539.
38. Small, M.C., et al., *Impact of ribosomal modification on the binding of the antibiotic telithromycin using a combined grand canonical monte carlo/molecular dynamics simulation approach.* PLoS Comput Biol, 2013. **9**(6): p. e1003113.
39. Sothiselvam, S., et al., *Macrolide antibiotics allosterically predispose the ribosome for translation arrest.* Proc Natl Acad Sci USA, 2014. **111**(27): p. 9804-9.
40. Grunenberg, J. and G. Licari, *Effective in silico prediction of new oxazolidinone antibiotics: force field simulations of the antibiotic-ribosome complex supervised by experiment and electronic structure methods.* Beilstein J Org Chem, 2016. **12**: p. 415-28.
41. Karplus, M. and J.A. McCammon, *Molecular dynamics simulations of biomolecules.* Nat Struct Biol, 2002. **9**: p. 646-652.
42. Latour, R.A., *Molecular simulation of protein-surface interactions: Benefits, problems, solutions, and future directions (Review).* Biointerphases, 2008. **3**(3): p. FC2-FC12.
43. Lindert, S., et al., *Accelerated Molecular Dynamics Simulations with the AMOEBA Polarizable Force Field on Graphics Processing Units.* J Chem Theory Comput, 2013. **9**(11): p. 4684-4691.

44. MartÃn-GarcÃa, F., et al., *Comparing molecular dynamics force fields in the essential subspace.* PLoS One, 2015. **10**(3): p. e0121114.
45. Leach, A.R., *Molecular modelling : principles and applications*. 2nd ed. 2001: Harlow, England ; New York: Prentice Hall.
46. Lindorff-Larsen, K., et al., *Systematic validation of protein force fields against experimental data.* PLoS One, 2012. **7**(2): p. e32131.
47. Hashem, Y. and P. Auffinger, *A short guide for molecular dynamics simulations of RNA systems.* Methods, 2009. **47**(3): p. 187-97.
48. Cino, E.A., W.-Y. Choy, and M. Karttunen, *Comparison of secondary structure formation using 10 different force fields in microsecond molecular dynamics simulations.* J Chem Theory Comput, 2012. **8**(8): p. 2725-2740.
49. Sponer, J., et al., *Molecular Dynamics Simulations of RNA Molecules*. Vol. 2. 2012: the Royal Society of Chemistry.
50. Weiner, S.J., et al., *A new force field for molecular mechanical simulation of nucleic acids and proteins.* J Am Chem Soc, 1984. **106**(3): p. 765-784.
51. Galindo-Murillo, R., et al., *Assessing the Current State of Amber Force Field Modifications for DNA.* J Chem Theory Comput, 2016. **12**(8): p. 4114-27.
52. Brooks, B.R., et al., *CHARMM: The Biomolecular Simulation Program.* J Comput Chem, 2009. **30**(10): p. 1545-1614.
53. Neria E, F.S., Karplus, M., *Simulation of activation free energies in molecular systems.* J Chem Phys, 1996. **105**(5): p. 1902–1921.
54. MacKerell, A.D., Jr., N. Banavali, and N. Foloppe, *Development and current status of the CHARMM force field for nucleic acids.* Biopolymers, 2000. **56**(4): p. 257-65.
55. Tanford, C., *The hydrophobic effect and the organization of living matter.* Science, 1978. **200**(4345): p. 1012-8.
56. Eisenberg, D. and A.D. McLachlan, *Solvation energy in protein folding and binding.* Nature, 1986. **319**(6050): p. 199-203.
57. Fogolari, F., A. Brigo, and H. Molinari, *Protocol for MM/PBSA Molecular Dynamics Simulations of Proteins.* Biophysical Journal, 2003. **85**(1): p. 159-166.
58. Honig, B. and A. Nicholls, *Classical electrostatics in biology and chemistry.* Science, 1995. **268**(5214): p. 1144-9.
59. Ren, P., et al., *Biomolecular electrostatics and solvation: a computational perspective.* Q Rev Biophys, 2012. **45**(4): p. 427-491.
60. Sitkoff, D., K.A. Sharp, and B. Honig, *Accurate calculation of hydration free energies using macroscopic solvent models.* J Phys Chem, 1994. **98**(7): p. 1978-1988.
61. Sharp, K., *Incorporating solvent and ion screening into molecular dynamics using the finiteâ€• difference Poisson-Boltzmann method.* J Chem Theory Comput, 1991. **12**(4): p. 454-468.
62. Niedermeier, C. and K. Schulten, *Molecular Dynamics Simulations in Heterogeneous Dielectrica and Debye-Huckel Media - Application to the Protein Bovine Pancreatic Trypsin Inhibitor.* Mol Simul, 1992. **8**(6): p. 361-387.
63. David, L., R. Luo, and M.K. Gilson, *Comparison of generalized born and poisson models: Energetics and dynamics of HIV protease.* J Comput Chem, 2000. **21**(4): p. 295-309.
64. Lu, B.Z., et al., *Protein molecular dynamics with electrostatic force entirely determined by a single Poisson-Boltzmann calculation.* Proteins, 2002. **48**(3): p. 497-504.
65. Fogolari, F., et al., *Molecular mechanics and dynamics of biomolecules using a solvent continuum model.* J Comput Chem, 2001. **22**(15): p. 1830-1842.

66. Roux, B. and T. Simonson, *Implicit solvent models.* Biophys Chem, 1999. **78**(1-2): p. 1-20.
67. Simonson, T., *Macromolecular electrostatics: continuum models and their growing pains*. Curr Opin Struct Biol, 2001. **11**(2): p. 243-52.
68. Chen, J., C.L. Brooks, and J. Khandogin, *Recent advances in implicit solvent based methods for biomolecular simulations.* Curr Opin Struct Biol, 2008. **18**(2): p. 140-148.
69. Metz, A., et al., *Hot Spots and Transient Pockets: Predicting the Determinants of Small-Molecule Binding to a Protein-Protein Interface.* J Chem Inf Model, 2012. **52**(1): p. 120-133.
70. Kopitz, H., et al., *Influence of the solvent representation on vibrational entropy calculations: generalized born versus distance-dependent dielectric model.* J Comput Chem, 2012. **33**(9): p. 1004-1013.
71. Ciglia, E., et al., *Resolving Hot Spots in the C-Terminal Dimerization Domain that Determine the Stability of the Molecular Chaperone Hsp90.* PLoS One, 2014. **9**(4): p. e96031.
72. Homeyer, N., et al., *Interpreting Thermodynamic Profiles of Aminoadamantane Compounds Inhibiting the M2 Proton Channel of Influenza A by Free Energy Calculations.* J Chem Inf Model, 2016. **56**(1): p. 110-26.
73. Lazaridis, T. and M. Karplus, *Effective energy function for proteins in solution.* Proteins, 1999. **35**(2): p. 133-52.
74. Hill, T.L., *An Introduction to Statistical Thermodynamics*. 1956: Dover Publications, New York.
75. Kollman, P.A., et al., *Calculating structures and free energies of complex molecules: combining molecular mechanics and continuum models.* Acc Chem Res, 2000. **33**(12): p. 889-97.
76. Srinivasan, J., et al., *Continuum Solvent Studies of the Stability of DNA, RNA, and Phosphoramidate-DNA Helices.* J Am Chem Soc, 1998. **120**: p. 9401-9409.
77. Case, D.A., et al., *The Amber biomolecular simulation programs.* J Chem Theory Comput, 2005. **26**(16): p. 1668-1688.
78. Homeyer, N. and H. Gohlke, *Free energy calculations by the molecular mechanics poisson−boltzmann surface area method.* Mol Inf, 2012. **31**(2): p. 114-122.
79. Khosa, S., et al., *Structural basis of lantibiotic recognition by the nisin resistance protein from Streptococcus agalactiae.* Sci Rep, 2016. **6**: p. 1-13.
80. Ben-Shalom, I.Y., et al., *Efficient Approximation of Ligand Rotational and Translational Entropy Changes upon Binding for Use in MM-PBSA Calculations.* J Chem Inf Model, 2017. **57**(2): p. 170-189.
81. Gumbart, J.C., B.t. Roux, and C. Chipot, *Standard binding free energies from computer simulations: What is the best strategy?* J Chem Theory Comput, 2013. **9**(1): p. 794-802.
82. Lawrenz, M., et al., *Thermodynamic integration to predict host-guest binding affinities.* J Comput Aided Mol Des, 2012. **26**(5): p. 569-576.
83. Gohlke, H. and D.A. Case, *Converging free energy estimates: MM-PB(GB)SA studies on the protein-protein complex Ras-Raf.* J Comput Chem, 2004. **25**(2): p. 238-250.
84. Gohlke, H., C. Kiel, and D.A. Case, *Insights into protein-protein binding by binding free energy calculation and free energy decomposition for the Ras-Raf and Ras-RalGDS complexes.* J Mol Biol, 2003. **330**(4): p. 891-913.
85. Cornell, W.D., et al., *A second generation force field for the simulation of proteins, nucleic acids, and organic molecules.* J Am Chem Soc, 1995. **117**(19): p. 5179-5197.

86. Weiser, J., P.S. Shenkin, and W.C. Still, *Approximate atomic surfaces from linear combinations of pairwise overlaps (LCPO).* J. Comput. Chem., 1999. **20**(2): p. 217-230.
87. Baker, N.A., et al., *Electrostatics of nanosystems: application to microtubules and the ribosome.* Proc Natl Acad Sci USA, 2001. **98**(18): p. 10037-10041.
88. Moellering, R.C., *Linezolid: the first oxazolidinone antimicrobial.* Ann Intern Med, 2003. **138**(2): p. 135-142.
89. Shaw, K.J. and M.R. Barbachyn, *The oxazolidinones: past, present, and future.* Ann N Y Acad Sci, 2011. **1241**: p. 48-70.
90. Skripkin, E., et al., *Rχ-01, a new family of oxazolidinones that overcome ribosome-based linezolid resistance.* Antimicrob Agents Chemother, 2008. **52**(10): p. 3550-3557.
91. Zhou, J., et al., *Design at the atomic level: design of biaryloxazolidinones as potent orally active antibiotics.* Bioorg Med Chem Lett, 2008. **18**(23): p. 6175-6178.
92. Hornak, V., et al., *Comparison of multiple Amber force fields and development of improved protein backbone parameters.* Proteins: Struct., Funct., Bioinf., 2006. **65**(3): p. 712-725.
93. Wang, J., et al., *Development and testing of a general amber force field.* J Comput Chem, 2004. **25**: p. 1157-1174.
94. Frisch, M.J., et al., *Gaussian 03*. 2004, Gaussian, Inc.: Wallingford CT.
95. Wang, J., et al., *Automatic atom type and bond type perception in molecular mechanical calculations.* J Mol Graphics Modell, 2006. **25**(2): p. 247-260.
96. Bayly, C.I., et al., *A well-behaved electrostatic potential based method using charge restraints for deriving atomic charges: the RESP model.* J. Phys. Chem. B, 1993. **97**: p. 10269-10280.
97. Åqvist, J., *Modelling of ion-ligand interactions in solutions and biomolecules.* J Mol Struct, 1992. **256**: p. 135-152.
98. Hoops, S.C., K.W. Anderson, and K.M. Merz, *Force field design for metalloproteins.* J Am Chem Soc, 1991. **113**(22): p. 8262-8270.
99. Sali, A. and T.L. Blundell, *Comparative protein modelling by satisfaction of spatial restraints.* J Mol Biol, 1993. **234**(3): p. 779-815.
100. MacroModel, *version 9.9, Schrödinger, LLC, New York, NY*. 2012.
101. Jorgensen, W.L., et al., *Comparison of simple potential functions for simulating liquid water.* J Chem Phys, 1983. **79**: p. 926-935.
102. Cheatham, T.E., III, et al., *Molecular dynamics simulations on solvated biomolecular systems: The Particle Mesh Ewald Method leads to stable trajectories of DNA, RNA, and proteins.* J Am Chem Soc, 1995. **117**: p. 4193-4194.
103. Ryckaert, J.P., G. Ciccotti, and H.J.C. Berendsen, *Numerical integration of the Cartesian equations of motion of a system with constraints: molecular dynamics of n-alkanes.* J Comput Phys, 1977. **23**: p. 327-341.
104. Williams, T. and C. Kelley, *gnuplot 4.2*. 2009.
105. PyMOL, *The PyMOL Molecular Graphics System, Version 1.3r1, Schrödinger, LLC*. 2010.
106. Srinivasan, J., et al., *Continuum solvent studies of the stability of DNA, RNA, and phosphoramidate−DNA Helices.* J Am Chem Soc, 1998. **120**(37): p. 9401-9409.
107. Trylska, J., et al., *Ribosome motions modulate electrostatic properties.* Biopolymers, 2004. **74**(6): p. 423-431.
108. Weiser, J., P.S. Shenkin, and W.C. Still, *Approximate atomic surfaces from linear combinations of pairwise overlaps (LCPO).* J Comput Chem, 1999. **20**: p. 217-230.

109. Yonath, A. and A. Bashan, *Ribosomal crystallography: initiation, peptide bond formation, and amino acid polymerization are hampered by antibiotics.* Annu. Rev. Microbiol., 2004. **58**: p. 233-251.
110. Auerbach, T., A. Bashan, and A. Yonath, *Ribosomal antibiotics: structural basis for resistance, synergism and selectivity.* Trends Biotechnol, 2004. **22**(11): p. 570-576.
111. Arunan, E. and H.S. Gutowsky, *The rotational spectrum, structure and dynamics of a benzene dimer.* J Chem Phys, 1993. **98**(5): p. 4294-4296.
112. Blaha, G., et al., *Mutations outside the anisomycin-binding site can make ribosomes drug-resistant.* J. Mol. Biol., 2008. **379**(3): p. 505-519.
113. Fulle, S. and H. Gohlke, *Statics of the ribosomal exit tunnel: implications for cotranslational peptide folding, elongation regulation, and antibiotics binding.* J Mol Biol, 2009. **387**(2): p. 502-517.
114. Ge, X. and B. Roux, *Calculation of the standard binding free energy of sparsomycin to the ribosomal peptidyl-transferase P-site using molecular dynamics simulations with restraining potentials.* J Mol Recognit, 2009. **23**(2): p. 128-141.
115. Hou, T., et al., *Assessing the performance of the MM/PBSA and MM/GBSA methods. 1. The accuracy of binding free energy calculations based on molecular dynamics simulations.* J Chem Inf Model, 2011. **51**(1): p. 69-82.
116. Huo, S., et al., *Molecular dynamics and free energy analyses of cathepsin D-inhibitor interactions: insight into structure-based ligand design.* J Med Chem, 2002. **45**(7): p. 1412-1419.
117. Yang, T., et al., *Virtual screening using molecular simulations.* Proteins: Struct., Funct., Bioinf., 2011. **79**(6): p. 1940–1951.
118. Wilson, D.N., *On the specificity of antibiotics targeting the large ribosomal subunit.* Ann N Y Acad Sci, 2011. **1241**: p. 1-16.
119. Saini, J.S., et al., *Determinants of the species-selectivity of oxazolidinone antibiotics targeting the large ribosomal subunit.* Biol Chem, 2013. **394**(11): p. 1529-1541.
120. Brady, G.P. and K.A. Sharp, *Entropy in protein folding and in protein-protein interactions.* Curr Opin Struct Biol, 1997. **7**(2): p. 215-221.
121. Singh, N. and A. Warshel, *A comprehensive examination of the contributions to the binding entropy of protein-ligand complexes.* Proteins: Struct., Funct., Bioinf., 2010. **78**(7): p. 1724-1735.
122. Wichmann, C., et al., *Dimer-tetramer transition controls RUNX1/ETO leukemogenic activity.* Blood, 2010. **116**(4): p. 603-613.
123. Fulle, S., et al., *Molecular Determinants of Binding to the Plasmodium Subtilisin-like Protease 1.* J Chem Inf Model, 2013. **53**(3): p. 573–583.
124. Selzer, T., S. Albeck, and G. Schreiber, *Rational design of faster associating and tighter binding protein complexes.* Nat Struct Biol, 2000. **7**(7): p. 537-541.
125. Locke, J.B., et al., *Structure-activity relationships of diverse oxazolidinones for linezolid-resistant Staphylococcus aureus strains possessing the cfr methyltransferase gene or ribosomal mutations.* Antimicrob Agents Chemother, 2010. **54**(12): p. 5337-5343.
126. Gregory, W.A., et al., *Antibacterials. Synthesis and structure-activity studies of 3-aryl-2-oxooxazolidines. 2. The "A" group.* J Med Chem, 1990. **33**(9): p. 2569-2578.
127. Gregory, W.A., et al., *Antibacterials. Synthesis and structure-activity studies of 3-aryl-2-oxooxazolidines. 1. The "B" group.* J. Med. Chem., 1989. **32**(8): p. 1673-1681.
128. Park, C.H., et al., *Antibacterials. synthesis and structure-activity studies of 3-aryl-2-oxooxazolidines. 4. Multiply-substituted aryl derivatives.* J Med Chem, 1992. **35**(6): p. 1156-1165.

129. Barbachyn, M.R. and C.W. Ford, *Oxazolidinone structure-activity relationships leading to linezolid.* Angew. Chem., Int. Ed. Engl., 2003. **42**(18): p. 2010-2023.
130. Brickner, S.J., et al., *Linezolid (ZYVOX), the first member of a completely new class of antibacterial agents for treatment of serious gram-positive infections.* J Med Chem, 2008. **51**(7): p. 1981–1990.
131. Brickner, S.J., et al., *Synthesis and antibacterial activity of U-100592 and U-100766, two oxazolidinone antibacterial agents for the potential treatment of multidrug-resistant gram-positive bacterial infections.* J. Med. Chem., 1996. **39**(3): p. 673-679.
132. Zhou, J., et al., *Design at the atomic level: generation of novel hybrid biaryloxazolidinones as promising new antibiotics.* Bioorg Med Chem Lett, 2008. **18**(23): p. 6179-6183.
133. MCPRO, *Schrödinger, LLC, New York, NY*. 2009.
134. Franceschi, F., et al. *Radezolid Overcomes cfr-mediated Linezolid-resistance by Efficiently Inhibiting Protein Synthesis of cfr-methylated Ribosomes*. in *Interscience Conference on Antimicrobial Agents and Chemotherapy*. 2010. Boston, Massachusetts, U.S.A.
135. Gürel, G., et al., *U2504 determines the species specificity of the A-site cleft antibiotics: the structures of tiamulin, homoharringtonine, and bruceantin bound to the ribosome.* J Mol Biol, 2009. **389**(1): p. 146-156.
136. Wilson, D.N., *Ribosome-targeting antibiotics and mechanisms of bacterial resistance.* Nat Rev Microbiol, 2014. **12**(1): p. 35-48.
137. Shaw, K.J. and M.R. Barbachyn, *The oxazolidinones: past, present, and future.* Ann. N.Y. Acad. Sci, 2011. **1241**: p. 48-70.
138. Lawrence, L., et al., *In vitro activities of the Rx-01 oxazolidinones against hospital and community pathogens.* Antimicrob Agents Chemother, 2008. **52**(5): p. 1653-1662.
139. Skripkin, E., et al., *R chi-01, a new family of oxazolidinones that overcome ribosome-based linezolid resistance.* Antimicrobial Agents and Chemotherapy, 2008. **52**(10): p. 3550-3557.
140. Mlynsky, V., et al., *Extensive molecular dynamics simulations showing that canonical G8 and protonated A38H$^+$ forms are most consistent with crystal structures of hairpin ribozyme.* J. Phys. Chem. B, 2010. **114**(19): p. 6642-6652.
141. Zgarbova, M., et al., *Refinement of the Cornell et al. nucleic acids force field based onreference quantum chemical calculations of glycosidic torsion profiles.* J. Chem. Theory Comput., 2011. **7**(9): p. 2886-2902.
142. Sitkoff, D., K.A. Sharp, and B. Honig, *Correlating solvation free energies and surface tensions of hydrocarbon solutes.* Biophys. Chem, 1994. **51**: p. 397-403.
143. Gaulton, A., et al. *ChEMBL: a large-scale bioactivity database for drug discovery.* Nucleic Acids Res. 2011. **40:** p.D1100–D1107.
144. Luo,R., David,L. and Gilson,M.K., *Accelerated Poisson-Boltzmann calculations for static and dynamic systems*. J.Comput. Chem., 2002. **23**: p. 1244–1253.
145. Long, K.S. and B. Vester, *Resistance to linezolid caused by modifications at its binding site on the ribosome.* Antimicrob Agents Chemother, 2012. **56**(2): p. 603-12.
146. Pringle, M., et al., *Mutations in ribosomal protein L3 and 23S ribosomal RNA at the peptidyl transferase centre are associated with reduced susceptibility to tiamulin in Brachyspira spp. isolates.* Mol Microbiol, 2004. **54**(5): p. 1295-1306.
147. Butler, M.S., M.A. Blaskovich, and M.A. Cooper, *Antibiotics in the clinical pipeline in 2013.* Journal of Antibiotics, 2013. **66**(10): p. 571-591.
148. Fair, R.J. and Y. Tor, *Antibiotics and Bacterial Resistance in the 21st Century.* Perspect Medicin Chem, 2014. **6**: p. 25-64.

149. Kopitz, H., et al., *Determinants of the unexpected stability of RNA fluorobenzene self pairs.* ChemBioChem, 2008. **9**: p. 2619-22.
150. Gohlke, H., C. Kiel, and D.A. Case, *Insights into protein-protein binding by binding free energy calculation and free energy decomposition for the Ras-Raf and Ras-RalGDS complexes.* J Mol Biol, 2003. **330**: p. 891-913.
151. Homeyer, N. and H. Gohlke, *Free energy calculations by the Molecular Mechanics Poisson−Boltzmann Surface Area method.* Molecular Informatics, 2012. **31**: p. 114-122.
152. Hou, T.J., et al., *Assessing the Performance of the MM/PBSA and MM/GBSA Methods. 1. The Accuracy of Binding Free Energy Calculations Based on Molecular Dynamics Simulations.* Journal of Chemical Information and Modeling, 2011. **51**(1): p. 69-82.
153. Andrews, J.M., *Determination of minimum inhibitory concentrations.* J Antimicrob Chemother, 2001. **48 Suppl 1**: p. 5-16.
154. Turnidge, J.D., M.J. Ferraro, and J.H. Jorgensen, *Susceptibility Test Methods: General Considerations*, in *Manual of Clinical Microbiology*, P.R. Murray, et al., Editors. 2003, American Society of Clinical Microbiology: Washington.
155. Williamson, R., et al., *Studies on the mechanism of intrinsic resistance to beta-lactam antibiotics in group D streptococci.* J Gen Microbiol, 1983. **129**(3): p. 813-22.
156. Gurel, G., et al., *U2504 Determines the Species Specificity of the A-Site Cleft Antibiotics: The Structures of Tiamulin, Homoharringtonine, and Bruceantin Bound to the Ribosome.* Journal of Molecular Biology, 2009. **389**(1): p. 146-156.
157. Kloss, P., et al., *Resistance mutations in 23 S rRNA identify the site of action of the protein synthesis inhibitor linezolid in the ribosomal peptidyl transferase center.* Journal of Molecular Biology, 1999. **294**(1): p. 93-101.
158. Xiong, L.Q., et al., *Oxazolidinone resistance mutations in 23S rRNA of Escherichia coli reveal the central region of domain V as the primary site of drug action.* Journal of Bacteriology, 2000. **182**(19): p. 5325-5331.
159. Pringle, M., et al., *Mutations in ribosomal protein L3 and 23S ribosomal RNA at the peptidyl transferase centre are associated with reduced susceptibility to tiamulin in Brachyspira spp. isolates.* Molecular Microbiology, 2004. **54**(5): p. 1295-1306.
160. Long, K.S., et al., *Mutations in 23S rRNA at the peptidyl transferase center and their relationship to linezolid binding and cross-resistance.* Antimicrob Agents Chemother, 2010. **54**(11): p. 4705-13.
161. Gregory, S.T., et al., *Mutational analysis of 16S and 23S rRNA Genes of Thermus thermophilus.* Journal of Bacteriology, 2005. **187**(14): p. 4804-4812.
162. Bulkley, D., et al., *Revisiting the structures of several antibiotics bound to the bacterial ribosome.* Proceedings of the National Academy of Sciences of the United States of America, 2010. **107**(40): p. 17158-17163.
163. Schlunzen, F., et al., *Inhibition of peptide bond formation by pleuromutilins: the structure of the 50S ribosomal subunit from Deinococcus radiodurans in complex with tiamulin.* Molecular Microbiology, 2004. **54**(5): p. 1287-1294.
164. Hermann, T., *A-site model RNAs.* Biochimie, 2006. **88**(8): p. 1021-1026.